

Aachener Verfahrenstechnik Series
AVT.CVT – Chemical Process Engineering
Volume 30 (2022)

Arne Can Lüken geb. Cinar

From Soft Matter Filtration Processes to Microfluidic Filter Cake Visualization

DOI: 10.18154/RWTH-2022-07003

From Soft Matter Filtration Processes to Microfluidic Filter Cake Visualization

Von kolloidalen Filtrationsprozessen zu mikrofluidischen
Deckschichtvisualisierungen

Von der Fakultät für Maschinenwesen
der Rheinisch-Westfälischen Technischen Hochschule Aachen
zur Erlangung des akademischen Grades eines Doktors der
Ingenieurwissenschaften genehmigte Dissertation

vorgelegt von

Arne Can Lüken geb. Cinar

Berichter:

Univ.-Prof. Dr.-Ing. Matthias Wessling

Assoc. Prof. Guy Ramon, Ph.D.

Tag der mündlichen Prüfung: 29.06.2022

Diese Dissertation ist auf den Internetseiten der Universitätsbibliothek online
verfügbar.

Parts of this dissertation have been published. Reproduced with permission from:

Arne Lüken, Lucas Stüwe, Johannes Lohaus, John Linkhorst, Matthias Wessling

Particle movements provoke avalanche-like compaction in soft colloid filter cakes

Scientific Reports 11, 2021, DOI: 10.1038/s41598-021-92119-w

©2021 Springer Nature Limited

Arne Lüken, Lucas Stüwe, Sebastian Bernhard Rauer, Jesco Oelker, John Linkhorst, Matthias Wessling

Fabrication, flow assembly, and permeation of microscopic any-shape particles

SMALL 18.15, 2022, 2107508, DOI: 10.1002/smll.202107508

©2022, The Authors. Small published by Wiley-VCH GmbH

Arne Lüken, John Linkhorst, Robin Fröhlingsdorf, Laura Lippert, Dirk Rommel, Laura de Laporte, Matthias Wessling

Unravelling colloid filter cake motions in membrane cleaning procedures

Scientific Reports, 10, 2020, DOI: 10.1038/s41598-020-76970-x

©2020, Springer Nature Limited

Arne Lüken, Maike Bruckhaus, Udo Kosfeld, Meike Emondts, Matthias Wessling

Automated tangential-flow diafiltration device

HardwareX, 2021, 10, e00200, DOI: 10.1016/j.ohx.2021.e00200

©2020, Elsevier

Titel: From Soft Matter Filtration Processes to Microfluidic Filter Cake Visualization

Author: Arne Can Lüken geb. Cinar

Reihe: Aachener Verfahrenstechnik Series
AVT.CVT - Chemical Process Engineering
Volume 30 (2022)

Herausgeber: Aachener Verfahrenstechnik
Forckenbeckstraße 51
52074 Aachen
Tel.: +49 (0)241 8097717
Fax.: +49 (0)241 8092326
E-Mail: secretary.cvt@avt.rwth-aachen.de
<http://www.avt.rwth-aachen.de/AVT>

Volltext verfügbar: 10.18154/RWTH-2022-07003

Nutzungsbedingungen:

Die Universitätsbibliothek der RWTH Aachen University räumt das unentgeltliche, räumlich unbeschränkte und zeitlich auf die Dauer des Schutzrechtes beschränkte einfache Recht ein, das Werk im Rahmen der in der Policy des Dokumentenservers „RWTH Publications“ beschriebenen Nutzungsbedingungen zu vervielfältigen.

Dieses Werk bzw. Inhalt ist lizenziert unter einer Creative Commons Namensnennung 4.0 International Lizenz (Creative Commons Attribution 4.0 International)

Universitätsbibliothek
RWTH Aachen University
Templergraben 61
52062 Aachen
www.ub.rwth-aachen.de



Acknowledgements

This thesis results from a pool of cooperation and contributions from various people working together with me in the last five years. It would have been impossible to obtain all the results, not to mention the early visions motivating the research, without the support of all these people.

Therefore, I want to thank my promoter and supervising professor Matthias Wessling, my second promoter Guy Ramon, my group leader John Linkhorst, and all my colleagues and friends at the chair of chemical process engineering, who advised and supported me on a day's basis. Additionally, I would like to thank all the students that worked on my projects and thereby intensively contributed to my personal development and the results presented here: Daniel Mehlis, Fabian Kools, Laura Lippert, Lucas Stüwe, Robin Fröhlingsdorf, Max Friedl, Johannes Paduch, Maike Bruckhaus, Lukas Griesberg, Jesco Oelker, Arne Pauschinter, Leo Walter, Vera Schostok, Margret Weißbach, Matthias Geiger, Lea Steinbeck, Johann Savinsky, Alexander Schrade, Robin Fröhlingsdorf, Lukas Griesberg, and Salim Benjamaa.

I essentially thank my parents and my brother for supporting me in every imaginable situation. Last but not least, I thank my wife Hannah and my children Malin and Ole for making every day's life joyful and exceptional.

Aachen, July 2022

Arne Lüken

Ole, Malin ve Hannah için.

Contents

Acknowledgements	v
Abstract	xi
Zusammenfassung	xiii
1 Introduction	1
1.1 Membrane processes	1
1.2 Applications in Micro- and Ultrafiltration	2
1.3 Membrane fouling	4
1.3.1 Particle transport properties	4
1.3.2 Concentration polarization	5
1.3.3 Particle deposition at a membrane	8
1.3.4 Filter cake resistance	9
1.4 Visual filter cake analysis	11
1.4.1 Confocal laser scanning microscopy:	12
1.4.2 Microfluidic analysis of filtration physics	13
1.5 Additive manufacturing boosting membrane process analysis	15
1.6 Scope of the thesis	16
2 Permeation induced cake compaction phenomena	21
2.1 Introduction	22
2.2 Experimentals	25
2.3 Results and Discussion	27
2.3.1 Cake mobility during buildup	28
2.3.2 Cake mobility during compression and relaxation	30
2.4 Conclusion and Outlook	35
3 Filter cakes and assemblies made from any-shape micro-particles	39
3.1 Introduction	40
3.2 Experimentals	42

3.3	Results and Discussion	47
3.3.1	Continuous vertical flow any-shape particle fabrication . . .	47
3.3.2	Permeation of any-shape particle tissues	49
3.3.3	Particles as cell tissue	58
3.3.4	Particle agglomeration and self-assembly	58
3.4	Conclusion	60
4	Filter cake motions in membrane cleaning procedures	63
4.1	Introduction	64
4.2	Experimentals	67
4.3	Results and Discussion	70
4.3.1	Cake morphology during filtration	71
4.3.2	Cleaning by backflushing	73
4.3.3	Cleaning by cross-flow flushing	74
4.4	Conclusion and Outlook	80
5	An automated lab scale filtration system for microgel purification	83
5.1	Introduction	84
5.2	Hardware description	87
5.3	Design files summary	90
5.3.1	Mechanical components	90
5.3.2	Electrical components	92
5.3.3	Arduino nano software	94
5.4	Bill of materials	94
5.5	Build instructions	95
5.5.1	Electrical control system	95
5.5.2	Mechanical device fabrication	95
5.6	Operation instructions	99
5.7	Purification of microgels using TFF	102
5.7.1	Experimentals	102
5.7.2	Results and discussion	104
5.8	Summary	107
6	Conclusion and Perspectives	109
	Bibliography	115

Abstract

Membrane ultra- and microfiltration is a chemical unit operation used to purify and concentrate liquid suspensions of colloids and particles. Typical industrial applications are removing or concentrating colloids, proteins, or cells in water treatment, food processing, and bioprocessing. The filtration performance suffers from the agglomeration of the filtrated matter on the membrane surface as a filter cake. This filter cake adds hydrodynamic resistance on top of the membrane's resistance and decreases the process's overall efficiency. Traditional applications measure the resistances for a specific filtrate at the point of operation and adapt the process design and the operating conditions accordingly. This thesis aims to provide mechanistic insights into the filtration process by developing experimental methods for microscopic filter cake visualization and applying these methods to analyze colloid and particle interactions in the filter cake during filtration. Finally, the thesis presents a novel ultrafiltration-based lab-scale microgel purification process and validates the process compared to state-of-the-art technologies.

This thesis developed two devices for visually observing filter cakes: The first is a microfluidic system that withholds the filtrated particles at a membrane-mimicking structure and enables a visual observation of the filter cake's cross-section. Filtering soft spherical polyethyleneglycol particles provoked avalanche-like compaction of the filter cake during cake built up. The filtration of additive manufactured non-isotropic any-shape particles showed the dependency of the hydraulic resistance and the cake morphology from the particle shape and material. These microscopic particle scale results give essential insights into the particle interactions occurring in filter cakes and permeated assemblies. The second observation device developed and applied in this thesis is a flat sheet membrane filtration cell that visually observes the filter cake using Confocal Laser Scanning Microscopy. During cross-flow cleaning procedures, microgel filter cakes unravel instability-driven 3D patterns on the cake surface, accelerating cake removal. Finally, the microscopic filtration results are supplemented with developing a tangential flow microgel lab-scale ultrafiltration device. The thesis validates the applicability of the process for purifying microgels and reports operational procedures, process quantification, and the purification's challenges compared to state-of-the-art technologies.

This thesis's findings provide one step towards bridging the gap between microscopic particle interactions and filtration cake layer properties. The presented results need to be incorporated into filtration models to translate the fundamental phenomena into applicable separation processes in future works. Finally, the findings are not only relevant for filter cakes, but additionally give insights in various applications of permeated micro-particle assemblies. The properties of self-assembling microparticle scaffolds, e.g., as tissue in cell culture, depend strongly on the particle-particle interactions, the assembly's morphology, and its hydraulic resistance. This interdisciplinary perspective will transfer the methods presented here to drive future developments.

Zusammenfassung

Ultra- und Mikrofiltration sind chemische Verfahren, das zur Reinigung und Konzentration von flüssigen Suspensionen von Kolloiden und Partikeln eingesetzt werden. Typische industrielle Anwendungen sind die Aufreinigung oder Konzentration Proteinen oder Zellen in der Wasseraufbereitung, der Lebensmittelverarbeitung und der Bioprozessindustrie. Die Filtrationsleistung leidet unter der Anhäufung der filtrierten Stoffe auf der Membranoberfläche in Form eines Filterkuchens, welcher den hydrodynamischen Membranwiderstand erhöht und damit die Gesamteffizienz des Prozesses vermindert. Herkömmliche Anwendungen messen die Widerstände für ein bestimmtes Filtrat im Betriebspunkt und legen den Prozess entsprechend aus. Ziel dieser Arbeit ist es, experimentelle Methoden zur mikroskopischen Visualisierung des Filterkuchens zu entwickeln und mit diesen Methoden Kolloid- und Partikelinteraktionen im Filterkuchen zu analysieren. Außerdem wird in dieser Arbeit ein Ultrafiltrationsprozess für Mikrogelaufreinigung im Labormaßstab entwickelt und validiert.

Im Rahmen dieser Arbeit wurden zwei neue Methoden zur visuellen Beobachtung von Filterkuchen entwickelt: Die Erste ist ein mikrofluidisches Ersatzsystem, das die filtrierten Partikel an einer membranähnlichen Struktur zurückhält und eine Visualisierung des Filterkuchenquerschnitts bei verschiedenen Verdichtungsmechanismen ermöglicht. Die Filtration von nicht-kugeligen Partikeln zeigt eine starke Abhängigkeit des hydraulischen Widerstandes und der inneren Struktur von der Partikelform und dessen Material. Diese mikroskopischen Ergebnisse geben wesentliche Einblicke in die Partikelinteraktionen, die in Filterkuchen auftreten. Die Zweite Visualisierungsmethode ist eine Flachmembran-Filtrationszelle, die eine Filterkuchenbeobachtungen durch konfokale Laser-Scanning-Mikroskopie ermöglicht. Die Methode erlaubt die Darstellung des Filterkuchens während der Filtration und auch während verschiedener Reinigungsverfahren. Überraschenderweise erzeugt das Tangential-Fluss-Reinigungsverfahren ein topographisches 3D-Muster auf der Kuchenoberfläche, dass den Filterkuchenabtransport beschleunigt. Schließlich werden die mikroskopischen Filtrationsergebnisse durch die Entwicklung einer Mikrogel-Diafiltrationsanlage im Labormaßstab ergänzt, welche zur Aufreinigung von Mikrogelen angewendet wird.

Um die mikroskopischen Ergebnisse dieser Arbeit im Kontext der Filtrationsanwendungen zu interpretieren, müssen in der Zukunft die vorgestellten Phänomene in mathematische Filtrationsmodelle eingearbeitet werden. Neben der Anwendung für Filtrationen, sind die Ergebnisse auch im Kontext permeierter Anordnungen von Mikropartikeln relevant. Beispielsweise hängen die hydrodynamischen Eigenschaften von selbstorganisierenden Mikropartikelanordnungen als 3D-Gerüst für Zellkultur stark von der Struktur der Anordnung und den Interaktionen zwischen den Partikeln ab. Eine solche interdisziplinäre Sichtweise könnte mit den hier vorgestellten Methoden und Ergebnissen weitere Forschungs- und Entwicklungsprojekte definieren und vorantreiben.

1 Introduction

1.1 Membrane processes

The separation of chemicals accounts for 10-15 % of the world's energy consumption [Shol2016]. Most of these separation processes are based on energy-inefficient distillation processes, using different phase change properties of the substances. However, changing phases requires significantly more energy than pressure-based membrane separations, opening enormous energy- and carbon emission savings potential. E.g., the desalination of water using a distillation process requires up to 40 times more energy than a membrane-based reverse osmosis process [Shol2016].

Membrane processes are classified into liquid filtration and gas separations. Even-though membrane-based gas separations gained growing attention in academia and industry in the last decade and show promising applications in the separation of hydrocarbons, the majority (85 % of expenditure 2019) of membrane applications are still in the field of liquid filtration [Belf2019]. A successful design of a membrane process requires the consideration of three main design parameters: First, the **selectivity** of the membrane is essential for reaching the required purity. Second, the **capacity** of the process at the point of operation defines the active membrane area for the necessary throughput. Finally, the **mass transfer** at the point of operation impacts the deposition of filtrated mater at the membrane surface and strongly influences the capacity and the temporal stability. [Belf2019] While the selectivity and the initial capacity primary depend on the membrane selection, the mass transfer depends not only on the filtrated materials but also on the module design and the operating conditions. E.g., a spacer structure combined with high cross-flow velocities

can efficiently remove colloid deposition on the membrane surface and increase the permeation rate [Wies2018]. The three design parameters are intimately dependent on each other, so that each of them needs to be considered equivalently for the successful operation of a membrane process [Belf2019].

This thesis focuses on the mass transfer of soft particles with sizes of 50 nm - 50 μ m in microfiltration (MF) and ultrafiltration (UF) processes. Therefore the following sections will target the phenomena occurring in these processes.

1.2 Applications in Micro- and Ultrafiltration

Today's major applications of MF and UF are in the fields of water treatment, bioprocessing, and food processing. **Water treatment** applications include processes treating surface water, reusing water in chemical processes and drinking water applications, and treating wastewater. Membrane-based water treatment processes are applicable on any scale, ranging from personal carry-on drinking water purification [Life2021] to industrial-scale produced wastewater purification [Belf2019]. The main goal in all processes is the removal of contaminants from water, including dust particles or cells in MF, but also microbes or macromolecules in UF processes (Figure 1.1).

Liquid membrane filtration processes separate particles and molecules gently, based on their molecular size and charge, by flushing them through a porous structure. This delicate processing makes membrane processes advantageous for proteins and living matter in **bioprocessing** compared to thermal separation processes. Virtually every biotechnology process includes several UF processes in upstream processing, in the reaction unit, and downstream processing [Robe2001]. Examples for upstream processing include sterile filtration of buffers and chemicals or virus filtration. In the bio-reactor itself, membranes are integrated for continuous product removal during cultivation and as a scaffold for cell immobilization on the membrane surface, allowing nutrient or oxygen supply through the membrane. Membrane-based downstream processes include cell harvesting, concen-

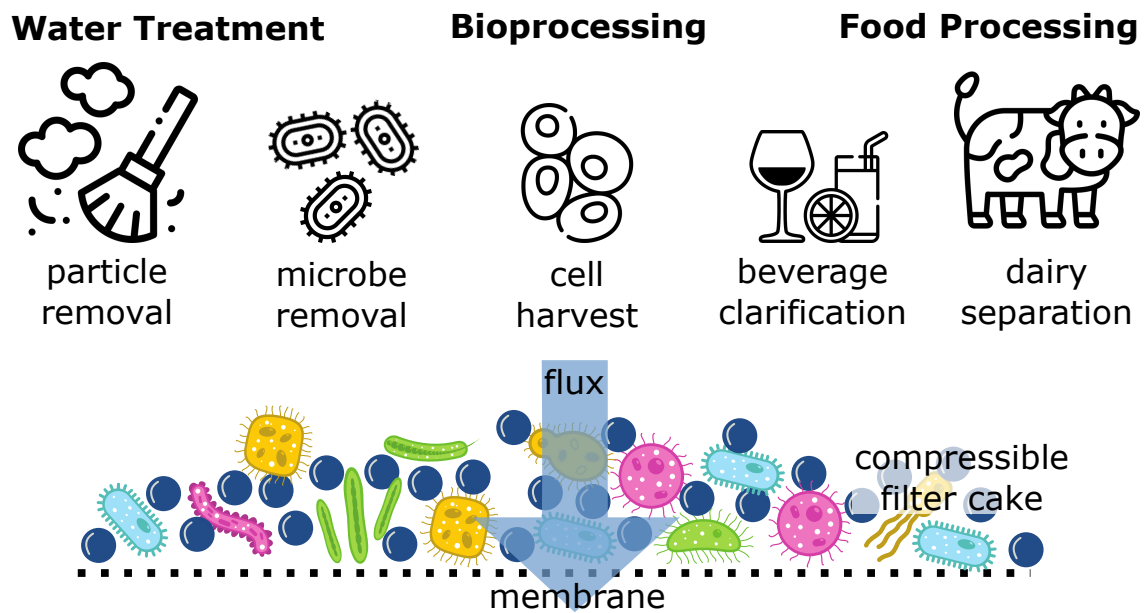


Figure 1.1: Exemplary applications of MF processes in water treatment, bioprocessing and foodprocessing, all forming soft compressible filter cakes on the membrane surface. (Icons are designed by macrovector_official / Freepik.)

tration and separation of cells and proteins [Char2006]. Finally, in downstream bioprocessing, membrane chromatography extends the membrane-based separation possibilities. Molecules are separated based on the material interactions by selective adsorption and desorption on the inner membrane surface [Fröh2012].

Besides water treatment and bioprocessing, MF is widely applied in **food processing** for purifying liquids from microorganisms, proteins (e.g., casein micelles), or fat globules in dairy and beverage processing. In dairy processing, MF is widely used for removing microorganisms extending the shelf life of milk even more than ultra-high-temperature processing (UHT) with a lower cost [Zahe2019]. In cheese making, MF is applied for defatting whey and for enriching casein micelles and removing serum proteins [Kuma2013]; [Nels2005]. Further, smaller-scale on-site applications approach milk concentration for reducing transportation costs [Kuma2013]. Concentration using MF is also carried out in juice processing, containing the taste of freshly squeezed juice, while reducing costs of worldwide shipping [Jiao2004]. Processing of fermented beverages, such as wine and beer, use MF processes for clarification, purification, and reduction of the

total microorganism count. In comparison to traditional mash separation, MF helps to reduce processing times, prolongs shelf life and can achieve higher yields [Geor2001].

Although different applications have significantly different feed concentrations and flow rates, all MF and UF processes include the removal of soft and deformable biological matter, such as proteins, cells, or microbes. The filtered particles accumulate on the surface of the membrane as compressible filter cake, adding a hydraulic resistance to the membrane's own resistance.

1.3 Membrane fouling

Membrane fouling is a general term for describing the reduction of membrane efficiency by the accumulation of particles, molecules or salts on the membrane surface and increasing the process's energy consumption. In MF and UF, filter cake formation predominantly defines the fouling behavior. This cake layer formation depends on the operating conditions and the particle transport properties. A membrane process can either be designed as a dead-end or tangential-flow filtration. In dead-end filtration, the complete feed-stream is flushed through the membrane so that the entire rejected matter accumulates on the membrane surface. In tangential-flow filtration (TFF), also called cross-flow filtration, the fluid flows tangentially along the membrane's high-pressure side. As a result, a share of the feed stream permeates the membrane, and a concentrated retentate stream leaves the membrane on the high-pressure side. In this TFF operation mode, filter cake formation and thickness depend on the particle transport properties and the flow conditions in the module [Bake2004].

1.3.1 Particle transport properties

The particle transport properties during a filtration are characterized using the Peclet number Pe , which is a dimensionless number giving the ratio of

advective to diffusive mass transport defined by:

$$Pe = \frac{\text{advective mass transport}}{\text{diffusive mass transport}} = \frac{L \cdot v}{D} \quad (1.1)$$

where L being a characteristic length, i.e. the membrane boundary layer thickness δ (section 1.3.2), v the flow-velocity, i.e. the permeation flux, and D the diffusion coefficient for particles and colloids. The diffusion coefficient D is given by the Stokes-Einstein-equation [Eins1905]:

$$D = \frac{2 \cdot k_B \cdot T}{6\pi \cdot \eta \cdot d} \quad (1.2)$$

where k_B being the Boltzmann constant, T the absolute Temperature, η the dynamic viscosity and d the particle diameter.

For MF and UF applications, this results in a Peclet number of:

$$Pe = \frac{\delta \cdot 6\pi \cdot \eta \cdot v \cdot d}{2 \cdot k_B \cdot T} \quad (1.3)$$

Accordingly, the Peclet number is lineary dependent on the particle size. As a result, diffusive transport phenomena dominate the filtration of small molecules, such salts in RO (small Peclet). On the other extreme, the particle transport of 5 μm sized cells during an MF process is dominated by advective fluid transport with almost negligible particle diffusion (large Peclet). [Bake2004]

1.3.2 Concentration polarization

Correlating the transport phenomena of molecules and particles (component i) to a cross flow filtration process, results in the model of concentration polarization (CP). The feed sided bulk is flowing tangentially along the membrane and is well mixed. However, close to the membrane, there is a laminar boundary layer with negligible tangential flow velocities, but dominating transport phenomena perpendicular to the membrane. The filtrated component i is **advectively transported** $J_v c_i(x)$ towards the membrane by the permeation flux, but retains at the membrane surface and accumulates

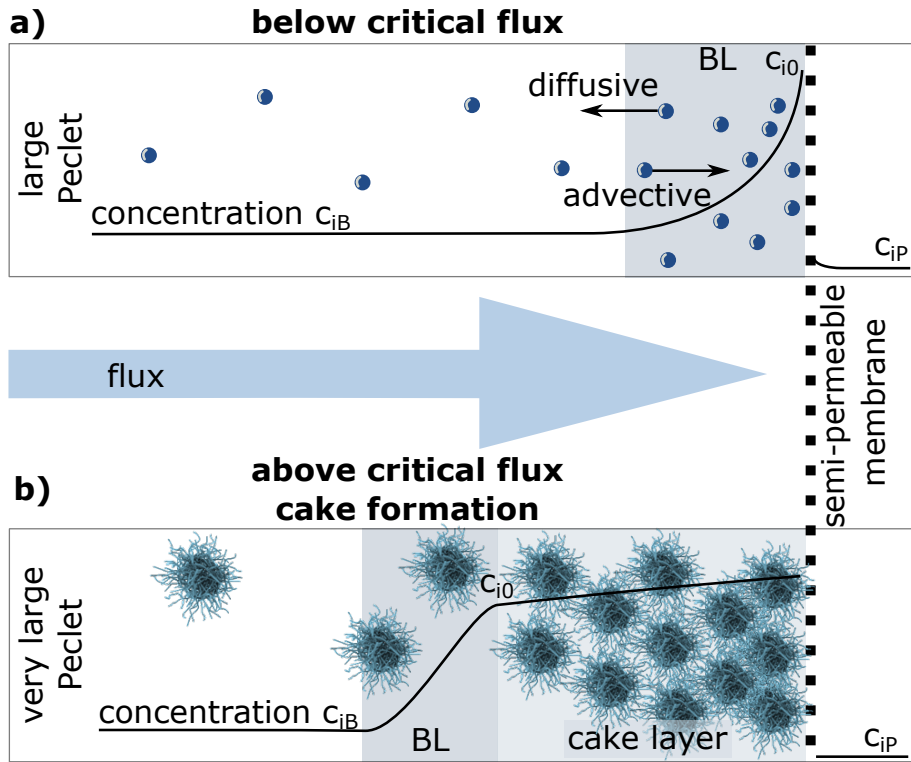


Figure 1.2: Transport phenomena close to the membrane surface depend on diffusive and advective transport mechanism. Operation below the critical flux results in a diffusion-driven concentration polarization *boundary layer* (BL)(a). Operation above critical flux generates particle accumulation on the membrane forming a *cake layer* (b). The particle size predominantly affects the Peclet number and the critical flux by being inverse proportional to the diffusion coefficient D_i .

there. The increased concentration gradient between membrane surface and bulk $c_{i0} - c_{iB}$ induces a **diffusive transport** $D_i \frac{dc_i(x)}{dx}$ towards the bulk. These two transport phenomena result in a steady state increased concentration in the membrane boundary layer (Figure 1.2a). The material quantity balance for the retained component i yields equation 1.4 [Bake2004]

$$J_v c_i(x) - D_i \frac{dc_i(x)}{dx} = J_v c_{i,P} \quad (1.4)$$

with J_v being the volume flux in the boundary layer generated by permeate flow ($m^3/(m^2s)$) and D_i the diffusion coefficient of the component i in the respective solvent. Integration over the thickness of the boundary layer δ with boundaries $c_i(x = 0) = c_{iB}$ and $c_i(x = \delta) = c_{i0}$ yields the polarization

equation [Bake2004]:

$$\frac{c_{i0} - c_{iP}}{c_{iB} - c_{iP}} = \exp\left(\frac{J_v \delta}{D_i}\right) \quad (1.5)$$

The term $(\frac{J_v \delta}{D_i})$ represents the ratio of advective J_v and diffusive D_i/δ fluid transport and corresponds to the above mentioned Peclet number (section 1.3.1).

Going one step further, equation 1.5 can be solved for c_{i0}/c_{iB} , which is named the concentration polarization modulus (CP modulus) [Bake2004]:

$$\frac{c_{i0}}{c_{iB}} = \frac{\exp(J_v \delta / D_i)}{1 + \frac{c_{iP}}{c_{i0}} [\exp(J_v \delta / D_i) - 1]} \quad (1.6)$$

This CP modulus is a dimensionless number for evaluating the CP's affect on the membrane performance. In reverse osmosis, the flux is small and the diffusion coefficients are high, resulting in CP modulus between 1.1 and 1.5, i.e. the osmotic pressure at the membrane is 1.1 to 1.5 times higher than between bulk and permeate [Bake2004]. For ultrafiltration processes with higher fluxes and lower diffusion coefficients, the CP modulus may be significantly larger, up to 5 or 10, seriously affecting the membrane performance, as shown for e.g. ultrafiltration of double-digit nanometer scaled colloids [Roa2015]; [Roa2016].

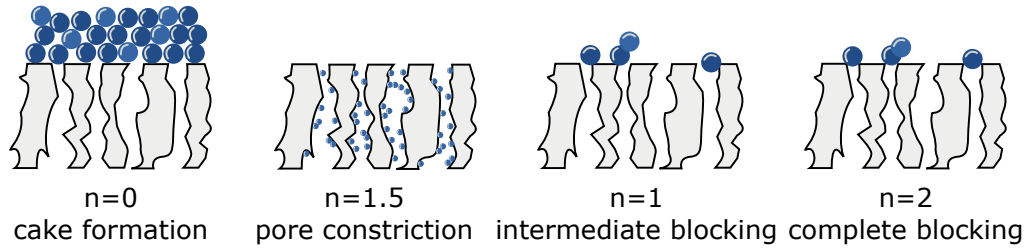
Increasing the colloids size to $d > 100$ nm the diffusion coefficient decreases severely resulting in very high Pe. Depending on the applied flux J_v , the concentration at the membrane c_0 exceeds the theoretical packing density, resulting in a packed arrangement of colloids on the membrane surface as filter cake. Thereby, first, the particles deposit on the membrane surface (1.3.3) and afterwards, if all pores are blocked, colloids accumulate in several layers on the membrane (Figure 1.2b). The minimal flux required to create a filter cake on the membrane surface is called **critical flux**. For operation conditions above the critical flux more and more particles are transported towards the membrane and accumulate on the membrane surface. Accordingly, in constant flux operation mode, the filter cake grows and it's resistance increases continuously without reaching

steady state (see section 1.3.4) [Fiel1995]. For operation at critical flux, quickly occurring in MF, the CP in the boundary layer model does not suffice to describe the filtration performance because the filter cake's hydraulic resistance dominates the process properties.

1.3.3 Particle deposition at a membrane

During filtration below critical flux and during the startup procedure of filtration above critical flux, the filtrated particles deposit on the membrane surface. Based on the classical fouling model from Hermans and Bredée [Herm1936]; [Gons1950], Hermia developed a constant pressure filtration model correlating the temporal development of the filtration flux to particle deposition phenomena at a membrane (Figure 1.3) [Herm1985]. Four fundamentally different phenomena were reported and correlated to the flux: cake formation, intermediate pore blocking, pore constriction (also standard pore blocking), and complete pore blocking (Figure 1.3). The predominant phenomenon depends on the filtrated matter and the membrane, including the particles' sizes, the membrane's pore size, and the particles' interactions with the membrane [Hlav1993]. Since then, the model was adjusted and improved regarding mixed deposition phenomena [Ho2000] and adapted to various specific process applications, including constant flux and cross flow filtration [Hlav1993]; [Fiel1995]; [Kirs2019]. Hermia's filtration model explains macroscopic filtration data with microscopic particle interactions and, therefore, presents a strong basis for interpreting microscopic filtration phenomena in the context of filtration data [Ngen2010b].

This thesis's topic focuses on the phenomena occurring in a filter cake, i.e. during filtration processes with $n=0$, not regarding the particle membrane interactions and the deposition phenomena of particles on the membrane surface and inside membrane pores. Therefore, at this point this thesis focuses on filter cake's resistances.



$$\frac{d^2t}{dV^2} = k \left(\frac{dt}{dV} \right)^n$$

t = filtration time
 V = permeated volume
 n = fouling type index
 k = deposit specific resistance coefficient

Figure 1.3: Illustration of different particle deposition and pore blocking phenomena based on Hermia [Herm1985] with the respective equation correlating these particle scale phenomena to a measurable filtrate flux correlation

1.3.4 Filter cake resistance

In membrane processes filter cakes emerge when retained particles accumulate on the membrane surface. This occurs in dead-end processes, when the particle's sizes exceed the membrane's pore size and the amount of retained particles exceeds the formation of a monolayer on the membrane. In cross-flow processes, depending on the particle's transport properties, filter cakes emerge, when the filtrated particles have a slower back-diffusion to the bulk than the advective, flux-driven transport towards the membrane (section 1.3.2). In both configurations, during filter cake formation, the permeating flux needs to permeate the filter cake additionally to the membrane, increasing the overall hydraulic resistance. The permeation through the filter cake J can be described by the filtrate flux equation [Bake2004], which is derived from Hermia's filtration correlation for $n=0$:

$$J = \frac{\Delta p}{\eta(R_m + \alpha \cdot m)} \quad (1.7)$$

where Δp is the applied transmembrane pressure, η the fluid viscosity, R_m the membrane resistance, α the specific cake resistance, and m the mass of cake per unit membrane area. In membrane processes, the cake resistance is often evaluated indirectly. The flux and pressure drop are mea-

sured at a specific operation point, and the cake resistance is calculated from the data. Similar methods are also applied for correlating empirical measurements at different fluxes to the specific cake resistance [Fole2006]. This procedure delivers important process information for designing and operating industrial filtration processes; however, it does not describe the cake resistance mechanistically with discrete events [Bouh2019a]; [Grif2022].

A rather mechanistic analysis model for rigid particles is given by a modified Carman-Kozeny equation. It estimates the cake resistance by correlating the permeation velocity u of the fluid in a packed bed with the porosity ε [Rich2002]:

$$u = \frac{\varepsilon^3}{K \cdot S_v^2 (1 - \varepsilon)^2} \frac{\Delta p}{\mu \cdot h} \quad (1.8)$$

where K is the Kozeny constant, S_v the particle surface area per unit volume, and h the bed depth, i.e. the height of the cake in front of the membrane. This equation can then be adapted to filtration processes to yield the specific cake resistance α from equation 1.7 [Fole2006]

$$\alpha = \frac{K \cdot S_v^2 (1 - \varepsilon)}{\varepsilon^3 \cdot \rho_p} \quad (1.9)$$

with ρ_p being the density of the particles. This approach is valid for non-compressible filter cakes, however, most applications of MF and UF result in soft compressible filter cakes, making empirical correction factors for the Kozeny constant K necessary for a reasonable fitting [Fole2006]. For soft filtration systems, the packing density increases towards the membrane which leads to a higher porosity at the bulk side compared to the membrane-boundary [Fole2006].

The Hagen-Poiseuille equation, which is also considered in the Carman-Kozeny equation, gives demonstrative assistance for understanding the importance of compressibility in a filter cake. It correlates the pressure loss Δp at a specific flowrate J in a capillary to its radius r and length L

through [Oert2015]:

$$J = -\frac{\pi}{8\eta} \frac{\Delta p}{L} \cdot r^4 \quad (1.10)$$

with η being the viscosity. The capillary radius r impacts the hydraulic resistance to the power of four, being the crucial parameter for the hydraulic resistance's order of magnitude. The change of the effective capillary-radius in a compressed filter cake was estimated in a geometrical model by Linkhorst et al. He calculated the diameter of a pore in the void space between 4 deformed, spherical colloids at constant colloid volume (isochoirity) in a crystal arrangement during compression by [Link2019]:

$$r_{pore} = \left(\frac{\sqrt{3}}{3} - 0.5 \right) \cdot \frac{\frac{\pi}{6} \cdot a - \frac{\sqrt{3}}{3} \cdot a_{def}}{\frac{\pi}{6} - \frac{\sqrt{3}}{3}} \quad (1.11)$$

while a is center colloid distance without deformation and a_{def} the distance during the deformation. Assuming a compression $(a - a_{def})/a$ of 5% results in a void pore size reduction of 54%, leading to a 20 fold hydraulic resistance based on the Karman-Cozeny equation. Even though this estimation is very error-prone based on the geometrical isochoric deformation model, it highlights the importance to account for particle deformation and particle density gradients in a filter cake.

1.4 Visual filter cake analysis

Correlating the filter cake morphology to the permeation properties helps validate and develop filtration models that transfer single-particle properties to the hydraulic resistances of a filter cake. However, the direct correlation of the morphology to permeation properties is only reasonable using in-situ real-time monitoring. There are a variety of in-situ methods including visual microscopic observation, light-based spectroscopy, acoustic techniques, interferometry, magnetic resonance imaging, X-ray and neutron imaging, vibrational spectroscopy, controlled current, and controlled stress techniques, which are precisely summarized in a recent review arti-

cle [Rudo2019]. However, either the gained information or the lowest resolution of existing techniques does not allow precise statements about single colloid behavior in filter cakes.

1.4.1 Confocal laser scanning microscopy:

Confocal laser scanning microscopy (CLSM) is a visual microscopic observation method capable of providing 3D microscopy data with sub-micron resolution. The technology allows the individual detection of various fluorescently labeled species in a multi-component sample by exciting the sample with different wavelength lasers and separately detecting the emissions from several fluorescent dyes. A scanning laser provides high sub-micron resolution in the field of view, and confocal optics make it possible to decrease the z-resolution down to 1 μm . Moving the sample through the focal plane enables the generation of 3D visualizations.

Applying CLSM for filtration monitoring enables the detection of particles on the membrane surface during a filtration process (Figure 1.4a). Several studies performed similar in-situ monitoring of particle deposition, including the visualization of mono-disperse and bi-disperse particle accumulations on different membrane surfaces [Ben 2014a]; [Ben 2014b]. Furthermore, it is possible to distinguish surface fouling and in-pore fouling [Krom2006]; [Bran2007], and study particle deposition at varying salt concentrations and pH in correlation to filtration resistances [Di2017]; [Di2018]. However, the in-transparency of the accumulated particles limits the ability to in-depth study real filter cakes.

Nevertheless, biological matter and hydrogels partially transmit light, making an in-depth visualization of the deposited matter possible. Therefore, such samples allow phenomenological statements of the filter cake composition at different depths [Beau2011]; [Bere2010] and make greater use of the CLSM abilities. Incorporating fluorescent nano-particles in transparent and soft alginate layers enables a micro-rheological analysis of the cake at different depths. The rheological properties of the gel-layer are distinguished by measuring the diffusive movements of the nano-particles in the alginate

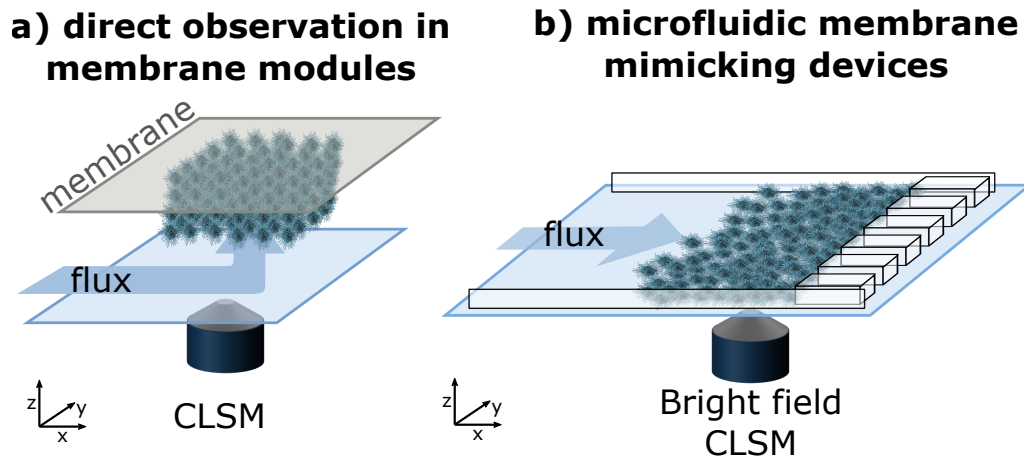


Figure 1.4: Schematic field of view for the direct observation of flat sheet membranes (a) and microfluidic membrane mimicking devices (b). Visual observation of the membrane surface results in a top view, requiring 3D-CLSM to get depth information of the filter cake (a). Microfluidic membrane mimicking devices provide a cross-sectional view of the filter cake and the pores allowing analysis of the filter cake depth using bright field microscopy (b).

filter cake [Epst2021]. However, a detailed analysis of particle density gradients and particle arrangements in a filter cake, which would be desired to generate a particle-scale filter cake model, has not been demonstrated in a filtration process yet. In addition, the non-transparency of the sample and the limited focal distance affect the module design and hinder high-resolution in-situ analysis.

1.4.2 Microfluidic analysis of filtration physics

Various methods for membrane integration in microfluidic channels allow the integration of commercial membranes, the in-situ synthesis of membranes in phase boundaries in microfluidic channels, and the creation of porous structures retaining particles [Jong2006]. These membrane mimicking structures allow the in-chip filtration of soft particles and colloids, creating densely packed assemblies, similar to filter cakes in membrane processes. Thereby, a transparent glass slide represents one of the channel walls and allows a direct cross-sectional view of the filter cake (Figure 1.4b).

The main focus of microfluidic membrane mimicking studies is to observe particle-particle and particle-surface interactions visually, transfer these phe-

nomena to mathematical equations, and bridge the gap towards discrete filtration processes [Bouh2020]. The clogging of single micro-pores for different particle and pore sizes was studied and resulted in diverse pore-clogging phenomena, named sieving, bridging, and aggregation [Dres2016]; [Saur2014]: If the cross-section of the particle is larger than the pore, the particle will get stuck in the pore entrance and block this pore for the following particles similar to a **sieving** effect. **Bridging** happens at higher colloid concentrations, when several particles, which are significantly smaller than the pore, bridge the pore by agglomerating and covering the pore in a bridge-like structure. In **aggregation**, colloids aggregate at the inner surface of a pore by surface interactions and potentially block a pore by decreasing the diameter subsequently.

Particle-particle interactions were additionally modeled applying the DLVO-theory [Peto2010], showing that the repulsive and attractive forces between particles and walls have a significant influence on the aggregation and clogging phenomena [Bacc2011]; [Send2016]. Additionally, the overall clogging process depends on the pore geometry, and the particle compressibility [Bouh2019a]. CFD-DEM models allow the incorporation of the fluid dynamics into the clogging procedures of single pores [Loha2018] and cleaning by backflushing [Loha2020], however, are limited to short modeling times by the computational effort. Models coupling discrete and continuum models allow a discrete description of pore blocking events while reducing computational cost and making such models a promising alternative for realistic time scales [Grif2022]. These varieties of studies offer first approaches to describe and predict discrete particle behavior at an MF pore.

Another critical aspect of MF and UF processes is gel and cake layer formation. Microfluidic model systems with membrane mimicking structures can visualize the cake layer's cross-section. For example, Linkhorst et al. applied CLSM to visualize single particles in a filter cake during the cake's permeation and showed the formation of highly ordered crystalline regions occurring within permeation procedures for soft microgels [Link2016]. Additionally, the deformation of single microgels and the overall bulk have a strong influence on the assembly's overall pressure drop

[Link2019]; [John2021]. This soft-matter cake layer analysis adds another missing piece to the complex filtration process puzzle. The transformation of the microfluidic observations towards filtration processes is still hindered by the variety of phenomena occurring during filtration. These phenomena include the complex morphology of real membranes, the particle transport in bulk and at the boundary layer, and the mixture of real filtration solutions. Accordingly, model systems are promising for studying defined parameters at high resolution, however, bridging this gap between microscopic observations and filtration processes will only be possible in combination with analysis methods being capable of studying real filtration systems [Kerd2019]; [Desm2018]; [Jafa2019] and will continue pushing the microscopic membrane community in the future years [Bouh2020].

1.5 Additive manufacturing boosting membrane process analysis

Additive manufacturing - commonly known as 3D printing - is the fabrication process of three-dimensional (3D) objects from computer-aided design (CAD) models. The object is typically formed by joining materials together in a layer-by-layer fabrication process. On the one hand, additive manufacturing offers fabrication of customized structures of complex geometries that are hardly producible by traditional manufacturing and, on the other hand, allows a reduction of the fabrication time and costs in prototyping applications [Lee2016]. In membrane research, various additive manufacturing technologies are applied for unraveling novel analysis methods driven by the production of complex geometries and taking advantage of fast and cheap prototyping.

Lab-scale filtration systems can be easily fabricated by 3D-printing custom holders, connections, and housings for the components using fused filament fabrication (FFF). Additive manufactured membrane modules with optimized geometries advance flow conditions and allow rapid analysis and adaption of the module design [Ande2013]; [Bait2021]. Furthermore, 3D

printed spacer geometries can serve as secondary flow promoting structures for various membrane configurations [Shri2008]; [Armb2018] and can also be printed in metal, serving as an electrode in electrochemical reactors [Löls2017]. Structuring the membrane surface topology can also improve the mass transfer in the membrane boundary layer. A polyjet and stereolithography (SLA) printed spinneret allows the fabrication of such helical ridge on the membranes improving the mass transfer during UF applications [Tepp2022]. Printing membranes with single pores is hindered by the resolution and the final sample size of existing 3D printers. However, high-resolution direct laser writing allows the introduction of porous membrane-like structures into microfluidic channels [John2021]. This technique can also be applied to fabricate free-form molds for microfluidic chip fabrication via soft lithography [Löls2018] or creating microfluidic channels for filtration analysis.

This thesis applies various additive manufacturing methods to create the experimental environment for analyzing soft matter filter cakes. The experimental environment includes fabricating device components using FFF, membrane modules using polyjet printing, microfluidic channels and any-shape particles as filter particles using direct laser writing.

1.6 Scope of the thesis

The present thesis analyzes the process of filtering colloids and soft micro-particles, focusing on the fundamental phenomenon occurring in the filter cake. It bridges the gap between microfluidic soft colloid assemblies, filter cake physics, and lab-scale filtration processes by transferring micro-scale particle interactions during cake compaction to dynamic cake-scale movements and lab-scale filtration processes. Thereby, the chapters in this thesis address the following research questions:

- Chapter 2: How does filter cake permeation affect the mobility of the single particles in the assembly?
- Chapter 3: How does the shape and softness of particles influence

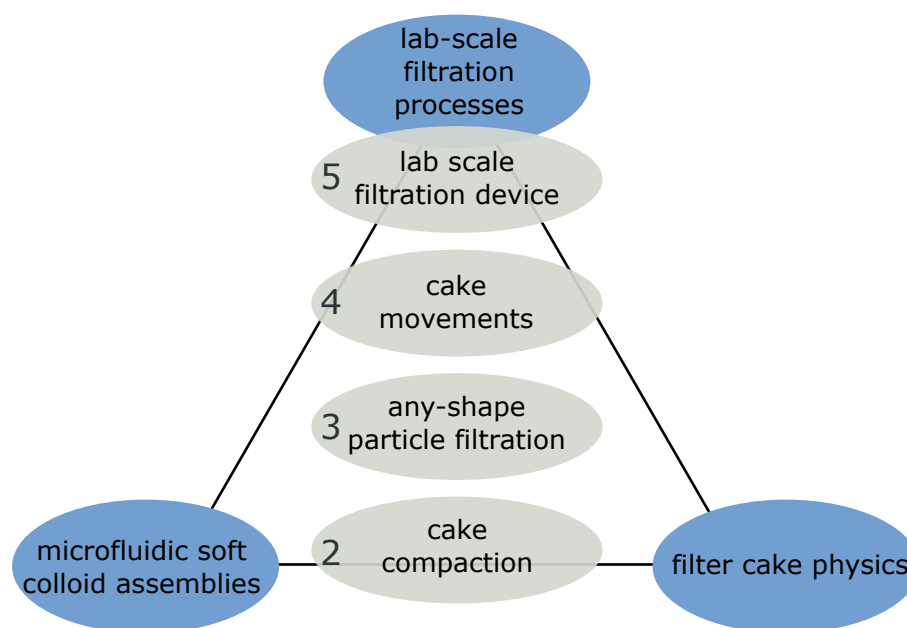


Figure 1.5: Outline of the thesis

the filter cake morphology and its hydraulic resistance?

- Chapter 4: How do colloidal filter cakes behave during membrane cleaning procedures including backflushing and cross-flow flushing?
- Chapter 5: Can soft colloids be purified by tangential flow filtration and how could an automated lab scale device look like?

Chapter 2 presents a fundamental microfluidic experimental study analyzing *filter cake compaction* by visualizing single-particle movements occurring in permeated filter cakes. The soft particles are fabricated by microfluidic emulsion polymerization, and their softness provokes rearrangements of the filter cake during permeation. The experimental study is additionally accompanied by CFD-DEM modeling approving the results on a phenomenological level.

Chapter 3 tackles the question of how the particle shape influences the cake morphology as well as the hydraulic resistance. The chapter presents a continuous two-photon lithography fabrication method for microscopic any-shape particles and studies the particles assemblies in a microfluidic filtration device during permeation. The particle's shape, size, and softness correlate to the packing density and the hydraulic resistance.

In **chapter 4**, colloidal fluorescent microgels are filtered in a flat sheet membrane module, and their filter cake is visualized during filtration and cleaning procedures. This study links microscopic cake morphology to filtration process conditions. During cake removal by cross-flow flushing, a longitudinal stripe pattern occurs on the filter cake boundary layer. This instability is analyzed according to the flow conditions, and its accelerated cake removal properties are investigated.

Chapter 5 presents a novel method for purifying precipitation polymerized microgels by tangential-flow filtration. The proof of principle for the purification task is given, and a detailed hardware description of an automated lab-scale filtration device for microgel purification applying low-cost hemodialysis membrane modules is presented.

Chapter 6 summarizes the thesis and stimulates to interpret filter cakes in a different context as porous and permeable soft scaffolds, e.g., in the field of tissue engineering.

This thesis includes the results of the following **student theses** written under the supervision of Arne Lüken:

- Fabian Kools, 2018, Master thesis, *Design of a versatile microfluidic impedance device for organ-on-a-chip and filtration applications*
- Laura Lippert, 2019, Bachelor thesis, *Microgel filtration - Filtration analysis and in situ visualization using microscopy*
- Lucas Stüwe, 2019, Master thesis, *Visualization of Microgel Filtration using Particle Image Velocimetry (PIV)*
- Robin Fröhlingsdorf, 2019, Bachelor thesis, *Investigation and visualisation of filter cake formation and removal in microgel filtration*
- Max Friedl, Johannes Paduch, Project thesis, 2019, *Purification of microgel solutions via ultrafiltration*
- Maïke Bruckhaus, 2019, Master thesis, *Development of an ultrafiltration device for microgel purification*

- Lukas Griesberg, 2021, Seminar Paper, *Investigating soft matter fouling effects using constant flux measurements and hydraulic impedance spectroscopy*
- Jesco Oelker, 2021, Master thesis, *Continuous 2-photon production and filtration of anisotropic particles*

2 Permeation induced cake compaction phenomena

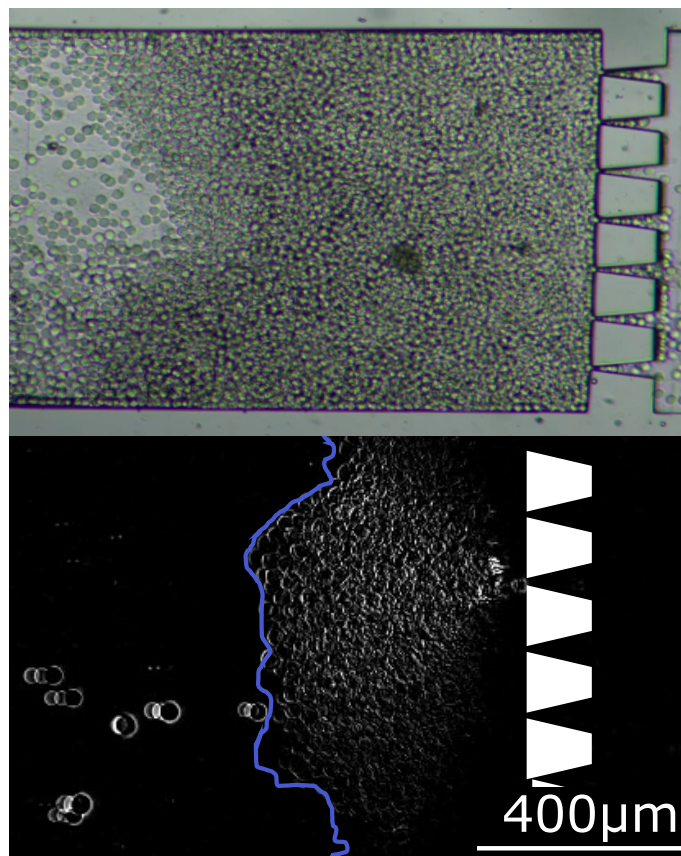
2

Parts of this chapter have been published as:

Arne Lüken, Lucas Stüwe, Johannes Lohaus, John Linkhorst, Matthias Wessling

Particle movements provoke avalanche-like compaction in soft colloid filter cakes, Scientific Reports 11, 2021

DOI: 10.1038/s41598-021-92119-w



2.1 Introduction

Membrane filtration is a unit operation in chemical processes to efficiently separate colloids from aqueous suspensions applied in, e.g., water treatment, food processing, or bioprocessing. During filtration, the colloids accumulate on the feed side surface of the membrane in a cake layer. This cake layer generates an additional resistance on top of the membrane's resistance and reduces the performance of the overall filtration process [Raut2004]. To optimize filtration performance and predict cake properties, intrinsic knowledge of the phenomena occurring inside the cake on a colloid-scale is essential.

During the filtration of biological suspensions, such as applied in food processing [Moha2012] or membrane bioreactors [Jørg2014], the filtered matter is soft and deformable. In contrast to hard particle filtration, the soft particle cake layer is compressible, such that the specific cake resistance depends on the filtration time and the applied flux [Bell2020]. Additionally, the soft cake layer is not packed uniformly but shows an increasing packing density towards the membrane [Fole2006]. Accordingly, the specific cake resistance increases over the filter cake thickness and reaches its maximum at the most compressed gel layer next to the membrane [Bake2004]. In soft matter microfiltration applications, this gel layer often dominates the pressure loss of the overall process [Hwan2003]; [Hwan2009]; [Bouh2018].

For explaining gel layer formation, the general phenomena during compression of a collection of soft colloids need to be considered. This compression strongly depends on the local colloid concentration and can be described in three stages. In the first stage, concentration is low, and single colloids are separated from each other. The colloids behave like hard spheres rearranging their position and filling up large voids in the cake [Moha2014]. In the second stage, the concentration is higher. The colloids are in a fixed position inside the collection and start deforming and narrowing the neighboring colloids' voids. Many different physical phenomena ranging from thermal agitation to compression and deformation [Bouh2018]; [Link2019], as well as interpenetration and crystallization [Moha2017];

[Bouh2017] depend on the particle's softness and charge and influence the cake's morphology and the corresponding cake resistance [Lu2001b]; [Lu2001a]. One phenomenon of this stage is that the packing's morphology and coordination depend on the previous filtration time and applied force [Li2014]; [Oğuz2012]. The particles stick in an amorphous geometrical frustration, which can reach a higher packing density by mechanical agitation induced rearrangement [Léva2018]. The particle interactions, as well as their shape and size, significantly affect the rearrangement kinetics and the resulting packing [Dull2006]. In the last stage, at very high compression, the colloids form a homogeneous material without voids. The packing still behaves compressible by water expulsion like a polymer gel [Menu2012].

Stage one and stage two networks occur in a filtration process during cake formation, where fluid permeates the compressed filter cake and the voids between the colloids. The void size mainly influences the cake-specific fluid resistance, and the pressure loss correlates to the inverse void-radius to the power of four (Hagen–Poiseuille). Subsequently, minor void size changes induced by particle deformation and cake compression affect the permeation characteristic tremendously [Hwan2010]; [Link2019]; [Di L2013]. The most compressed gel layer with the smallest voids next to the membrane dominates the overall pressure loss [Fole2006]. This dense gel layer might become a stage three network without voids when filtering tiny and soft colloids at high compression or when particles break by compression. In this case, the fluid needs to permeate through the compressed colloid material, which has higher fluid resistances than the filter cake's porous structure. Thus, the gel layer permeation properties dominate the overall cake resistance [Bacc2002].

The soft matter multi-stage cake behavior and the subsequent filtration process is often inaccurately described by models, such as the conventional cake filtration theory [Lu2001b]; [Hwan2003]. There exist a variety of empirical and semi-empirical models, which macroscopically describe softness and compression effects of the filter cake on the permeation [Hwan2003]; [Meir2004]; [Bugg2012]; [Bouc2014]. These models are very

valuable to describe and to design filtration processes. The interplay between the reversible / irreversible compression and hydrodynamic permeation is determined by the micromechanics of the individual soft particles, which is difficult to analyze with these macroscopic models. Therefore, the evaluation of the micro-mechanics of the particles inside the filter cake is of great interest. Simulation tools combining particle mechanics coupled with fluid dynamics help to decode the complex reversible and irreversible compression phenomena inside the filter cake of soft particles. These methods potentially enable to connect the individual soft particles' properties and the empirical parameters which still remains unsolved.

Microfluidic filtration of colloids at porous structures have proven to be a powerful tool for mimicking real filtration processes and visualizing cake morphology on particle scale [Bouh2020]. Hard spherical colloids were flushed through tight microfluidic pore-mimicking constrictions inside poly-(dimethylsiloxane) (PDMS) channels, and the phenomena of particle adhesion on the pore surface and the consequent pore-blocking were studied using visual methods [Bacc2011]. The pore geometry, as well as the foulant and the fluid-properties, were studied. The studies reveal the importance and the influence of particle-particle and particle-wall interactions on particle adsorption and pore-blocking [Send2016]; [van 2016]; [Loha2018]. In contrast to hard particles, soft particles can adapt to the pore geometries by deformation and, therefore, show a smaller pore-blocking tendency [Bouh2019a]; [Bouh2019b]. The microfluidic observation method was applied for pore phenomena and for studying the filter cake in a fouling layer. Different studies investigate the influence of the cake morphology on permeation [Link2016]; [John2021], the deformation of single microgels during cake compression [Link2019], and the relaxation and removal of filter cakes by backflushing [Send2016]; [Loha2020]; [Lüke2020]. These microfluidic studies display the complexity of the phenomena influencing single particles' behavior during micro-and ultrafiltration by studying single events during pore blocking, cake formation, or cake compression. However, transferring single colloid phenomena to real membrane processes lacks the description of how single colloid events, such as colloid deformation, affect

the overall cake morphology and its properties.

This work studies the influence of single-particle movements on the cake properties in microfluidic soft filter cakes. Hence, 27 μm sized soft polyethylene-glycol (PEG) microgels are filtered in front of porous microfluidic structures. The impact of single-particle movements inside the filter cake during filtration is analyzed by image analysis. Thus, this study differentiates particle movements that induce avalanche-like v-shaped displacement of a particle network inside the cake and minor movements of single particles not affecting the cake morphology. After cake buildup, the cake is compressed by applying pressure stepping experiments, allowing the differentiation of reversible and irreversible cake compression and the localization of the spatial position of the two effects. Finally, the experimental findings of irreversible compression are explained and confirmed using CFD-DEM simulations.

2.2 Experimentals

Fabrication of the microfluidic chip Two different microfluidic chips were fabricated using soft lithography replica molding. One chip was used for microgel synthesis using emulsion polymerization and one for the filtration experiments. The positive master mold was 3D-constructed using Autodesk Inventor and fabricated by two-photon dip-in direct laser writing following the procedure described by Loelsberg et al. [Löls2018]; [Blei2018]. Afterward, PDMS (Sylgard 184, Farnell) was used to replicate the molds, holes for tube connection were punched, and the chip was bonded to a microscope slide with a thickness of 1 mm using oxygen plasma.

Microgel synthesis For the microfluidic filtration experiments, PEG microgels are produced inside a microfluidic chip via emulsion polymerization following the procedure as described elsewhere [Jans2017]. In short, the microfluidic cross-junction chip has a height of 50 μm and a nozzle width of 20 μm , such that droplets are formed one-by-one at the intersection of two organic and one aqueous phase flow. Due to different manufacturing

conditions, the droplet size varies slightly from batch to batch. The aqueous phase contains 10 wt% poly(ethylene glycol) diacrylate (MW 575 g/mol) and 0.5 wt% 2-Hydroxy-4-(2-hydroxyethoxy)-2-methylpropiophenone (Ircagure) as radical photo-initiator. A 50:50 wt mixture of cyclohexane and paraffin oil with 8 wt% SPAN80 is chosen as a continuous organic phase. SPAN80 serves as surfactant and prevents agglomeration of formed droplets. Before synthesis, both solutions are mixed separately for at least 10 min. Polymerization of the emulsion takes place in the outlet tube by exposing the droplet-filled tube to UV-light for at least three minutes. The droplet production rate is adjusted by using a constant pressure microfluidic pump system (Elveflow OB1 MK3). The microgel solution is purified by centrifugation based solvent exchange from cyclohexane to isopropanol and finally to distilled water. The microgels show an average diameter of approx. 27 μm with a standard deviation of 2.55 μm and a zeta potential of $-12.7 \text{ mV} \pm 2.95 \text{ mV}$, measured with Zetasizer Ultra (Malvern Panalytical) with a DTS1070 cuvette (Malvern). The slightly negative charge is caused by the remaining acrylate groups in the polymeric network.

Filtration experiments The filtration channel is 800 μm wide and has a height of 150 μm . 8 filtration blocks with a distance of 3 μm in between are placed inside the channel to withhold the microgels. Filtration experiments are executed in dead-end mode using a microfluidic constant pressure pump (Elveflow OB1 MK3) and an additional microfluidic pressure sensor Elveflow MPS1 at the chip inlet. The experiments were executed on a light microscope, and the images were analyzed using the imaging software DaVis10 (LaVision GmbH). The channel is at first contacted with water to ensure complete wetting. In a second step, microgels dispersed in distilled water are added to the fluid flow to build a filter cake. The cake buildup experiment (Fig. 2.1) is conducted by applying constant pressure of 50 mbar to the feed solution. For image analysis a time filter is used to subtract from every image the average of the recent 3 frames for every pixel. This results in highlighted areas illustrating movements in the filter cake. These areas are manually identified and transferred to the graph in

Fig. 2.1c.

The two compression experiments (Fig. 2.2c) are conducted by first building up a filter cake using 17 mbar feed pressure for 13 minutes until no flux is visible and no further incoming microgels build up the cake. In this uncompressed state, pressure stepping is performed by increasing and decreasing the pressure in 50 mbar steps. Subsequently, the previously compressed cake undergoes another compression by repeating the compression cycle, which resulted in the "compressed" curve in Fig. 2.2c. The cake thickness is measured at a specific point in the middle of the channel for every pressure state. Inflowing microgels by increased transmembrane pressure and increasing cake thickness are neglected, as each pressure step is executed in a short period of about 5 seconds. Image analysis for generating the heat-maps (Fig. 2.3) is conducted by using a time filter and subtracting the intensity of each pixel from the state before and after compression using the "Davis 10" software from LaVision GmbH.

CFD-DEM simulations The simulation framework CFDEM © is applied in this study. CFDEM © combines computational fluid dynamics (Open-FOAM ©) with discrete element method (LIGGGHTS ©) to describe particle movement inside a fluid flow field [Goni2010]; [Klos2012]. In the CFD-DEM approach, individual particle trajectories are determined by a force and momentum balance. The particle motion is coupled with the fluid profile by a momentum exchange enabling two-way coupling between fluid and particle [Zhu2007]; [Noro2016]. The continuity equation and the volume-averaged Navier-Stokes equation is used to calculate the fluid flow field in the CFD-part. Detailed information about the CFD-DEM coupling algorithm is provided in the supplementary part.

2.3 Results and Discussion

Soft PEG microgels with a diameter of approx. 27 μm are fabricated by microfluidic emulsion polymerization and are filtrated inside a microfluidic PDMS filtration channel using a porous filter structure. The filter structure

in the channel consists of several filtration blocks with a trapezoidal cross-section as indicated in Fig. 2.1b, c, and d. The 3 μm gaps between the filtration blocks allow an entire rejection of the microgels. The channel's height of 150 μm permit more than eight microgel layers to fit in the filter cake on top of each other.

2

2.3.1 Cake mobility during buildup

This study investigates the mobility of microgels in a filter cake during filter cake formation at constant pressure. Therefore, microgels are filtrated for about 23 min and the cake growth is visualized (Fig. 2.1a). Inside the cake, the microgels change their initial position to fill the voids in the arrangement. The cake formation video is evaluated applying a time filter to improve the visualization of particle movement in the filter cake. The time filter subtracts the average of the previous three frames from each frame. The results is a mostly dark video. Areas without brightness change over the previous three images remain dark, whereas areas in which the pixel information change over the previous three images appear bright. Hence, bright areas highlight particle movements in the bulk and in the filter cake. Moving particles in the bulk change their position over the previous frames and appear as trajectories. One-time movements in the filter cake appear as bright spots. Fig. 2.1b and c showcase two selected frames of the edited video revealing two different phenomenological types of morphology change.

The first type of change describes an avalanche-like displacement of particle networks over the whole filter cake. This type is characterized by a v-shaped geometry ranging from a single microgel on the right side to the cake surface on the left side of the image. These network movements are induced by a single microgel movement on the right side in the filter cake, which causes the following layers to rearrange (see Fig. 2.1b). The second type of morphology change is the single-particle movement, where only one microgel modifies its position in the particle arrangement. In contrast to the first type, no avalanche-like rearrangement follows, and neighbor-

ing microgels remain at their initial position (see Fig. 2.1c). Both types of morphology change are illustrated in Fig. 2.1d.

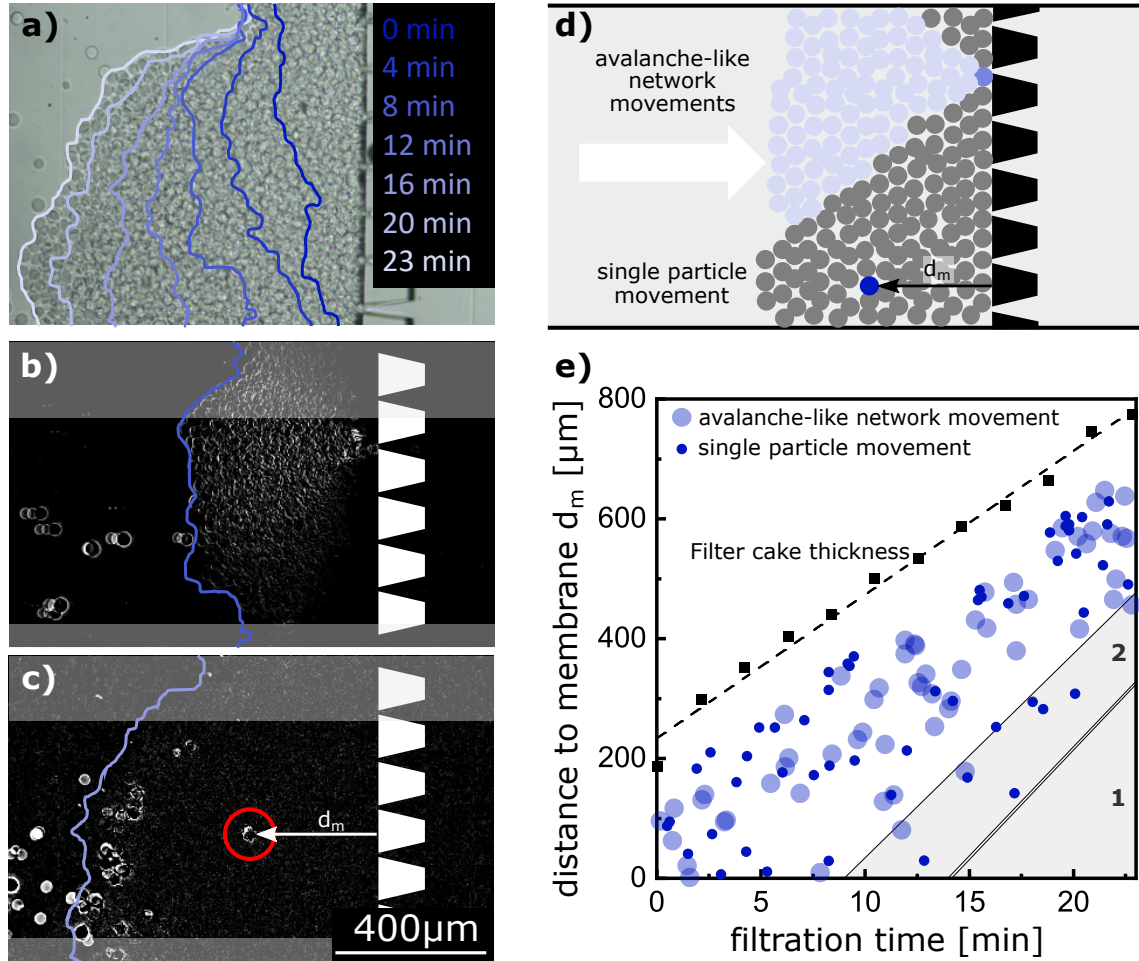


Figure 2.1: Evolution of a filter cake of 27 μm sized PEG microgels inside a microfluidic PDMS channel during constant pressure filtration. The lines in (a) indicate the cake surface at the respective time. Visualization of the local cake movements by microgel rearrangement with avalanche-like network movements (b), and single-particle movements (c). The filter cake surface at that respective time is overlaid as a blue line and the porous filtration structure is overlaid in white for better orientation. Illustration of the two types of rearrangement occurring in the filter cake (d). Position of the rearrangements (blue dots) in the filter cake at the respective filtration time and the filter cake thickness (black squares) (e).

In Fig. 2.1e the particle movements are extracted of the cake build-up video, analyzed in terms of their distance to the membrane, and differentiated in terms of the above-mentioned avalanche-like movements and single-particle movements. The dashed line shows the continuous filter cake growth over time. Wall effects and non-uniform cake thicknesses are

excluded by omitting the particle movements in the upper 300 and lower 100 pixels of the images, such as indicated in the grayed areas in Fig. 2.1c and d. Movements close to the cake surface during the initial attachment of incoming microgels also appear bright (compare to Fig. 2.1c next to the cake boundary line). As those microgels have fewer neighbors and higher freedom of movement, rearrangement in this region is observed with each inflowing microgel. However, these movements do not play a decisive role in the filter cake's morphology and are therefore also omitted. Hence, Fig. 2.1e shows a white gap between the filter cake surface and the defect positions.

At the beginning of the experiment, during the first 10 minutes, the system represents a homogeneous state. Rearrangements are initiated by flow-induced mechanical agitation, such that single-particle and avalanche-like network movements are both occurring and evenly spread over the whole filter cake. Several events cluster simultaneously in a short time, suggesting that rearranged microgels open novel voids subsequently filled by the following microgels. With ongoing filtration time, the defect positions shift towards the cake surface, as seen in the grayed region 1 of Fig. 2.1e. This shift indicates that the total number of rearrangements in a layer is limited. Each rearrangement increases packing density towards the membrane, reducing remaining voids and further rearrangements become unlikely. Region 2 shows a decreased probability of avalanche-like network movements. The packing density is already on a high level, and load-bearing microgels have found their stable position, such that only local single-particle movement of non-loaded microgels occurs.

2.3.2 Cake mobility during compression and relaxation

The compression behavior of the filter cake is investigated by performing a pressure stepping experiment. The buildup has been executed by applying constant pressure before. For pressure stepping, the pressure is raised three times by 50 mbar and then lowered again three times as illustrated in Fig. 2.2a. This procedure is repeated twice, enabling a differentiation

between uncompressed (Fig. 2.2b) and compressed initial state. To further analyze the cake behavior at elevated pressures, the filter cake thickness change, relative to the initial position 1, $(h_1 - h_i)/h_1$, is measured for each pressure step (Fig. 2.2c). In the uncompressed state, the relaxation does not follow the compression, while in the compressed state, the relaxation follows the compression.

Compared to the results from cake mobility during the buildup, two parallel phenomena occur in this experiment; irreversible rearrangement and elastic compression. The flow-induced rearrangement changes the internal morphology towards an increased order and higher packing density without reversing during relaxation. The elastic compression deforms the soft microgels and reverses during compression. Accordingly, in the initial compression, the filter cake rearrangement dominates step 1 to step 3, while all other steps and the second cycle mainly show elastic deformation. This result underlines the importance of a soft filter cake's compression history and its decisive influence on its morphology and cake properties.

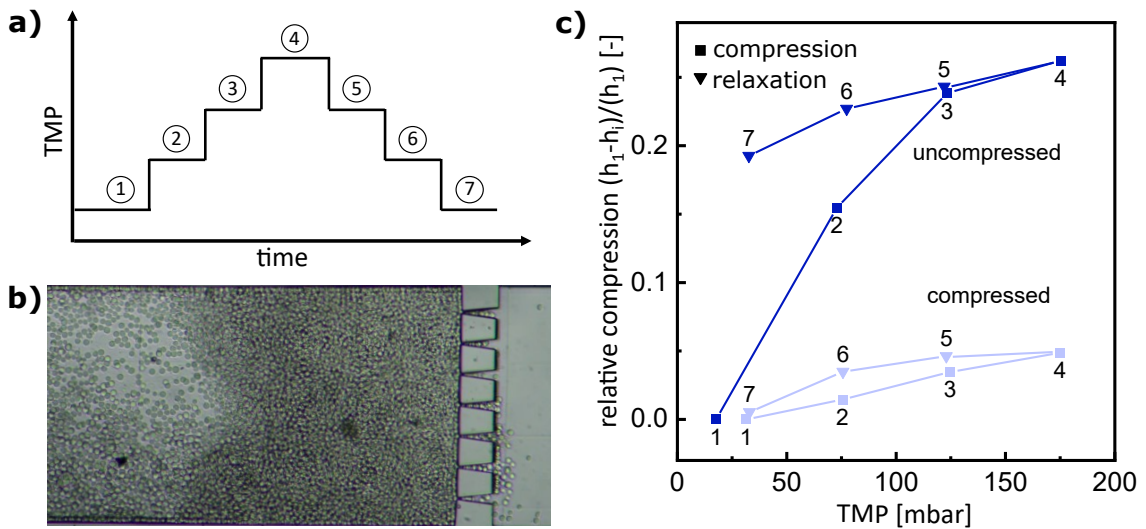


Figure 2.2: Cake thickness during pressure stepping experiment. Experimental procedure of the applied transmembrane pressure (TMP) steps (a). Light microscopy image of the microfluidic membrane channel and the filter cake during pressure step 1 (b). Cake compression relative to the initial thickness $\frac{h_1 - h_i}{h_1}$ of an uncompressed and a previously compressed filter cake during pressure stepping experiments (c).

The images of the seven compression states are analyzed in the pre-

viously uncompressed cycle by generating spatial descriptive heat maps, displaying the movements inside the cake (Fig. 2.3). Therefore, the image of a specific compression level is subtracted from the previous compression level (Fig. 2.3a, b), so that bright areas in the image highlight the regions with the morphological change, while dark regions are unaffected by the compression and relaxation. Additionally, these cake movements are plotted by accumulating the heat map average pixel counts (Fig. 2.3c). Accordingly, the Figure shows the brightness in different x-slices in the cake, representing the mobility at that specific position.

The heat map of the first compression c_1 is brightest with two peaks at the filter structure ($0 < d_m < 200$) and the filter cake surface ($750 < d_m < 1000$). At the peak at the membrane structure, the particles rearrange severely by filling up voids. This rearrangement leads to a large change in the total filter cake thickness, as shown in Fig. 2.2c, step 1-2. These movements are transferred to the following layers, such that the overall brightness is high. The brightness peak at the cake surface is due to a reordering of a very loosely packed layer in front of the cake, which emerged during the initial cake built up at low pressure. In the following compression curves (c_2 and c_3), the near-membrane peak moves towards the cake center, decreasing the overall brightness. This brightness decrease indicates that rearrangement is reduced and that it mainly occurs distant from the membrane.

During relaxation (r_1 , r_2 , and r_3) only elastic deformation occurs, such that the heat maps are generally darker. However, the last relaxation step shows a higher movement in all layers compared to the two recent steps. This brightness difference nicely confirms the findings from Fig. 2.2, where the compression gradient between step 6-7 is more extensive than between step 4-5 and step 5-6.

This analysis confirms the findings from Fig. 2.2, that the cake movement during compression is more prominent than during relaxation. Additionally, it shows that the rearrangement begins at the membrane surface and evolves towards the center of the cake. The layers close to the membrane experience the highest compression, such that they reach the state of geometrical frustration with exclusive elastic deformation. Further pressure

increase enlarges the mechanical agitation and the driving force of particles towards the membrane, such that the layers distant to the membrane also rearrange towards the frustrated state. In relaxation, the frustrated state remains, while the microgels reform elastically towards a sphere.

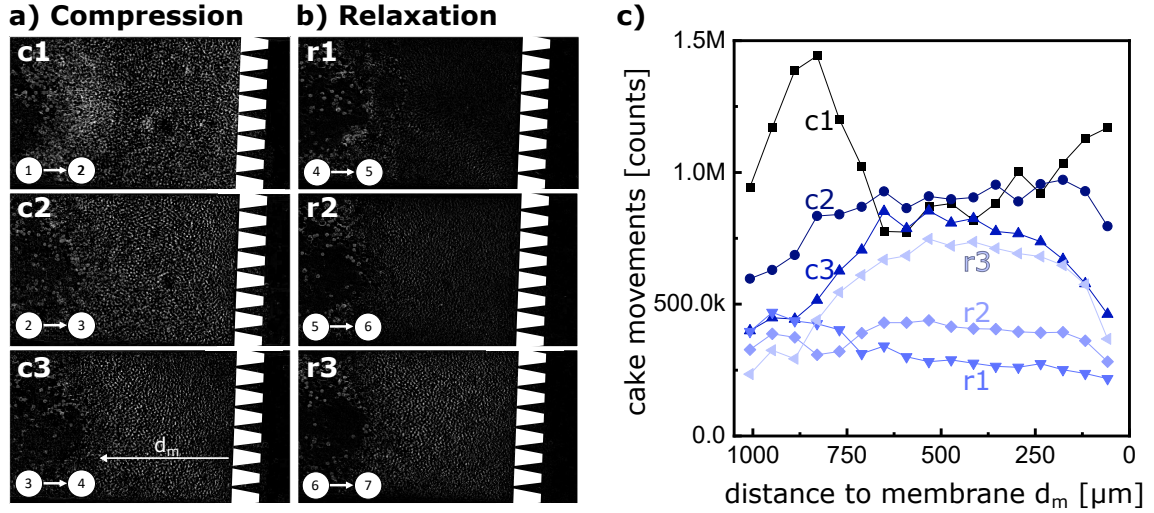


Figure 2.3: Spatial resolution of the pressure stepping cake mobility. Compression (a) and relaxation (b) heat maps revealing cake movements during the pressure stepping experiment from Fig. 2.2 uncompressed. Heat map comparison illustrating spatial resolution of cake movements at different compression and relaxation steps (c).

CFD-DEM modeling

The microfluidic experiments were accompanied by coupled CFD-DEM simulations investigating the filtration and the compaction of soft particles. Details about the simulation method and conditions are described in the supplementary part. The simulations were performed in a two-step process. First, soft particles are filtered with a constant transmembrane pressure (TMP) of 17 mbar on a particle-impermeable membrane. In the simulations, the particle's softness is reflected in a low Young's modulus of 50 kPa, which is adapted from values that can be found in literature for PEG-DA based hydrogels [Peyt2006]; [Herr2013]; [Anse2015]; [Teme2002]. The softness enables the particles to interpenetrate partly.

A hydrodynamic resistance is integrated into the simulation's CFD part, resulting in a pressure loss in the porous filter cake structure at permeation.

The particles build up a filter cake with a height of roughly 250 μm . The resulting filter cake is shown in Fig. 2.4a. The filter cake exhibits two important characteristics of a soft filter cake: cake compaction accompanied by increased coordination closer to the membrane. Fig. 2.4d (pre-compression) highlights the compaction behavior of the filter cake. The average penetration depth is chosen as a measure for compaction of the filter cake. Since the pressure on the particles raises closer to the membrane, the penetration depth increases. Besides the compaction, the average coordination number increases towards the membrane indicating a more ordered morphology until the coordination number drops off for steric reasons at the membrane boundary.

After filtration, the filter cake is briefly compressed with a higher TMP of 175 mbar. The higher TMP causes the filter cake to compact drastically, as shown in Fig. 2.4. The cake height roughly reduces to half. After compaction, the filter cake is relaxed again to the TMP of 17 mbar. Back to post-compression steady state, the average penetration depth is increased compared to the pre-compression steady-state, highlighting the filter cake's irreversible behavior. Further minor changes in the average coordination can be detected. The irreversible compaction shows similarities with the pressure stepping experiments presented in Fig. 2.2c. In both, the simulation and the experiment, the cake remains more compacted after the compacting step. However, the increased compaction is not as pronounced in the simulation, perhaps due to the simulation domain's limited size. The avalanche-like, funnel-shaped changes in the filter cake seen in the experiment are restricted to the simulation domain's limited size. Larger simulation domains would be necessary, but the simulation effort is currently still too high.

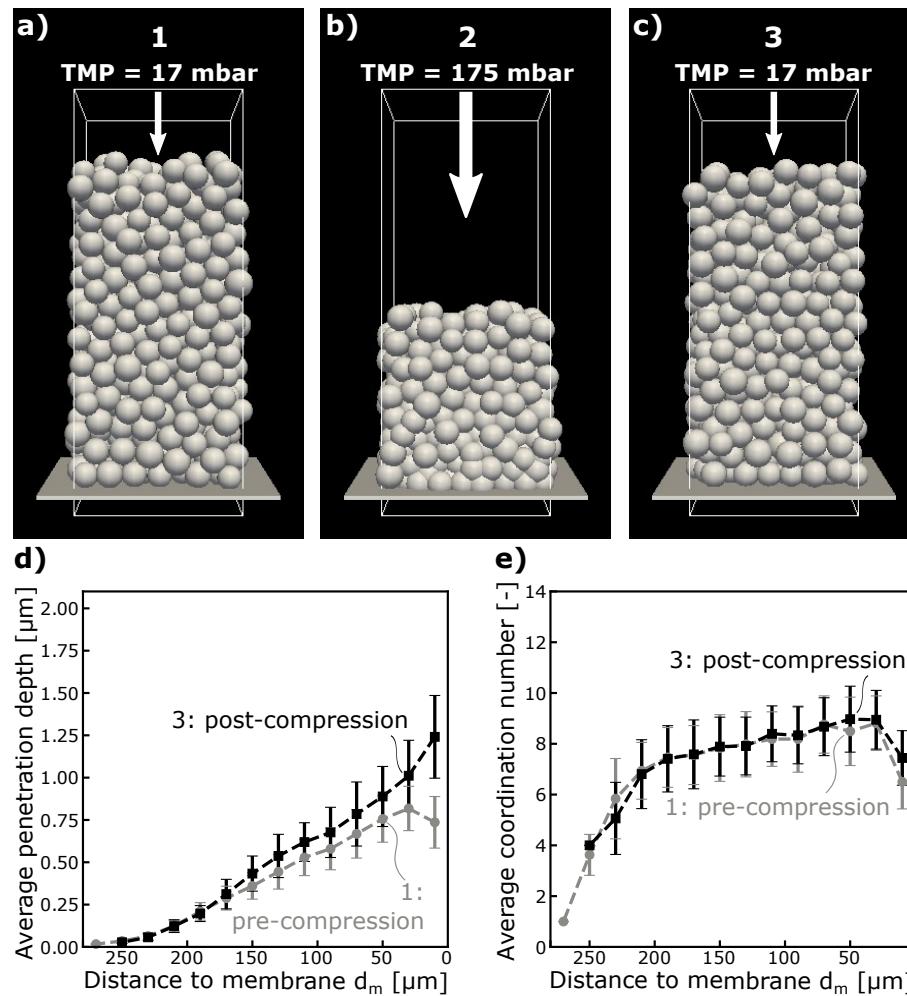


Figure 2.4: CFD-DEM modeling of cake compression with the visualization of the three conditions (a,b,c). The average penetration depth (d) and the average coordination number (e) of the particles is compared for the pre-compression (grey circles) and the post-compression (black squares) condition.

2.4 Conclusion and Outlook

This study analyzes the movements of soft microgels inside microfluidic filter cakes. First, soft spherical PEG microgels are fabricated by emulsion polymerization. These particles are then filtrated in microfluidic channels at a porous structure, so that the microgels are fully retained and form a porous filter cake. The evolving filter cakes shows single-particle movements inside the assembly during constant pressure cake buildup, which can be classified according to their influence on the overall cake morphology. After rearrangements of single particles or whole particle networks in

the filter cake, the deeper layers come to rest, forming a stable set of geometrically frustrated layers. The filter cake stabilizes gradually towards the cake center, starting with the layers close to the membrane.

Additionally, this study analyzes the filter cake's compression and relaxation and divided the deformation behavior between a rearranging and an elastic fraction. In the rearranging fraction of the compression, the single microgels fill up voids between other microgels and change their morphological position in the filter cake. In the elastic fraction, the microgels deform while staying in their same morphological position. At the very first compression of a filter cake both, rearranging and elastic deformation can be found. In contrast, during relaxation and repeated compression, the filter cake only deforms elastically. Furthermore this study analyzes the spatial resolution where the compression and relaxation occurs. It can be concluded that rearranging compression develops from the near-membrane layers towards the center of the cake, confirming process-known gel layer formation at the membrane boundary. Finally, CFD-DEM modeling confirms the experimental findings of a combined reversible and non-reversible compression. The results reveals different average penetration depths and coordination numbers before and after a compression step. The presented simulations are a first step to evaluate the microscopic dynamics of soft filter cakes by single particle modeling. This first phenomenological analysis neglects the influence of the surface charge, since the particle's charge of -12.7 mV is minor. For future studies, it would be of great interest to refine the model in terms of the influence of surface charge and its interactions on the soft filter cake mobility. Additionally, a more detailed description of the mechanical properties [Berg2018a]; [Gnan2019] of the particles, including an experimental measurement of the elastic properties [Lu2001a]; [Liét2011]; [Hash2009]; [Sier2011]; [Wyss2010] would be desirable.

This study relates single microgel properties to the overall filter cake behavior and gives insights into the events occurring during soft matter filtration inside a filter cake. It underlines the importance of the compression history related to the morphological properties of a soft filter cake and the gel-layer formation process. Additionally, the findings might be used to eval-

uating soft filter cake models. In the future, further experiments, including flux measurements, might link the here presented cake morphology to the permeation resistance and allow predictions of the impact for real filtration processes.

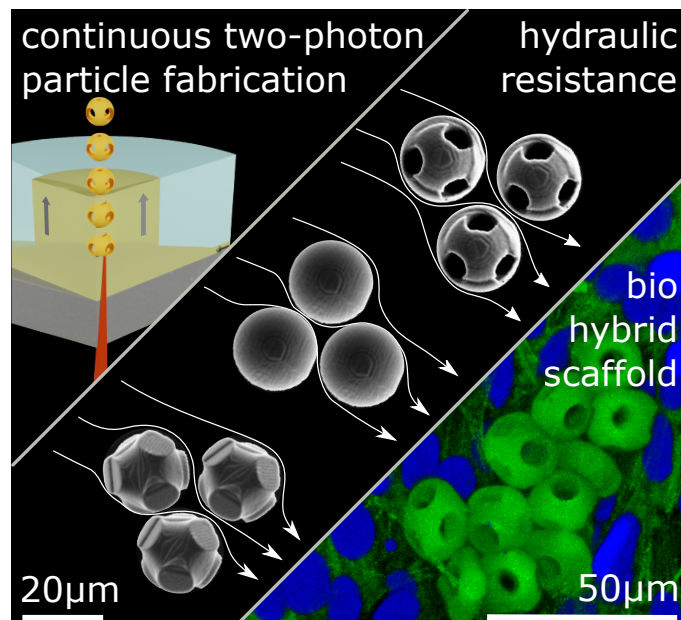
3 Filter cakes and assemblies made from any-shape micro-particles

Parts of this chapter have been published as:

Arne Lüken, Lucas Stüwe, Sebastian Bernhard Rauer, Jesco Oelker, John Linkhorst, Matthias Wessling

Fabrication, flow assembly, and permeation of microscopic any-shape particles, SMALL 18.15, 2022, 2107508

DOI: <https://doi.org/10.1002/sml.202107508>



3.1 Introduction

Filtration of particles in MF results in cake layer formation, which is being permeated during the filtration process. Modeling and predicting filter cake permeation is to date based on the the Karman-Kozeny equation, estimating a porous assembly of rigid spheres [Fole2006] (see Section 1.3.4). This chapter analyzes the assembly and the permeation of differently shaped particles as filter cake. This topic is hardly considered in the field of membrane research, though, it is well studied for larger scale non-isotropic particles as filling in biochemical reactors. Therefore, this chapter gives an introduction to the assembly and permeation of non-isotropic particle assemblies in bioreactors.

Surface active bioreactors tailor biomanufacturing processes by immobilizing enzymes, cells or microorganisms on the surface of the reactor filling. Additionally, they serve as a scalable technology, transferring batch towards continuous processes [Kiss2018]. The biochemical reaction is performed in living cells on the surface or catalyzed by the immobilized enzyme on the surface, making the surface to volume ratio the main factor affecting the process efficiency [Anto2012]. Hollow fiber membrane bioreactors [Pire1990]; [Eghb2016] and packed-bed bioreactors [Meuw2007] both show high surface to volume ratios and are therefore the two established reactor types in industrial processes. Tuning the properties of the particles used in packed-bed reactors as filling defines the desired reactor characteristics. These particles' properties range from the material with a specific surface charge, softness, or rigidity to the macroscopic structure with particular particle size, shape, and desired surface roughness. The particles' properties affect the biological environment, including the adhesion and development of cells, and the engineering performance indicators, such as the hydraulic resistance, the packing density, and the surface to volume ratio. E.g., the particle softness affects the cells adhesion [Dias2017] as well as the flow-dependent compressibility of the packed bed, which increases the pressure loss, just as filter cake permeation during MF.

The influence of particle shape on pressure drop, permeability, and ac-

tive catalyst surface is also applied on a larger scale at fixed bed reactors for particle sizes of several centimeters. By tailoring particle shapes, from spherical to cylindrical, tubular or more complex-shaped particles, the hydrodynamic pressure drop and the active surface area are tailored for the specific application in experiments [Brun2015] as well as in simulation [Flai2019]. Such irregular assemblies of porous any-shape particles are a promising alternative to applications of periodic open cellular structures (POCS) as a fixed bed. The POCS geometry allows predicting and tailoring of the hydrodynamic properties, including the pressure drop [Klum2014]; [Lämm2018]. However, tailoring any-shape particle assemblies' porosity and pressure drop holds great benefits regarding automated fabrication, process adjustment, and installation. For bioprocessing and tissue engineering applications, double-digit micrometer-sized particles enhance the surface-to-volume ratio and allow cells to interact with the geometrical structures of similar-sized obstacles. Several fabrication techniques are applied in research to fabricate such complex-shape micro-particles and can be structured in batch fabrication, horizontal-flow lithography and vertical-flow lithography. Batch fabrication includes molding techniques for rods [Roll2005]; [Rose2017] and 3D printing of complex 3D particles on a static substrate using 2-photon polymerization [Dohe2020]. These batch techniques are not suited for continuous fabrication and are therefore hardly up-scalable.

Microfluidic horizontal-flow lithography enables the fabrication of anisometric particles by exposing light perpendicularly into a photoresin-filled channel. For example, rod-shaped particles can be fabricated by centering the photo resin by a jet and pulsating a spotlight source [Krüg2019]. More complex 2.5D particles can be fabricated by projecting photo-masked--shaped parallel light into a channel, which is filled with the liquid photo-resin so that particles are formed in the shape of the light beam, and the height of the channel [Dend2006]. This technique is applied for various materials [Wolf2020] and flow interruption during particle formation improves its resolution [Dend2007]. In addition, high-resolution 2-photon polymerization can be applied in a horizontal flow for the fabrication of 3D particles by

correcting the laser pathway in flow-direction depending on the print-time [Shaw2018].

Rotating the illumination direction parallel to the fluid flow results in vertical flow lithography, which was implemented with a stop-flow set-up using UV-projection [Haba2015]. However, high-resolution in-flow printing is only possible by moving the polymerization level away from the channel walls inside the center of the laminar flow profile. Lölsberg et al. suggested this technique by applying two-photon polymerization in the vertical flow and fabricating high-resolution micro-tubular structures with sub-micron-sized porosities [Löls2019].

In today's state-of-the-art particle fabrication technologies, the production of any-shape particles in a reasonable size range is hindered regarding 3D complexity, resolution, and throughput. Therefore, the analysis of hydrodynamic properties of rigid and soft micro-particle packings in model filter cakes, as well as in other applications, such as packings in bio-reactors or scaffolds in tissue engineering is to date limited to spherical particles [Link2016]; [Link2019]; [Bouh2017].

This study applies the vertical flow two-photon lithography (VFL) technology [Löls2019] in a continuous process for fabricating complex 3D shaped particles from rigid and soft materials for tissue engineering applications. By printing specific amounts of particles into microfluidic channels, this study combines the knowledge of the particle amount with visual observations and hydrodynamic resistance data. Accordingly, this study tailors the hydrodynamic properties, the packing density, and the compressibility of packed bed filter cakes, by engineering the single particle's 3D shape. For the application as scaffold, first cell culture results disclose bio-compatibility and a manifold interaction of cells with the particles.

3.2 Experimentals

Microfluidic device fabrication The microfluidic channels for vertical flow lithography fabrication as well as the hydrodynamic analyses were both fabricated as described by Lölsberg et al. [Löls2018]. A negative structure of

the channel is printed onto a glass substrate (Carl Roth, 25 x 57 x 1 mm) using two-photon direct laser writing (Nanoscribe GmbH, Photonic Professional GT2) and fully polymerized using an ultraviolet light source (302 nm, 8 W). The structure is afterward molded using PDMS elastomer (Dow, SylgardTM184 Silicone Elastomer Kit) and holes are punched (Rapid-Core 1.2 mm) into the PDMS mold for tubing connection. After cleaning by ultrasonication in isopropanol (Carl Roth, 99.5 %) the mold is bonded to a 170 μm thick microscopy cover slide applying an absolute oxygen pressure of 0.3 mbar at 60 W for 30 s (Diener, Zepto model 3 Plasma System).

Continuous vertical flow direct laser writing The continuous vertical flow channel and process was adapted from Lölsberg et al. [Löls2019]. The printing files were prepared by first constructing a 3D object of the particle (Autodesk, Inventor 2021), slicing the stl design using the Describe software (Nanoscribe, Describe 2.5.5) (solid, slicing 0.6 μm , hatching 0.3 μm), and subsequently processing the gwl file for VFL using a python script, which performs two processing steps (supplementary file S1). First, the script removes all z-movements from the gwl file because the moving fluid performs the z displacement. Second, it adjusts the print-time of each layer to the same value by adding wait commands for each printing layer. Elsewise, small cross-section layers with short print times would reduce the z-height compared to large cross-section layers. The liquid resin is flushed into the channel using a syringe pump (Harvard Apparatus, PHD ULTRA) and a syringe (SGE Gas Tight, 2.5ml) with a flowrate of 17 $\mu\text{l/h}$. The syringe is connected to the microfluidic chip using FEP tubing (Darwin Microfluidics, OD: 1/16" ID: 1/32"). The outlet tubing (Smiths Medical, fine bore polythene, OD: 1.09 mm, ID: 0.38 mm) transfers the liquid resin and solidified particles into a 1.5 ml tube (Eppendorf, 1.5ml). The particles are printed alternating at two positions with a particle distance of 20 μm , ensuring that particles do not attach to each other (Supplementary Video S2). The harvested sample is developed and separated from the liquid resist by dilution, centrifugation, and subsequently pipetting the supernatant. This procedure

was repeated three times using 1-Methoxy-2-propyl-acetat (Sigma Aldrich, 99%) (10.000/s, 10 min) and six times using Isopropanol (Sigma Aldrich, 99%) (5.000/s, 5 min).

In-channel particle fabrication The hydraulic resistances of the assemblies were measured by printing the particles inside a microchannel inside the analysis domain with two filter structures having a size of H/W/L of 100/300/3000 μm (see Figure 3.2). The microfluidic PDMS channel was manually filled with the photoresist (IP L or IP PDMS, Nanoscribe GmbH) using a syringe and then placed in the two-photon printer (Nanoscribe GmbH, Photonic Professional GT2) in oil-immersion mode using a 25x objective. The resist was given 30 minutes to rest to avoid currents caused by the filling. The particles were sliced using the Describe software (solid, slicing 0.6 μm , hatching 0.3 μm) and printed (scan speed 60000 $\mu\text{m/s}$, laser power 36%, z-direction downwards) as an array with a distance of 25 μm away from the membrane structure (Figure 3.2). (supplementary Video S3) The filtration experiments were prepared by removing the liquid photoresist by flushing solvent through the channel using a constant pressure pump (Elveflow, OB1 Mk3+). First, tubing and channels were filled with the new solvent by flushing from inlet 1 to outlet 1 and inlet 2 to outlet 2. Afterward, both outlets were closed, and the solvent was flushed from inlet 1 to inlet 2. The rigid IP L particles were developed using first Acetonitrile and afterward Isopropanol as filtration fluid. The soft IP PDMS particles were developed using ethanol as a developer and as a working fluid. The Young's Modulus of the materials was taken from the material's datasheet.

Hydrodynamic filtration experiments A reservoir containing the working fluid was connected to the constant pressure pump. In between the reservoir and the microfluidic chip two flow sensors (Bronkhorst Coriolis Flow Rate Sensor, Elveflow, Microfluidic Flow Rate Sensor MFS2, Elveflow) and a pressure sensor (Microfluidic Pressure Sensor MPS1, Elveflow) were installed and connected via FEP tubing. All flow data presented

in this study were measured using the MFS2 sensor. The outlet channel of the chip was connected to a waste reservoir. During filtration experiments, the filter cake was situated on an optical light microscope (Leica DM IL LED, 10 x objective) and recorded using Basler Video Recording Software. The filtration experiments were conducted immediately after the development using IPA (IP L) and ethanol (IP PDMS) as the working fluids. For this purpose, the two outlets were closed, and the pressure was set to 50 mbar. After particles accumulation at the filter structure, the pressure controller was increased to 200 mbar, resulting in a TMP of approx. 150 mbar and reduced step-wise in 30 mbar steps. This procedure is here defined as one filtration cycle. After each filtration cycle, the filter cake was backflushed and sonicated for 5 min (Elmasonic xtra TT) to re-disperse the particles. The filtration cycle was repeated three times for each experiment. The pressure and flow data for each pressure step were obtained by taking the average from the last 10 seconds corresponding to 19 data points. Additionally, a corresponding image was taken from the filter cake.

Particle volume fraction The particle volume fraction was calculated with

$$\phi_p = \frac{V_{p,total}}{A_{FC} \cdot h_c} \quad (3.1)$$

where ϕ_p is the particle volume fraction at the highest pressure step, $V_{p,total}$ the total volume of all particles in the cake, A_{FC} the x/y area of the filter cake, and h_c the height of the channel (100 μm). A_{FC} was manually measured for all filtration experiments from microscopic images of the respective first filtration cycle at the highest pressure step using ImageJ. The total particle volume of the spheres with holes was calculated without considering the holes.

Cell culture The interaction of particles with L929 mouse fibroblast cells was investigated in self built PDMS wells. PDMS and crosslinker (Dow, Syl-

gardTM184 Silicone Elastomer Kit) were poured in a petri dish in a ratio of 10:1 and were cured at 60 °C overnight. Subsequently, a PDMS slab was cut out from the petri dish, and wells were integrated using a 4 mm biopsy puncher (EMS, Rapid-Core 4.00 mm). The PDMS slab was then plasma bonded to a microscopy cover slide applying an absolute oxygen pressure of 0.3 mbar at 60 W for 30 s (Diener, Zepto model 3 Plasma System). Finally, the PDMS wellplate was sterilized at 121 °C for 20 min (SystecTM VX-95). 20 µm sized spherical particles with 8 µm holes were printed using continuous vertical flow direct laser writing using biocompatible IP-VISIO resist (Nanoscribe GmbH & Co. KG). The low auto-fluorescence of the IP-VISIO resist is advantageous for laser-based imaging applications. Particles suspended in isopropanol (Sigma Aldrich, 99%) were added to the wells and the isopropanol was evaporated at room temperature under sterile conditions. Subsequently, the wellplates were washed multiple times with sterile MilliQ water. Finally, they were incubated over night in Roswell Park Memorial Institute (RPMI) 1640 medium (4500 mg L⁻¹ glucose, L-glutamine, sodium pyruvate, sodium bicarbonate) supplemented with 10% v/v fetal bovine serum (FBS) and 1% v/v penicillin streptomycin. Cells were seeded at a concentration of 10 000 cells per well. After four days of cultivation, the cells were fixed in 4% v/v paraformaldehyde (PFA) for 15 min, permeabilized in a 0.1% v/v Triton X-100 solution for 15 mins and rinsed thoroughly in phosphate-buffered saline (PBS 1x). For the analysis of cell-particle interactions, the cells were stained for nuclei and F-actin by exposing the specimen to DAPI solution (Abcam, United Kingdom) for 5 min and Phalloidin-iFluor 488 reagent (Abcam, United Kingdom) for 120 min. Finally, the samples were imaged using a TCS SP8 Falcon confocal microscope (Leica, Germany).

3.3 Results and Discussion

3.3.1 Continuous vertical flow any-shape particle fabrication

3D any-shaped particles with 20 μm diameter are synthesized continuously using a vertical flow lithography process. The channel design of Lölsberg et al. [Löls2019] enables 3D any-shape particle synthesis by moving a 2-photon laser in a single xy-plane while the flow transports the printed xy-slice continuously in the z-direction (Figure 3.1a, b). The print time of each xy-slice is adapted to the flow rate by adding a wait command depending on the trajectory length of the laser path using a python script (supplementary Figure S1). This script additionally removes all z-movement commands from the print file, so that Nanoscribe's "Describe" software can be used to slice complex geometries.

The printing layer inside the outlet channel is located 200 μm above the glass slide and is limited by the objective's focal distance. The channel design promotes a laminar flow profile with parallel streamlines at the printing level. However, the particles' shape unravels a non-uniform flow depending on the print position. Cubes were printed in the centered symmetry axes of the outlet channel ($r=0 \mu\text{m}$), as well as at two positions further dis-centered from the symmetry axes at a radial distance of 82 μm and 165 μm . The particles were subsequently analyzed according to their height-to-width ratio as well as their shear angle α (Figure 3.1d, e). Particles printed in the center of the channel show the desired height-to-width ratio and shear angle α of 90° , while the dis-centered particles show undesired geometry (Figure 3.1: d1, d2, d3). The shifted shear angle α can be correlated to non-parallel streamlines in the print layer as a result of an undeveloped laminar flow profile and suits well to CFD simulations (Figure 3.1d). The increased height-to-width ratio of the particles printed at a radius of 82 μm is also a result of the undeveloped laminar flow profile with a ring-shaped velocity profile at the beginning of the outlet channel. The CFD simulations phenomenologically confirm the ring-shaped profile at the print position (Figure 3.1d). Still,

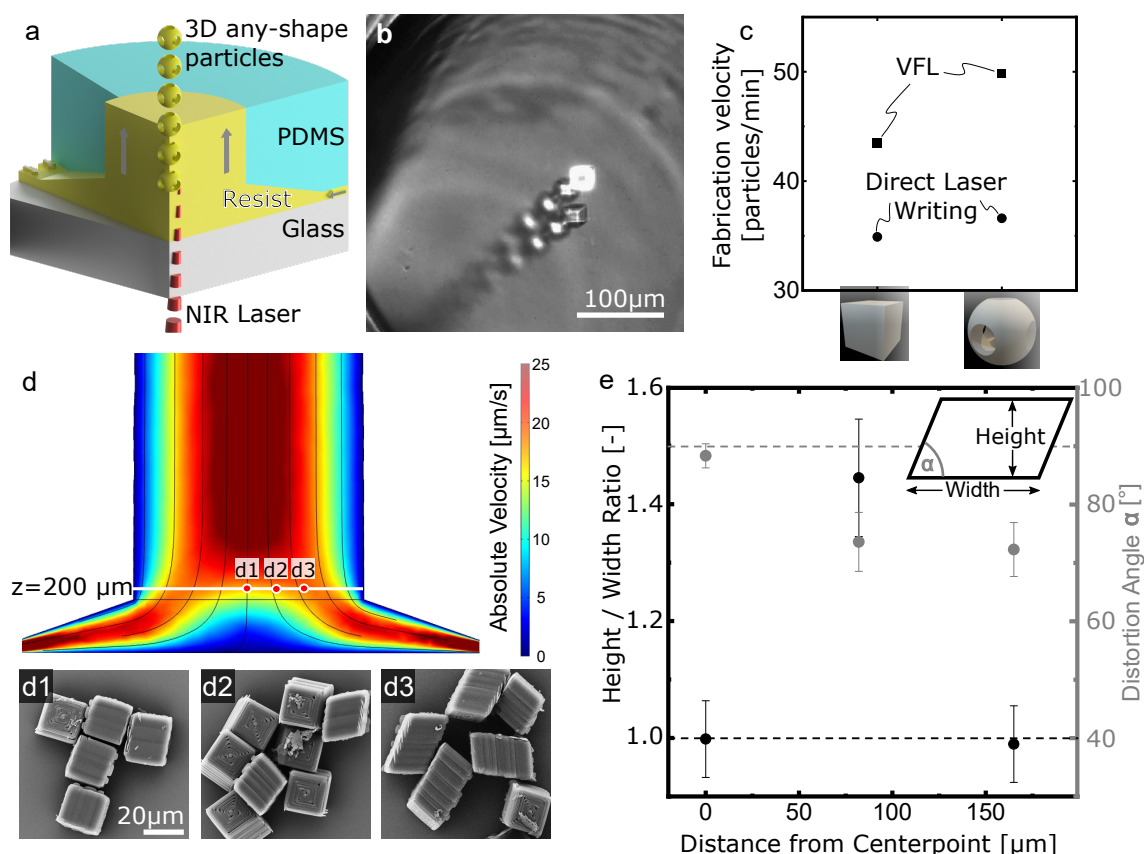


Figure 3.1: Continuous vertical flow lithography particle synthesis. (a) Visual representation of the fabrication process. (b) Micrograph of the fabrication process with two particles printed subsequently after each other. (c) Comparison of the fabrication velocity of vertical flow two-photon lithography (VFL) with traditional 2-photon lithography. (d) Cross-section of a 3D CFD simulation of the flow field and micrographs of the particles, depending on the print position (d1 at $r=0 \mu\text{m}$, d2 at $r=82 \mu\text{m}$, d3 at $r=165 \mu\text{m}$). (e) Analysis of the particles' shape at different print positions.

the relative flow velocities at the three printing positions do not match the measured particle height-to-width ratio. Hence, a precise height-to-width ratio was achieved using an iterative fabrication process with subsequent size analysis using a microscope.

Finally, this study evaluates the fabrication velocity of the VFL in comparison to traditional two-photon direct laser writing on a substrate. The particles in VFL were printed one after each other at two offset positions (Figure 3.1b) with an x/y-distance of 20 μm to prevent the particles from adhering. Thus, the particles could be printed directly in succession without waiting times between two particles. Additionally, the VFL does not perform z-movements between the printed layers, so that the printing time per single particle also decreases. Both effects result in an accelerated fabrication velocity of VFL (Figure 3.1c) in comparison to two-photon direct laser writing on a substrate. The absolute speeds depend on the particle's size, its uniformity, and the overall printed volume.

Using VFL, 3D particles were fabricated continuously by printing for 72 h resulting in more than 150 000 particles. This proof of principle showcases the potential of the automated, continuous, and scalable particle fabrication technology towards a high throughput production of 3D structures and discloses micron-sized any-shape structures to the next level of potential applications.

3.3.2 Permeation of any-shape particle tissues

Microfluidic encapsulation of any-shape particles

This study analyzes the hydrodynamic permeation properties of any-shape particle assemblies by encapsulating free-flowing 3D particles inside a microfluidic channel. Filter structures at the inlet and outlet withhold the particles in the observation and analysis domain (Figure 3.2c). The particles were fabricated directly inside the analysis domain by two-photon printing in a steady standing fluid (Figure 3.2b), enabling precise control of particle material, size, shape and amount. After the printing process, the remaining liquid resin was removed by flushing developer solvent and afterward

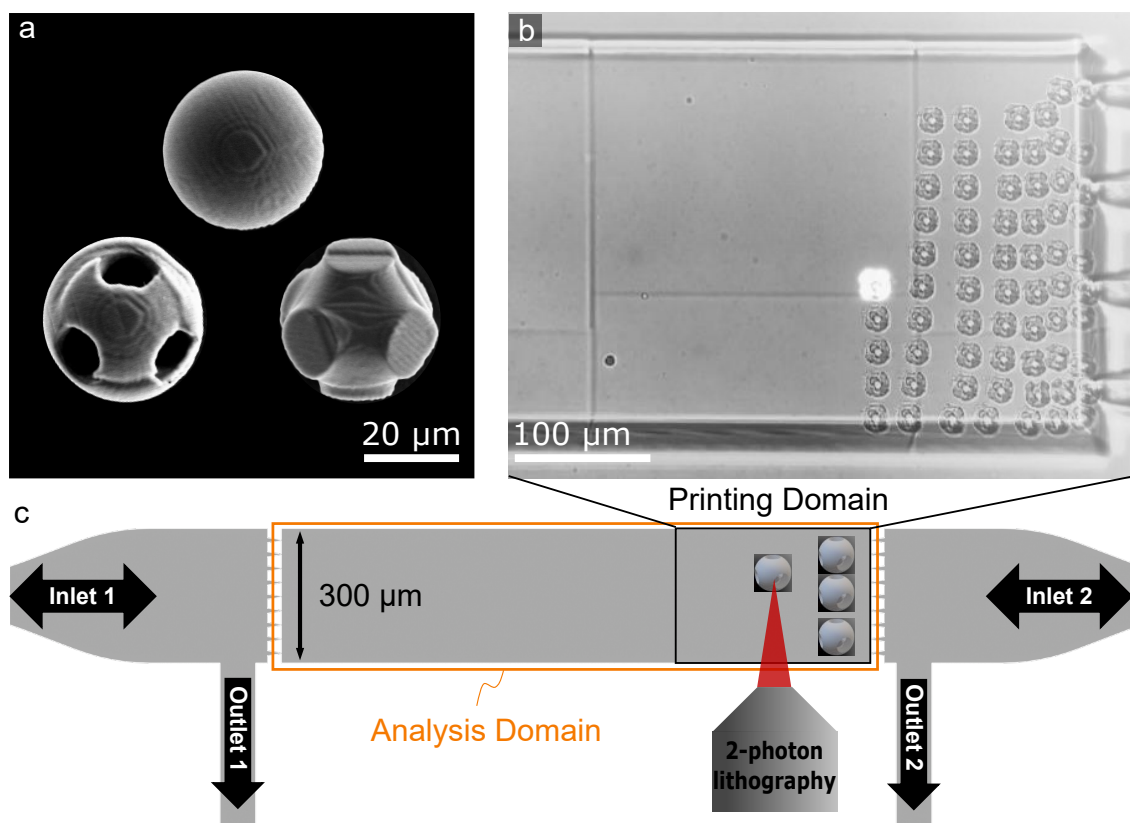


Figure 3.2: Direct 3D particle in-channel fabrication by two-photon printing of any-shape particles (a) in a non-moving fluid (b). The channel design encapsulates the any-shape particles by two filter structures at the inlet and outlet (c).

filtration fluid through the whole channel system (see methods for details). For analyzing the particles' influence on the hydraulic resistance of an assembly, three different particle shapes were chosen: Spheres ($d=20\ \mu\text{m}$), porous spheres with $8\ \mu\text{m}$ holes along all axis ($d=20\ \mu\text{m}$), and P-Schwarz Triple Periodic Minimal Surface (TPMS) unit cells ($d=20\ \mu\text{m}$) (Figure 3.2a). Additionally, polydisperse particles with a pyramid-distributed size range from $10\ \mu\text{m}$ to $30\ \mu\text{m}$ were filtrated (details in supplementary Figure S4). The particle's softness was modified by applying a rigid material with a Young's Modulus of $4730\ \text{MPa}$ (IP-L) and a soft material with a Young's Modulus of $15.3\ \text{MPa}$ (IP-PDMS). The $20\ \mu\text{m}$ sized soft spheres with holes squeezed through the filter structure, though, the diameter of the soft particles was increased to $40\ \mu\text{m}$.

Repeatability of permeation experiments for rigid and soft particles

The permeation experiments were performed by increasing and subsequently releasing the feed pressure in small steps from 20 mbar to 150 mbar and measuring the flow permeating the packed bed of particles over three cycles (Figure 3.3b, e). The assembly was in-situ visualized in a brightfield microscope (Figure 3.3a, d) and the relative compression of the assembly was evaluated by image analysis (Figure 3.3c, f). Finally, the void fraction of the assembly was calculated by knowing the exact amount of encapsulated particles in the analysis domain and the filled volume.

The encapsulation of particles between two filter structures enables a repetition of the permeation cycles with the same particles by forward- and backward flushing. This experimental design is outstanding for such microfluidic experiments, where the amount of particles, particle movements, and permeation control is hardly repeatable due to the small permeation volumes [Bouh2020]. The here presented experimental setup allows to accurately determine the particle number and shape and also allows to optically study the filtration process in-situ and couple this to specific resistances of the particle assembly via flux and pressure data. This approach is unique in the application of microfluidic 3D particles for the determination of hydraulic resistances. The experimental procedure includes three permeation cycles, each with a backflushing and ultrasonication cycle in between, re-dispersing the particles.

The rigid spheres show repeatable flow rates and compression curves during all three cycles (Figure 3.3a-c). The soft particles show an increased variation in the flow, primarily upon the first permeation cycle. The measured flow is higher during pressure increase (Figure 3.3e) than during pressure release. The compression curve (Figure 3.3f) supports the flow measurement by an irreversible relative compression of 10 %. Although the flow measurements represent similar results of the second and third permeation cycle (Figure 3.3d), re-dispersion was not entirely successful creating agglomerates affecting the assembly's formation process (Supplementary Figure S5). Accordingly, the compression curve during re-permeation of soft particles shows mainly the irreversible share of the

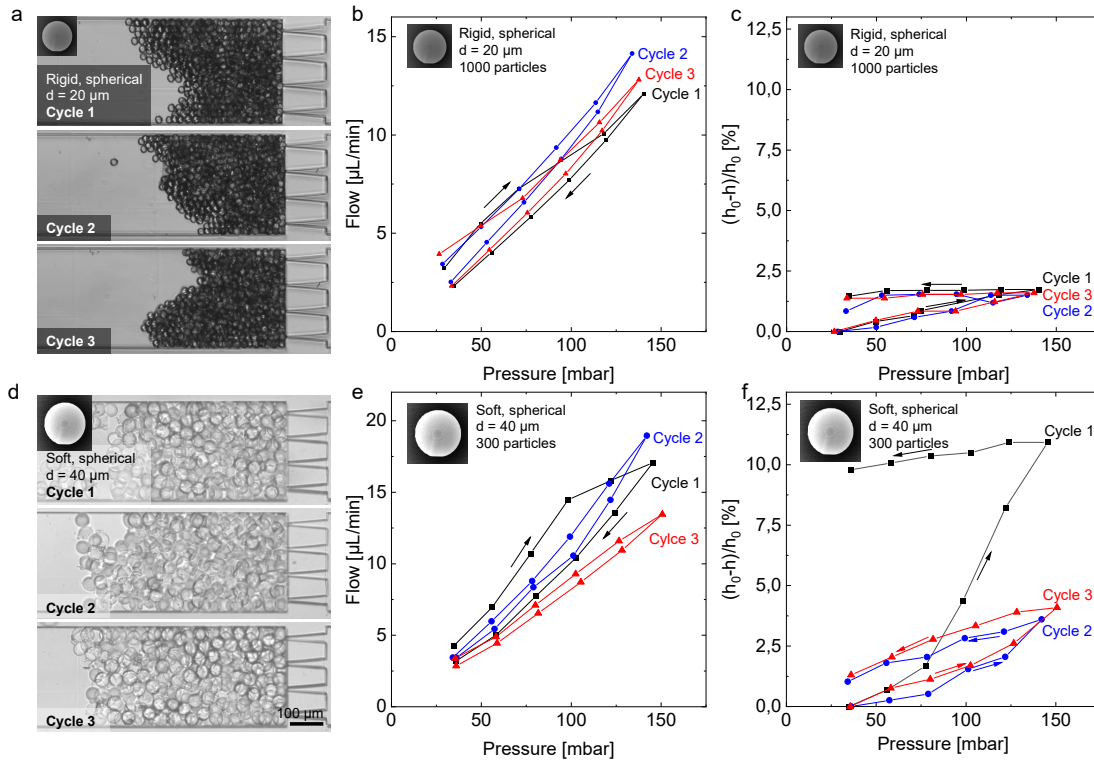


Figure 3.3: Three permeation cycles with backflushing and ultrasonic treatment in between for rigid 20 μm sized particles (a-c) and soft 40 μm sized particles (d-f). Each cycle is analyzed by the permeating flow at different pressure steps (b,e) and the relative compression of the assembly during pressure stepping (c,f). The data from the relative compression is taken from the micrographs of each pressure step. Exemplary micrographs of the assemblies in the highest compression state show that each cycle results in a different morphology (a,d).

compression. The similar slope of all three decompression cycles confirms the theory about reversible and irreversible compression, which was similarly reported in microfluidic filtration experiments filtering soft spherical PEG particles [Lüke2021]. The phenomenon of a reversible and irreversible hydraulic resistance upon compression of soft matter was also reported for bio-films on membrane surfaces [Jafa2019]. This study illustrates the difference between hard and soft particles during compression and confirms the importance of particle rigidity upon tailoring re-orientations and the inner structure of particle assemblies.

Correlation of the hydraulic resistance and packing density to the amount of particles

The coupled in-chip fabrication and subsequent analysis method, including microfluidic encapsulation of a well-defined amount of any-shaped particles and filtration procedure, allows the investigation of different particle amounts influencing the hydraulic resistance and the packing density for rigid and soft particles. However, the assemblies' degree of agglomeration after the first permeation cycle unreproducibly affects the hydraulic resistance of the second and third permeation cycle. Therefore, only the hydraulic resistance of the first pressure cycle was taken into account. Figure 3.4a shows the permeating flux interpolated at 100 mbar trans-assembly pressure. The corresponding assemblies are visualized in the micrographs in Figure 3.4d and e.

The 20 μm diameter rigid spheres show a decreasing flow with increasing particle number (Figure 3.4a, d1 - d3). The 20 μm sized soft particle measurement with low flowrate (Figure 3.4d4) uncloses that the particle material's softness and deformability influences the hydraulic resistance significantly. The same amount of soft particles results in a 4-fold hydraulic resistance compared to the same sized rigid particles. (Figure 3.4c)

The filtrate flux equation 3.2 [Raut2004] describes the hydraulic resis-

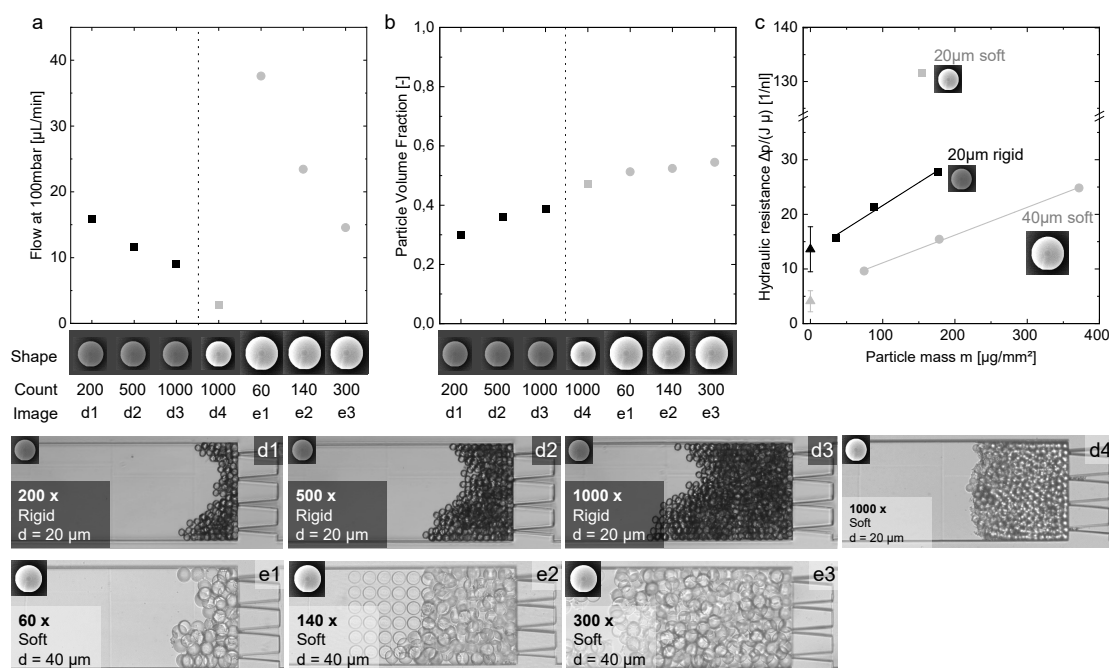


Figure 3.4: Influence of particle number on permeation flow (a), volume fraction (b), and hydraulic resistance (c) for rigid (black) and soft (grey) particles. The permeating flow (a) is interpolated for a trans-assembly pressure of 100 mbar. The volume fraction (b) is calculated from the micrographs of the corresponding experiments (d) and (e). The particle mass in (c) calculates from the particle number, it's diameter and the material density. The interpolation of the three masses represents the linear correlation. The triangles at zero-mass represent the hydraulic resistance of six individually measured empty channel resistances with the respective solvent.

tance of a filter cake on a filter structure with

$$J = \frac{\Delta p}{\mu(R_m + \alpha \cdot m)} \quad (3.2)$$

while J is the permeating flux, Δp the trans-assembly pressure, μ the fluid viscosity, R_m the filter structure resistance, α the specific assembly resistance, and m the mass of the particle assembly per unit filter structure area. Fitting this filtrate flux equation for the measured resistances for different assembly masses m (Figure 3.4c), results in a linear correlation of particle mass and hydraulic resistance. The extrapolated interception with the y-axis, R_m , indicates that the filter structure's resistance R_m has a great share of the overall hydraulic resistance. The empty channel resistances without particles were measured for six individual channels (Data in supplementary Figure S6) and added as triangles to Figure 3.4c. The different values for rigid and soft particles result from the two working fluids, isopropanol and ethanol. The two fluids had to be used to suppress the agglomeration of the particles for the two material systems. Due to the different solvent resistances, a precise comparison of rigid and soft particles is not reasonable. However, extrapolating the linear relationship of the particle mass suits the measured empty channel resistances and confirms the accuracy of the measurement.

The assembly's particle volume fraction (Figure 3.4b) is calculated by dividing the real volume of the particles by the measured assembly volume obtained from the micrographs (see experimental section). The particle volume fraction increases for increasing particle number for rigid and soft particles, indicating a denser packing. Upon permeation, a larger assembly experiences an increased drag force towards the filter structure because the hydraulic resistance of all particle layers sums up. Accordingly, particles tend to fill up voids and rearrange in the assembly towards the filter structure as shown in the study of Lueken et al [Lücke2021] and increase the overall volume fraction.

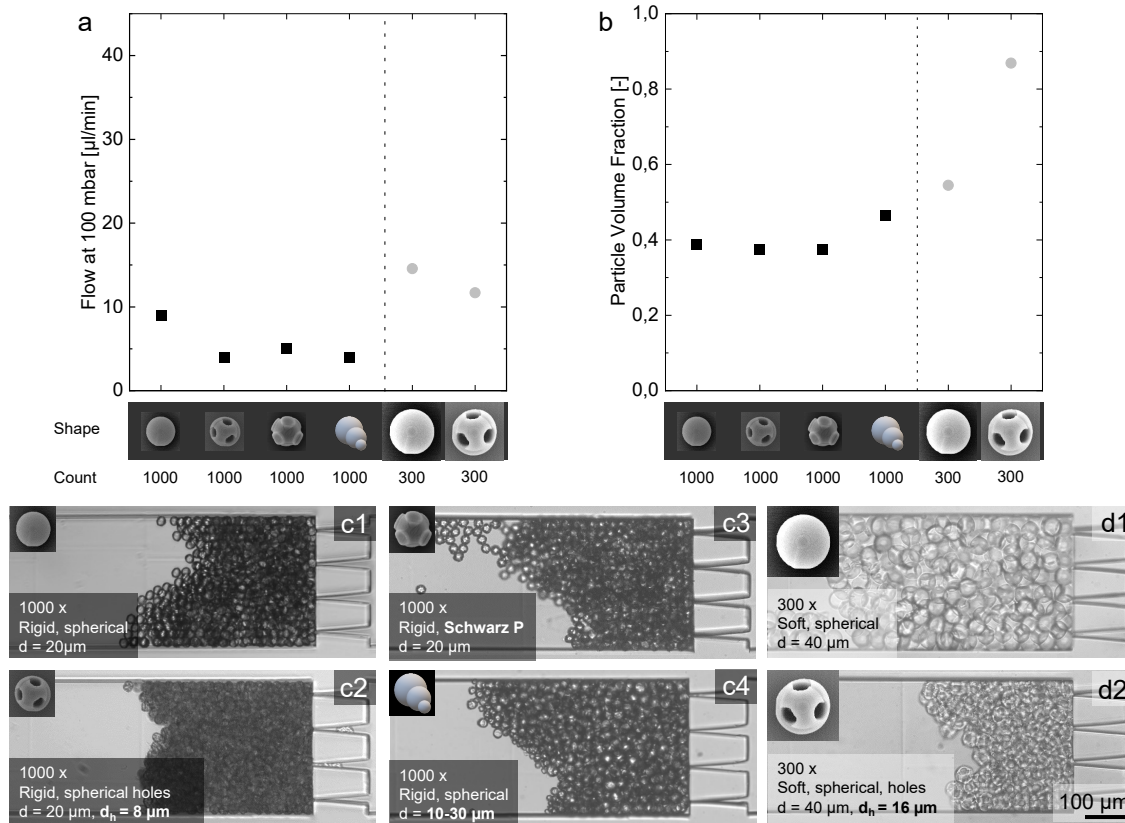


Figure 3.5: Influence of different particle shapes on flow at 100 mbar TMP (a) and volume fraction (b) for rigid (black) 20 μm sized particles in the shape of porous spheres with 8 μm holes (c2), P-schwarz unit cell particles (c3), and 10-30 μm sized polydisperse particle mixture (c4) in comparison to rigid 20 μm sized spherical particles (c1). Additionally, soft (grey) 40 μm sized spheres are compared with 40 μm sized spheres (d1) with 16 μm holes (d2).

Tailoring pressure loss by particle shape

The direct laser wiring process allows the fabrication of non-spherical 3D particles, enabling a tailored hydrodynamic resistance and packing density. This section investigates how the assembly's hydrodynamic resistance and packing density depend on the particles' shape and porosity.

Porous particles were generated by introducing 8 μm holes for the 20 μm-sized rigid particles and 16 μm holes for the 40 μm sized soft particles along all three axes and analyzed in comparison to the identical sized spheres (Figure 3.5). Rigid and soft porous particles decrease the flow upon permeation. Upon permeation of the soft particle assembly, the particles deform strongly (Figure 3.5d2), compressing the holes and increasing the

volume fraction (Figure 3.5b). However, it must be noticed that the holes are not considered in calculating the particle volume. Accordingly, for the soft particles, the holes increase the compressibility of the assembly resulting in a denser packing with smaller permeable voids but did not contribute to increased permeation. The contra-intuitive permeation data of the rigid particles with holes result from the direct contact between single particles. Spherical particles contact each other at a single point, generating large voids between the particles. The particles with holes can smoothly adapt into the ring-shaped openings of the holes from the neighboring particle. This contact reduces the distance between the particle center points and void size in the assembly, increasing the hydraulic resistance. Additionally, the ring-shaped contact increases attractive forces between particles and reduces particle mobility inside the assembly. On the one hand, reduced mobility supports non-uniformity and decreases the average particle volume fraction. On the other hand, the ring-shaped particle contact reduces the particle distance and increases the particle volume fraction. Although the reduced mobility and the reduced particle distance counteract the particle volume fraction, both phenomena superpose with the hydraulic resistance of the overall assembly. Therefore, they support the experimental data of a constant particle volume fraction (Figure 3.5b) with increased resistance (Figure 3.5a).

The polydisperse sample consists of 1000 particles with sizes from 10 μm to 30 μm (Supplementary Figure S4). The P-Schwarz unit-cell particles and the polydisperse sample behave similar to the porous spheres, increasing the hydraulic resistance compared to spheres. This phenomenon can also be related to an increased number of contact points reducing the average void size inside the assembly. The increased particle volume fraction of the polydisperse sample confirms this phenomenon.

The hydraulic resistance analysis illustrates the importance of the particle shape for tailoring the pressure loss of an assembly. Smaller particles increase the surface relative to its volume, such that the influence of attractive contact forces between particles gains importance compared to larger any-shape particles. Furthermore, the 3D shape gives an additional degree

of design parameters, including the number of contact points and contact area to tailor attractive and repulsive particle interactions additionally to the material properties, e.g., the Gibbs free energy [Zama2016].

3.3.3 Particles as cell tissue

The application of particle assemblies as cell tissue is advantageous due to the flexibility in processing, such as pipetting or injecting, and its ability to react to ambient conditions, such as a given reactor shape or a permeating flow. Furthermore, tuning the particle geometry can increase the surface-to-volume ratio and tailor the hydrodynamic properties of an assembly. On the next step towards a 3D cell tissue, mouse fibroblast cells are cultivated in a petri-dish, which was partly covered with VFL-printed 20 μm sized spherical particles with 8 μm holes (Figure 3.6a). After four days of cultivation, laser scanning confocal microscopy micro-graphs show the interaction of cells and particles.

During cultivation, the cells spread on the surface of the well-plate and grew inside the areas where particles were located (Figure 3.6b). The cells show a manifold interaction with the particles, infiltrating the porous structures of the particles (Figure 3.6 I) and percolating and connecting various particles by the actin filament (Figure 3.6 II, III). This study confirms the biocompatibility of the particles and encourages study further the influence of particle shape, material, and surface roughness on cell-particle interaction.

3.3.4 Particle agglomeration and self-assembly

The any-shape particles reveal different agglomeration and self-assembly tendencies, which mainly depend on two aspects. The first most prominent aspect is the wettability of the particle material by the solvent. Dissolving the particles in a non-wetting aqueous solvent supports particle agglomeration by minimizing the wetted surface. A well-wetting solvent, such as isopropanol, encourages the dispersion of single particles. The hydraulic resistance studies unravel the second aspect of particle agglomeration. Particles with larger contact areas and more contact points increase the

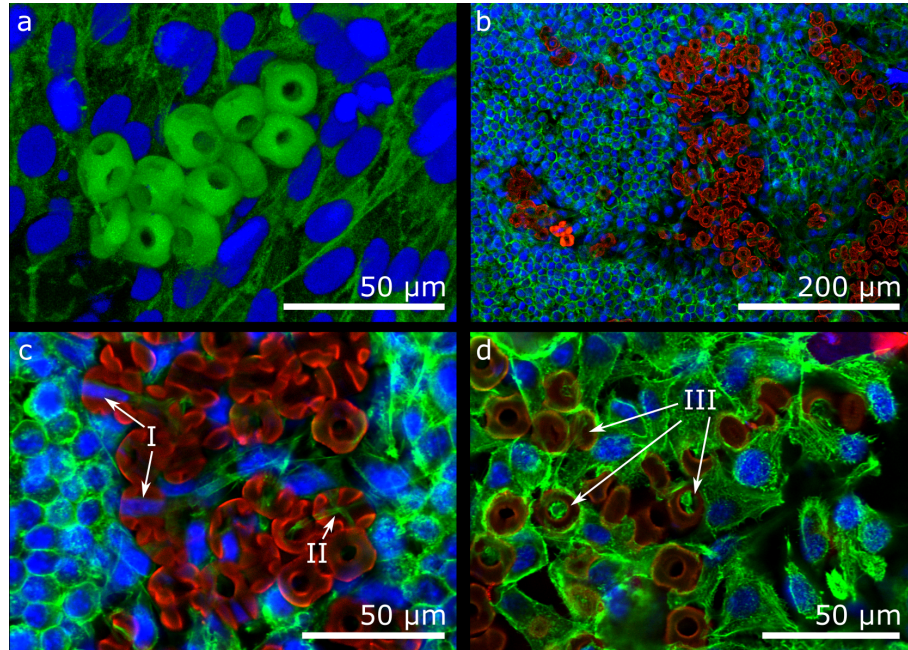


Figure 3.6: Confocal micrographs of VFL-fabricated 20 μm sized particles with 8 μm holes as cell culture tissue. A 3D visualization of the particles (green) in the cell-assembly is generated from a confocal z-stack image (a). Interactions of the cells and particles (red) are visualized as confocal micrograph in an overview (b) and in two detailed visualizations (c,d). (I) signs cell-infiltration into the porous particles, (II) shows actin filament percolating porous particles, and (III) displays actin filament attaching to the particle surface connecting the assembly.

inter-particle attractive forces and promote agglomeration. The assembly compression studies confirm these observations. Compressed assemblies with increased inter-particle contact area result in more robust agglomerations that do not disassemble in the executed ultrasonic treatment.

Particularly during the cell cultivation experiments, the particles agglomerate in the well plate assembling in certain regions, while other areas do not contain any particles (Figure 3.6b). This inhomogeneity results from the sample preparation process. After particle fabrication and purification, the isopropanol dissolved particles are pipetted into the wellplate, spreading evenly around the whole area of the well plate. After evaporation of the isopropanol, the cells are seeded with the aqueous cell-culture medium. The aqueous solvent acts as a non-wetting solvent and promotes particle mixing and agglomeration during the initial fluid flow. The few single particles remaining in the well plate stuck to the well plate without being re-dispersed by the aqueous cell culture medium. This example represents a macroscopic self assembly process of any-shape micro particles triggered by solvent exchange.

3.4 Conclusion

This study demonstrates an in-flow two-photon direct laser writing approach for the continuous high-throughput fabrication of microscopic 3D any-shape particles for tissue engineering applications. The printing process was successfully executed to fabricate 150 000 particles in 72 hours, proving continuous processability. The hydraulic permeation properties of printed particles were analyzed by filtrating particles with different amounts and shapes in microfluidic channels and measuring the hydraulic resistance by permeation. The unique microfluidic encapsulation method allows comparability of different particle amounts, materials, and shapes matching the filtrate flux equation. The particle shape defines the contact points of neighboring particles in an assembly and influences the hydraulic resistance significantly.

The study reveals that mechanistic filtrate models need to account for the

particle shape, the wettability of the solvent. The particle-particle interactions define the inter-particle adhesion and thereby strongly influences the packing density of a filter cake.

Additionally, the porous particle assembly can be applied as permeable scaffold for tissue engineering enabling nutrient supply through advective permeation. As a first step towards this application, mouse fibroblast cells were cultivated on the any shape particles and showed manifold interactions with the particle assemblies.

4 Filter cake motions in membrane cleaning procedures

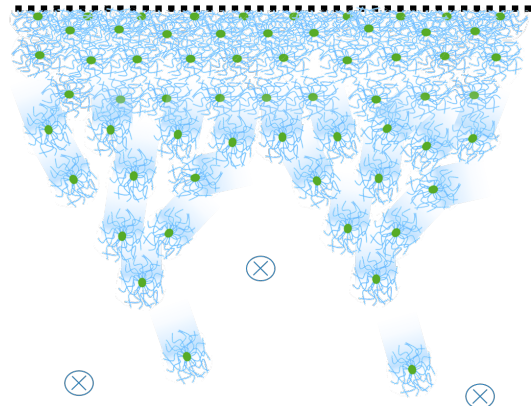
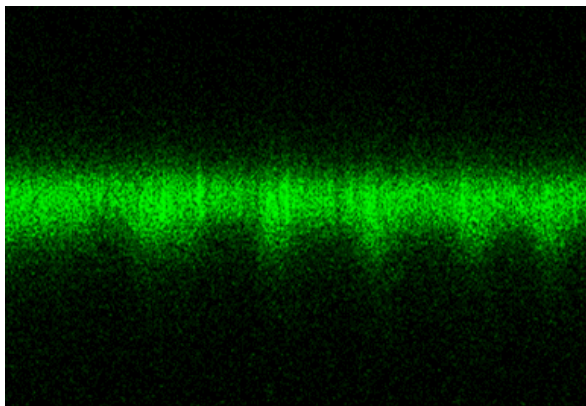
Parts of this chapter have been published as:

Arne Lüken, John Linkhorst, Robin Fröhlingsdorf, Laura Lippert, Dirk Rommel, Laura de Laporte, Matthias Wessling

Unravelling colloid filter cake motions in membrane cleaning procedures, Scientific Reports, 10, 2020

DOI: 10.1038/s41598-020-76970-x

4



4.1 Introduction

Membrane micro- and ultrafiltration is a well established low-energy unit operation for separating and concentrating particles and colloids in the fields of, e.g., food processing, water treatment, and biotechnology. In such filtration processes, a trans-membrane pressure (TMP) drives the fluid through the porous structure of the membrane while larger particles are retained by size exclusion. The retained matter accumulates on the surface of the membrane. This particle retention causes the generation of a cake layer, which yields an additional pressure loss on top of the membrane's own pressure loss and thus significantly impacts the process energy requirement. Therefore, depending on the application, cleaning methods such as cross-flow flushing with detergent solutions or backflushing from permeate to feed side are widely applied methods in industry [Bake2004]; [Raut2004]. Understanding the origin, behavior, and properties of such cake layers in filtration and cleaning processes is of crucial importance to improving current evidence-based filtration models [Bacc2011]; [van 2018]; [Send2016]; [Wei2011].

Compared to hard particle filtration, filtration of soft particles such as colloids or biological matter results in a compressible cake layer. This compression leads to internal mobility within the cake, which facilitates rearrangement of the particles, resulting in higher packing densities, and forms dense gel layers near the membrane surface [Hwan2001]. Accordingly, the particle material properties such as size, softness, charge, and ability to interpenetrate mainly influence the cake properties [Hwan2010]; [Lore2016]. Such properties can be tuned in a reproducible manner using colloidal microgels as a model. Microgels are soft polymeric colloids that are well-studied and easily tunable. Fabricated by precipitation polymerization, microgels offer diameters ranging from less than 100 nm [Xia2013] up to 5 μm [Ksia2020]. Microgels are tunable to respond to an external stimulus like temperature, pH, ionic strength, or pressure by changing their size or charge [Plam2017]. The properties of densely packed microgel suspensions cover deswelling, deformation, and interpenetration effects and nicely

mimics other soft matter applications [Senf1999]; [Bouh2017]; [Moha2017]. This flexibility and reproducibility makes the use of microgels in soft matter filtration studies advantageous [Link2016]; [Nir2016]; [Hend2010].

Characterization of filter cakes on membrane surfaces follows either visual or non-visual methods. Non-visual methods pose the challenge that calibration experiments need to characterize the origin of the measured value, and appropriate models are required to interpret the data. While hard-sphere filtration can be effectively monitored by TMP and flux measurement [Bake2004] or impedance spectroscopy [Bann2016]; [Ho2016]; [Mart2018] and modeled accurately [Zama2009]; [Loha2020], non-visual approaches for soft-matter filtration are limited by underlying models. Even though these models have increased in complexity and accuracy in recent years, further experimental verification is needed to cover multi-scale phenomena such as compression, deformation, and rearrangement of the filter cake [Jean1996]; [Berg2018b]; [Gnan2019]. The on-line visualization of such microscopic events of the filter cake needs adaption of the membrane modules. Hence, a popular method is to retain particles by microfluidic structures to study the phenomena in the cake layer. A glass slide represents one channel wall perpendicular to the membrane such that high-resolution imaging of the filter cake cross-section is possible [Ngen2010a]; [Bacc2011]; [Link2016]; [van 2018]. Studies, monitoring filtration with real membranes give additional insight into the membrane-cake interface [Wies2019], the cake morphology [Hugh2006], and cleaning efficiencies [Zato2009]. Nevertheless, high-resolution in-situ microscopy often suffers from insufficient process control resulting in pulsating flows or moving membranes as well as from large focal distances stemming from channel design, reducing the fluorescent signal.

Membrane filter cakes are known to show instabilities and pattern formation upon certain process parameters. The first time in 1984, Jonsson observed a stripe-shape pattern on a filter cake by recording the membrane surface during dextran and whey filtration [Jons1984]. Jonsson showed that the stripes occur in the concentrated boundary layer, which moves in flow direction and he identified that the stripe distance correlates inversely with

the cross flow velocity [Jons1984]; [Jons1986]. A few years later, Larsen explained and modeled this behavior in a 2D model of macromolecular solutions, transferring the observations of instabilities at phase boundaries with high viscosity gradients [Jose1984] to membrane filtration [Lars1991]. For certain permeation rates the viscosity-gradient driven instability at the filter cake boundary and bulk are stabilized and persist on the filter cake surface. Larsen developed a correlation for pattern stability using a modified permeate Reynolds number and the wave-number [Lars1991]. In 1993, Hendriksen et al. presented a 3D-FEM model of the striping phenomena and highlights the importance of a large viscosity gradient from bulk to cake layer for the occurrence of the stripe-pattern [Pete1993]. Recent studies recap the phenomenon experimentally for filtration of oil emulsions and prove that the pattern accelerates emulsion back-transport from cake to bulk [Tanu2017]; [Tanu2018]. However, in the context of membrane filtration, the striping-pattern was only visualized as a 2D-image in bird's eye view without any information about its depth and its mobility in the cake. Additionally, stripe-like surface patterns during membrane cleaning without filter cake permeation has not been reported before.

This study visualizes the motions of microgel filter cakes by confocal laser scanning microscopy. The $\sim 2 \mu\text{m}$ sized transparent soft microgels comprise a fluorescently labeled 200 nm core for imaging the center position. The microgels are filtered on top of a commercial polyethersulfone (PES) membrane with a pore size of 100 nm and the filter cake's top view and cross-section is in-situ visualized. The morphology as well as dynamic bulk motions of the filter cake during backflushing and cross-flow flushing are analyzed. Cross-flow flushing creates a longitudinal stripe-pattern on the cake surface, which is visualized in 3D and analyzed regarding its mobility at different depths at changing average cross-flow velocities. Additionally the study accounts for the stripe pattern's influence on cake removal kinetics.

4.2 Experimentals

Membrane module A custom membrane module was designed to enable membrane permeation and in-situ observation of the membrane surface (see Figure 4.1). The in-situ observation is implemented by attaching a glass cover slide as module bottom, such that the optical laser microscope can directly observe the membrane surface. Additionally, the feed channel height of 700 μm is adjusted by positioning the membrane with an imprinted spacer structure in the module lid. This spacer structure avoids movements of the membrane on the one hand and reduces the feed channel height which shortens the optical laser path and increases microscope resolution on the other hand. The module was liquid-tight tested for pressures up to 400 mbar and used in the experiments at pressures below 300 mbar.

The module was designed by Autodesk Inventor and fabricated by additive manufacturing with a polyjet printer (Objet Eden 260VS) using "Veroclear" material. The printed module was stored in 1M NaOH solution to dissolve the support material, rinsed with water and dried at room temperature for at least 24 h. Afterwards a 175 μm thick glass cover was glued to the module using a two-component epoxy glue "UHU-Plus Schnellfest" and baked at 60 °C for another 24 hours. The module was assembled with a 0.1 μm pore size PES membrane with an active membrane size of 15 mm x 24 mm (Pieper Filter GmbH). The membrane was mounted between two 0.5 mm thick flat gasket frames (Viton/FKM 0.5 mm, Lux & Co GmbH). The membranes were wetted beforehand by immersing them in a 50 vol% water, 50 vol% ethanol mixture for at least 24 h. The module top and bottom were pressed together using four plastic M4 screws and nuts. 3x2 mm polyurethane tubes were connected using M5x3 mm IQS connectors (Landefeld GmbH).

pNIPAM-co-AAc microgels Filtrated colloids are poly(N-isopropylacrylamide)-co-acrylic-acid core-shell microgels that were synthesized as described elsewhere [Wies2019]; [Go2014]. In short, the polystyrene cores have a diameter of 200 nm and are labeled with a Nile-red fluorescent

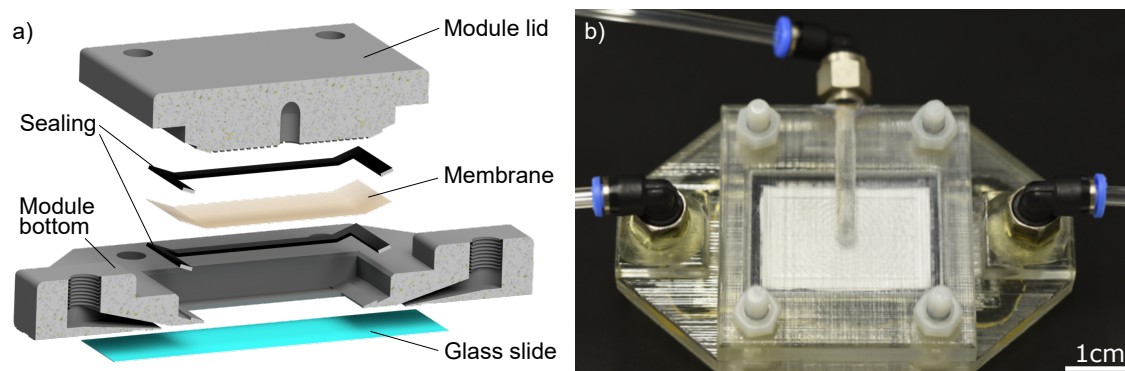


Figure 4.1: The cross-section model of the module assembly shows the additive manufactured filtration device consisting of a module bottom, a module lid, and the filtration membrane squeezed in between two flat sealing gaskets. The module lid includes a membrane positioning spacer structure and the permeate outlet. The module bottom includes an integrated glass slide, the feed inlet, and the retentate outlet (a). The permeate-side view of the real module shows the assembly with four plastic screws, IQS push-in fittings, and tubing (b).

4

marker, such that visual observation of the center of the microgel is possible using a fluorescent microscope. The non-fluorescent pNIPAM shell (14 g/l NIPAM, 1 wt% MBA, 5.8 wt% KPS, 26 mol% or 7 mol% AAc - see section Filtration experiments all percentages are relative to the monomer amount) is polymerized around the cores and creates a soft microgel with a diameter of $\sim 2 \mu\text{m}$ and has a negative charge with a zeta potential of -37 mV at pH 7 (measured with DLS - ZetaSizer Ultra). Both microgel batches (26 mol% and 7 mol% AAc) had the same size and Zeta-potential. The synthesis solution was purified from linear chains and residuals of other reactants by dialysis (25kDa, SpectraPor 6, CarlRoth) against DI water for one week while changing the DI-water twice a day resulting in pH7. For all experiments the microgel solution was diluted with water to a concentration of 0.1 g/l. The pH was kept constant at pH 7 during all experiments and checked before and after each experiment.

Experimental setup The experimental setup uses a feed side syringe pump (Chemyx Fusion 4000) for precise and pulseless flow and a digital backpressure regulator (Elveflow OB1 MK2+) on the retentate module outlet. Accordingly, experiments could be conducted either in constant

pressure cross-flow filtration by adjusting a feed flowrate with the syringe pump and setting a backpressure with the pressure regulator or in dead-end constant flux filtration by closing the retentate channel with a valve. The filtration module is mounted on an inverted confocal laser scanning microscope (Leica SP8) using 10x air and 63x air objectives, enabling on-line visualization of slices in the top view and the cross-section to the membrane with a frame rate of ~ 1 frame per second at a resolution of 512x512px. The cross-section images were taken by laser scanning in x-z scan mode. Thereby the laser scans in x-direction and the sample simultaneously moves through the focal plane by the galvo controlled z-stage.

Filtration experiments Experiments on cake stability and morphology (Figure 4.2) were conducted in constant pressure filtration mode by applying a backpressure of 100 mbar and an average cross-flow velocity of 4.2 cm/s. The low trans-membrane pressure of 100 mbar was chosen to reduce the influence of cake growth during the analysis. The average cross-flow velocity is calculated by dividing the feed volume flow by the size of the feed channel cross-section, which has a width of 15 mm and a height of 700 μm . For mobility studies, an 80x80 μm area of the cake was photo-bleached by applying maximum laser power for several minutes. For this experiment the first microgel batch with 26 mol% AAc was used.

Back-wash mechanisms (Figure 4.3) were studied by first creating a cake layer by constant pressure filtration at 300 mbar for a specific duration and subsequently applying a gentle gravitational permeate back pressure of ~ 10 mbar by hand lifting the permeate outlet tube and stopping the feed flow. The experiments were repeated twice showing the same phenomenon, only images from the one experiments with clearer imaging are shown. For this experiment the first microgel batch with 26 mol% AAc was used.

Pattern formation and its morphology at cross-flow flushing (Figure 4.4 & 4.5) were studied by first dead-end cake formation (3 minutes, 0.8 ml/min), then closing the permeate by a valve to avoid any membrane permeation or permeate backflush, and subsequent cross-flow flushing at different velocities without applying any retentate back-pressure. All experiments con-

ducted in the flow-range are plotted in the graph (Figure 4.4b,c). For this experiment the second microgel batch with 7 mol% AAc was used.

The experiments on pulsating flow (Figure 4.6) were conducted by connecting two independent channels of the digital pressure regulation (Elveflow OB1 MK2+) to the feed and retentate side. The experimental procedure starts with constant pressure cross-flow filtration at 300 mbar for 2 minutes to generate a filter cake and subsequently changes to a pulsating cross-flow by applying a sinusoidal pressure on the feed side ranging from 0-100 mbar while eliminating membrane permeation by closing the permeate side using a valve. This experiment uses the second microgel batch with 7 mol% AAc.

4

4.3 Results and Discussion

A custom filtration module with a build-in glass slide parallel to the membrane was fabricated by additive manufacturing and used in all filtration experiments. Poly(N-isopropylacrylamide)-co-acrylic-acid (pNIPAM-co-AAc) microgels were filtrated in two experiment sets by either constant pressure or constant flux filtration. The filter cake was simultaneously monitored by confocal microscopy. In order to monitor the membrane in situ, precise control of the membrane position was necessary. For this purpose, a permeate spacer structure positions the membrane surface 700 μm above the glass slide in all filtration states. For larger channel size, the fluorescent signal was found to weaken, and microscopical resolution suffered. All filtration experiments were conducted in laminar flow condition with a Reynolds number $2 < Re_{\text{Channel}} < 250$ for the channel and $0.004 < Re_{\text{Particle}} < 0.4$ for a particle with a diameter of 2 μm as characteristic length. Assuming the feed overflowing the particles with a diameter of 2 μm as characteristic length at the filter cake surface with an average cross-flow velocity of $\bar{u} > 0.1$ cm/s, the Peclet numbers are in the range of $Pe > 15000$, representing advection-dominated fluid transport.

4.3.1 Cake morphology during filtration

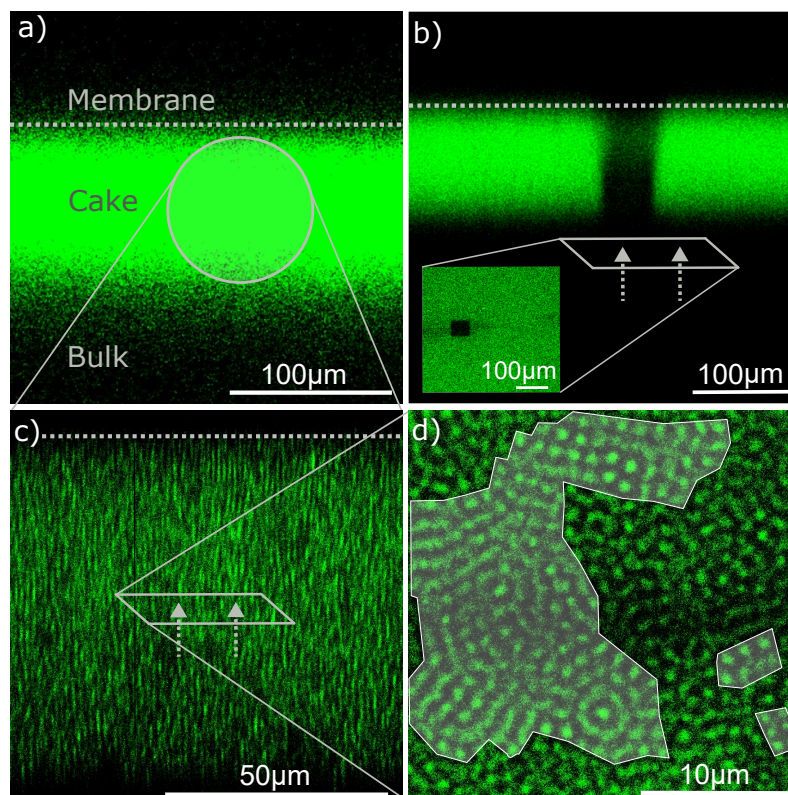


Figure 4.2: (a) On-line filter cake visualization by confocal microscopy in cross-flow constant pressure filtration with a labeled membrane, filter cake, and bulk. (b) Filter cake mobility experiment under cross-flow filtration. The image shows the persistent photo-bleached region (black stripe) in cross section and top view (square) not moving during cross-flow filtration. The membrane position is indicated with a grey dashed line. (c) Magnification of the cross-section with 63x lens enables identification of individual microgels. The membrane position is indicated with a grey dashed line. (d) A representative slice taken parallel to the membrane, demonstrating the morphology of the filter cake with highly ordered domains highlighted in grey.

Using the custom filtration module, a constant pressure cross-flow filtration is conducted using the labeled microgels (find details in the method section), which deposit as a thick cake layer on top of the membrane surface. Laser scanning confocal microscopy visualizes the top view (x-y-image) and the cross-section (x-z-stack) of the filter cake. A 10x objective helps to visualize the shape of the cross section of the filter cake. This method allows an efficient and fast study of the cake's general shape and its mobility on a large observation field of up to 400 μm . As shown in Figure

4.2a, cake growth with uniform cake thicknesses all over the membrane is identified. In the laminar flow regime with $Re < 100$, this uniformity is independent of the cross-flow velocity. The cross-flow independency confirms the observations made in traditional filtration experiments [Wies2018].

A photo-bleaching experiment enables analysis of the macro-mobility of the cake layer. For this purpose, a small area of the filter cake is illuminated with high laser intensity. Under these conditions, in this area, the microgels were still present, but the fluorescent signal disappeared (Figure 4.2b). The constant pressure cross-flow filtration with 100 mbar TMP and an average cross-flow velocity of 4.2 cm/s did not show any changes in the bleached region within an observation time of 5 minutes. Accordingly during filtration, no macro-mobility of the cake induced by the cross-flow was observable.

Single microgel behavior was analyzed by utilized a 63x air objective with long working distance to characterize both the cross-section (Figure 4.2c) and a representative slice parallel to the membrane inside the cake layer (Figure 4.2d). The cross-section shows the cores of the single microgels appearing as elongated stripes, as well known from 3D-image stacks in confocal microscopy using the z-stack technology. [Di2017]. The top-view slice is located in the center of the filter cake, i.e., approximately 10 levels of microgels are above and underneath the visualized slice. The image shows areas with highly ordered arrangements of microgels in parallel lines next to each other, indicating crystalline structures. The applied criterion for being highly ordered was a minimum of three microgels being located on a straight line and two of these lines being parallel to each other. These highly ordered areas are labeled in grey indicating half-ordered and half-amorphous regions. This existence of highly ordered areas confirms microfluidic observations of partly crystalline and partly amorphous cakes for jammed colloids [Link2019]; [Geno2011]. Based on experimental phase diagrams generated with pNIPAM microgels, this transition between amorphous and crystalline structures develops in the transition region from fluid to crystal behavior at effective volume fractions $\phi_{eff} \sim 0.56$ [Palo2013].

4.3.2 Cleaning by backflushing

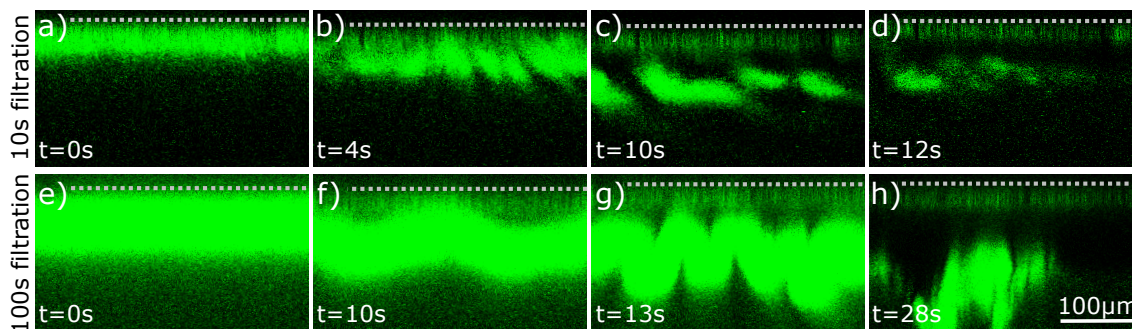


Figure 4.3: Filter cake backflush mechanism induced by a gentle back pressure of 10 mbar. The membrane position is indicated with the grey dashed line. (a-d) after 10 seconds of 300 mbar filtration, the cake detaches in fragmented pieces; (e-h) after 100 seconds of 300 mbar filtration, the cake detaches from the membrane in one piece. A monolayer of strongly adhering microgels remains on the membrane and is visible in (c,d,g,h). It appears larger due to diffraction of the light.

Additionally, this study analyzes the morphology of colloidal filter cakes while applying a backflush cleaning procedure. Two sets of experiments were conducted with 10s filtration and 100s filtration, both at 300 mbar constant pressure. After cake built up, the cake was removed by applying a gentle backflush while stopping all other flows. The backflush was induced by a 10 mbar trans membrane pressure on the permeate side, leading to two different phenomena. First, after 10 s of cake build-up, the cake layer detached in fragmented pieces from the membrane and subsequently dissolved in the bulk (Figure 4.3a-d, video available in the SI V1). Second, after 100 s of cake build-up, the whole cake layer detached in one piece, bent, and finally broke apart (Figure 4.3e-h, video available in the SI V2). At a subsequent cross-flow, hazy fragments were observed in the retentate outlet tube of the module, which subsequently disaggregated in the storage beaker. In both experiments, a shiny layer remains on the membrane surface. At higher magnification, this layer figures out to be a monolayer of microgels adhering to the membrane, appearing broader due to the light's diffraction at low magnification. The microgels touching the membrane surface deform strongly, such that the area of contact points and subsequently the attractive interaction potential (e.g., Van der Waals forces) increases strongly [Well2015]. Accordingly, the monolayer

is hardly removable even at high shear flow rates, as studied by Wiese et al. [Wies2019]. These backflushing results lead to the assumption that compression and more time for rearrangement in the filter cake stabilizes the cake structure by increasing the packing density and interpenetration degree. This phenomenon is in accordance with literature, where jamming of microgels has been found to induce entanglement of polymer arms and to increase the adherence to each other [Moha2017]. On top of this jamming phenomenon, studies have shown that highly concentrated suspensions tend to rearrange and form crystalline domains during waiting times [Mulu2011].

4.3.3 Cleaning by cross-flow flushing

An alternative way of removing the filter cake from a membrane is cross-flow flushing through the feed channel without membrane permeation. This cross-flow experiment was performed by first filtrating 2.4 ml of a 0.1 g/l microgel suspension in constant flux dead-end mode, ensuring the comparability of the cakes in different experiments. Subsequently, closing of the permeate channel, opening of the retentate channel, and applying a cross-flow stream on the feed side of the membrane induced a shear force on the filter cake surface. For slow cross-flow velocities the cake removal takes several minutes, for high velocities the cake removal only takes a few seconds. During cake removal a longitudinal stripe-pattern appears on the filter cake in a certain range of cross-flow velocities similar to the observations made for stripe-pattern during cross-flow filtration of other materials [Jons1984]; [Lars1991]; [Tanu2017]. The following sections describe selected properties of this stripe-pattern.

Stripe-pattern formation

The stripe-pattern has the shape of parallel regular ridges (Figure 4.4a) along the flow direction on the whole area of the filter cake covered membrane (Supplementary Figure S1). During one experiment, unintentionally trapped air bubbles confirmed that the ridges follow the streamlines. The

bubbles settled on the feed side of the membrane and the ridges followed the curvy shape around the bubbles, in accordance with the streamlines (Supplementary Figure S2). The ridges' appearance and their peak-to-peak distance were found to depend on the cross-flow velocity \bar{u} as shown in Figure 4.4. For cross-flow velocities higher and lower than the plotted range of $0.2 \text{ cm/s} < \bar{u} < 13 \text{ cm/s}$, no pattern appeared as illustrated in Figure 4.4a in the top and bottom images. At low cross-flow velocities in the range from $0.2 \text{ cm/s} < \bar{u} < 1.5 \text{ cm/s}$, a time lag of several minutes occurred before pattern formation was observed (Figure 4.4b). Additionally, in this flow range, the peak-to-peak distance at the moment of pattern appearance is larger (Figure 4.4c). The ridges stayed on the cake surface for the complete duration of cake removal. They slowly moved in wavy motions, with ridges merging and new ones appearing. The longer the process took, the more ridges merged, such that the peak-to-peak distance during cross-flow flushing increased until the filter cake was completely removed. The duration for complete cake removal after pattern appearance decreased with higher cross-flow velocity as expected (Figure 4.4b).

Cake mobility under shear stress

The cake mobility during pattern appearance was studied by a photobleaching experiment similar to the one in Figure 4.2. After dead-end cake formation, a specific region of the cake was exposed to high laser intensity, such that the microgels in this region were photo-bleached to the extent that they became non-fluorescent despite still being present (Figure 4.5a). When inducing the shear stress by cross-flow flushing at 2.4 cm/s without permeation, a fluorescent zone on the bulk side appeared in the bleached region at the very moment of pattern formation (Figure 4.5b). In the ongoing experiment the cake layer thickness decreased, but the fluorescent zone remained at the cake-bulk boundary until the complete removal of the cake layer (Figure 4.5c). Similar to the backflushing experiments, a monolayer remained on the membrane surface and did not show any movement in the photo-bleached region.

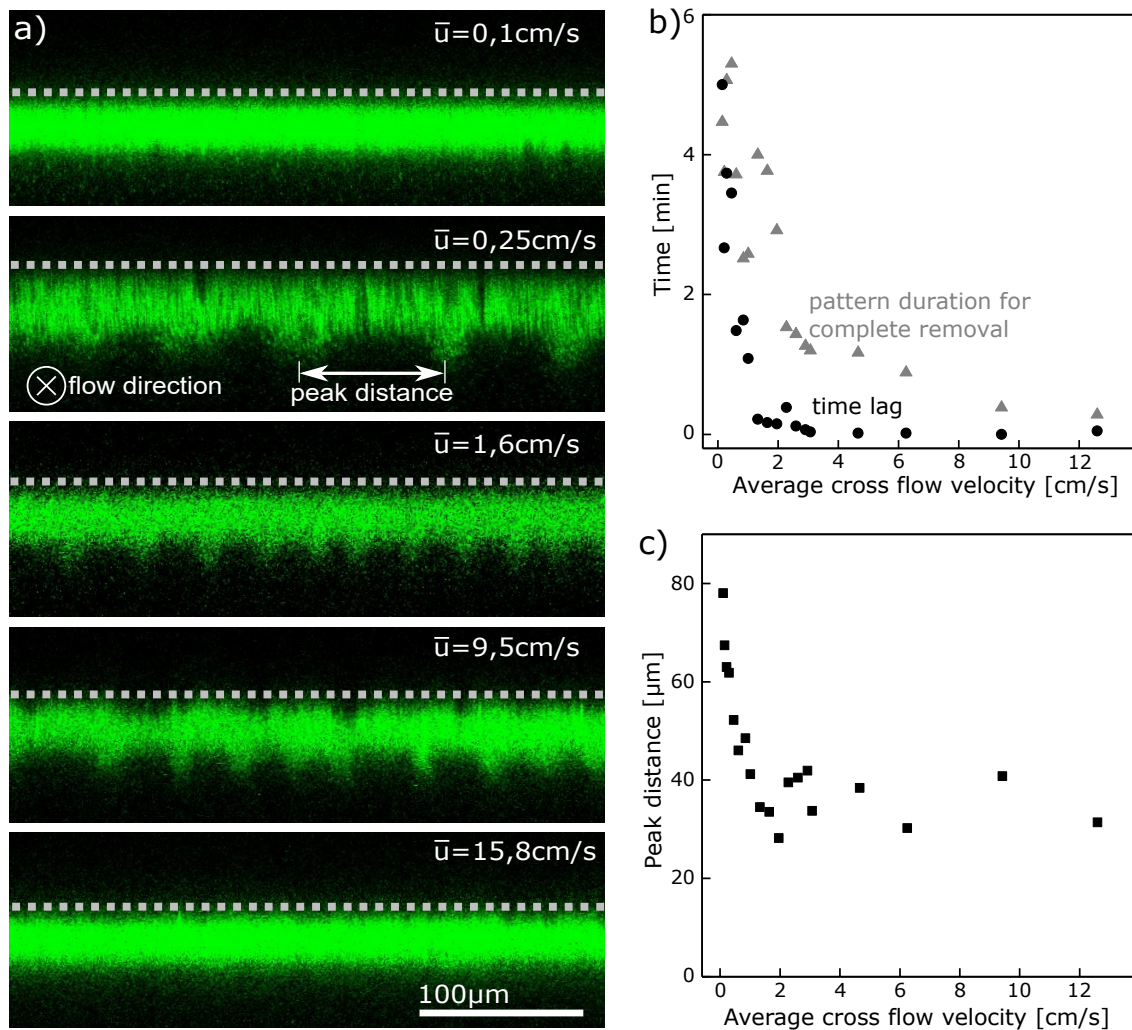


Figure 4.4: (a) Cake removal by cross-flow flushing without permeation reveals a pattern appearing on the microgel filter cake, which depends on the average cross-flow velocity \bar{u} . The cross-flow of the bulk is directed into the image-plane parallel to the pattern. The membrane position is indicated with a grey dashed line and the images are taken in the moment of pattern appearance after the time lag. (b) The pattern appears with a time lag after starting the cross-flow that depends on the cross-flow velocity (black). The cake removal time after first pattern appearance depends on the cross-flow velocity (grey). (c) The peak-to-peak distance in the first moment of pattern appearance depends on the cross-flow only for small velocities.

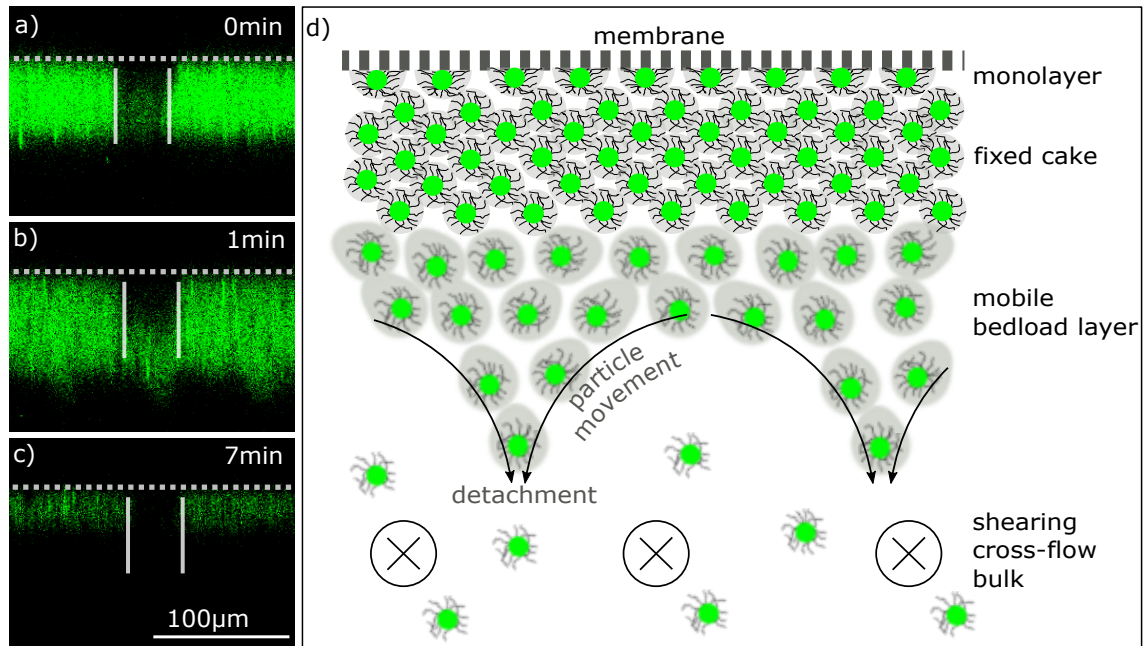


Figure 4.5: Cake mobility experiment with photo-bleached section. The membrane position is indicated with a grey dashed line. (a) After cake formation by dead-end filtration a 40 x 40 μm area of the cake is irradiated with high energy laser light to bleach the microgels. (b) Cross-flow flushing without permeation shows a mobility of the cake on the lower part of the surface after the surface pattern appears. (c) After complete cake removal, only a irreversible microgel monolayer remains on the membrane. The low resolution makes the single microgels shine fuzzily by diffraction, such that the light cone appears larger than the microgels are. (d) The schematic drawing shows the zones of the cake while inducing shear by cross-flow flushing of the bulk: An immobile monolayer on the membrane surface, a fixed cake-zone in the center, and the mobile cake with pattern formation on the bulk-side of the cake. The microgels move from the valley to the ridge, where detachment and dissolution is accelerated.

Pattern stability at pulsating flow and accelerated cake removal

The pattern stability was additionally studied in pulsating flows, such as it might appear with radial piston pumps or diaphragm pumps. First, a digital pressure regulator was connected to the feed side and cake built up was performed by constant pressure dead end filtration. Afterwards, the pressure regulator pump applied a pulsated cross-flow with an inlet pressure amplitude from 0-100 mbar with frequencies $f = 1 \text{ /s}$, 0.5 /s , 0.25 /s and 0.17 /s resulting each in the average cross-flow velocity of roughly 10 cm/s. Applying the frequency of $f = 1 \text{ /s}$ (Figure 4.6b), pattern formation occurred

just as in non-pulsating flow. For $f = 0.5$ /s (Figure 4.6c) pattern formation was decreased and for $f \leq 0.25$ /s no pattern formation was visible. For high frequencies, the soft tubing's and the module's damping compensation is dominant, such that pulsation does not inhibit the pattern. For small frequency the damping effect decreases, such that the process does not overcome the lag time that is needed to form a pattern.

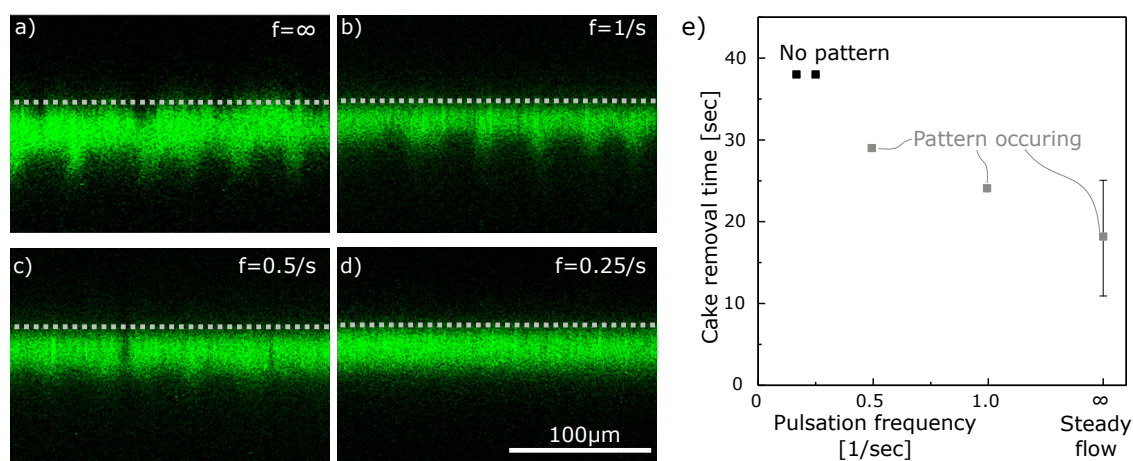


Figure 4.6: Slowly pulsating flow prevents pattern formation. All images are taken at average cross-flow velocities of $\bar{u} = 10$ cm/s and pulsation from 0-100 mbar. The membrane position is indicated with a grey dashed line. The pattern appears at no pulsation (a) or higher frequencies (b), but is reduced (c) or inhibited (d) at low frequencies. (e) For the equal average cross-flow velocity of $\bar{u} = 10$ cm/s the cake removal time increases on the pulsation frequency, while the fastest removal occurs in steady flow. The steady flow error is based on two independent experiments.

The cake removal kinetics of the pulsation experiments show another characteristic of the pattern (Figure 4.6e). The steady flow and the high-frequency pulsations with pattern occurrence show a faster cake removal than the slow pulsation frequencies below 0.25 /s, where no pattern occurs. Even though this is a limited data-set of six experiments, which does not demonstrate statistical significance, all conducted experiments support the trend. This accelerated dissolution is likely due to the increased microgel mobility in the cake surface, where the stripe-pattern occurs. On the one hand, mobility increases the microgels' distance to each other and hence reduces the inner cake adhesion. On the other hand, the microgels on the tip of the ridge have a larger contact surface to the bulk and experience

a higher shear force resulting in detachment. As shown in the scheme of Figure 4.5d, particle flow of microgels from the valley to the ridge and subsequent detachment is a possible sequence of the accelerated transport.

Discussion of the cake pattern

The observations of the stripe-pattern presented in this study show great similarity to the observations made for cross-flow ultra-filtration [Jons1984]; [Lars1991]; [Tanu2017]. For a similar range of cross-flow velocities 8 cm/s as used by Jonsson [Jons1986], the stripe-pattern occurs. Just as reported by Jonsson, this study observes a lack time before the pattern starts to develop [Jons1984]. Jonsson also reported a movement of the boundary layer into flow direction [Jons1986]. By visualizing the cross section of the cake layer this study is additionally able to resolve the size of the moving boundary layer and show that a fixed boundary layer remains close to the membrane. Finally, the here presented observation of an increased cake removal kinetic by the stripe-pattern was also reported for oil emulsion filtration in recent studies by Tanudjaja et al. [Tanu2017]; [Tanu2018]. The results on pulsated flow proves Tanudjaja's observation of reduced cake-layer formation for processes operated in the range, where the stripe-pattern occurs.

However, the here presented stripe-pattern only forms in operation modes without cake permeation. The models of Larsen and Hendriksen [Lars1991]; [Pete1993] both account a permeation flow through the membrane, transporting the particles hydrodynamically towards the membrane and maintaining a force equilibrium. In our process the permeation drag on the particles need to be substituted by a different force towards the filter cake. During permeation, the microgels are compressed by the permeating flux and adhere to each other by the entanglement of polymer chains [Moha2017], hydrogen bonds between NIPAM- and acrylic acid moieties [Meng2007], and hydrophobic interactions between the microgels [Krüg2018]. When permeation through the cake disappears and shear stress along the flow direction becomes dominant, the microgels on the cake's surface are ripped

out of their immobile cake position, and start flowing parallel to the bulk in a bedload layer with an significantly increased concentration compared to the bulk. Such concentrated bedload layers represent tightly packed assemblies of microgels with increased fluid viscosity, behaving similar to concentrated solutions of solid particles [Senf1999]. Accordingly, the bedload layer of flowing microgels represents a sheared boundary layer with major viscosity-gradient, which is known to create stripe like instabilities [Jose1984]. Unfortunately, a model for the process, similar to Larsen [Lars1991] or Hendriksen [Pete1993], would require absolute values of microgel interaction forces upon compression and data on the microgel concentration in the bedload boundary layer.

4

4.4 Conclusion and Outlook

This study links general particle specific investigations of densely packed soft colloidal suspensions observed in idealized microfluidic systems to real membrane processes. In this context, this study present a unique visualization of colloidal filter cakes during different process conditions in a cross-flow microfiltration module. As an exemplary colloid, pNIPAM-co-AAc microgels with a small fluorescent core were filtered. Accordingly, the filter cake is transparent, while the core positions in the whole cake can be detected precisely using confocal microscopy. In-situ measurements of the cake morphology on a single colloid level reveal highly ordered and amorphous regions inside the cake. Based on these results, further research is required for a better understanding under which circumstances crystalline and amorphous regions develop in filter cakes and how they develop during filtration processes. Furthermore, this study analyzes the motions of the filter cake when being removed by backflushing. The experiments reveal that the thickness of the filter cake and it's internal organization influence the stability of the cake, such that the size of the removed cake-pieces varies. Additionally, the cake structure and morphology changes when applying a shear force induced by cross-flow flushing along the cake without permeating the cake. The top-most particle layers of the cake mobilize and a pattern

on the cake surface appears. This pattern occurs with a time lag and has a characteristic peak-to-peak distance, both depending on the cross-flow velocity. The pattern supports colloid transport from cake to bulk and accelerates cake removal accordingly. The physical phenomena behind the pattern are instabilities on sheared boundary layers with major viscosity-gradients, such as the concentrated highly viscous filter cake and the low viscous bulk solution.

The phenomena of dynamic cake mobility presented in this study introduce a new approach of fouling analysis to the field of membrane filtration. This study shows that soft compressed cakes adapt their properties to their environment during permeation and shear force by changing their organization and mobility. Nowadays, such dynamic processes are barely studied and practically not considered in module design and process engineering but might give some additional guidance towards process optimization and additionally increasing accuracy of filtration models.

5 An automated lab scale filtration system for microgel purification

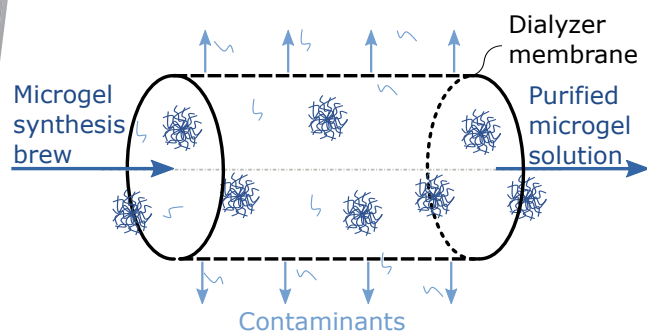
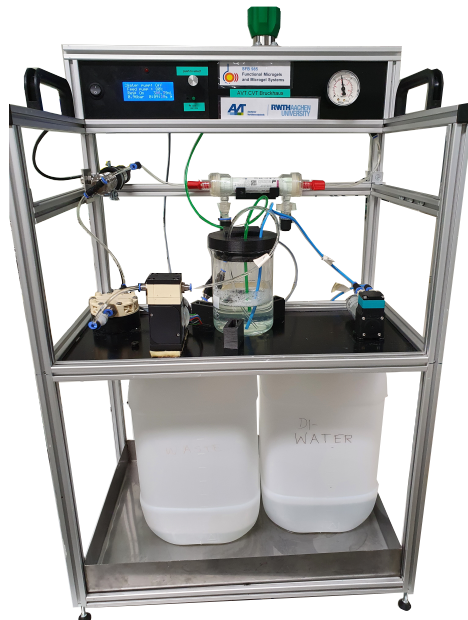
Parts of this chapter have been published as:

Arne Lüken, Maike Bruckhaus, Udo Kosfeld, Meike Emondts, Matthias Wessling

Automated tangential-flow diafiltration device, HardwareX, 2021, 10, e00200.

DOI: 10.1016/j.ohx.2021.e00200

5



5.1 Introduction

5

Ultrafiltration membranes are porous filters used to separate and concentrate particles in liquid suspensions by flushing them through the porous structure. The solvent and smaller molecules permeate the membrane while larger particles are retained by size and charge exclusion and accumulate on the feed side of the membrane. In tangential flow filtration (TFF), the feed suspension is tangentially flushed across the membrane. The solvent and smaller molecules permeate the porous membrane, while the small pores retain larger particles. These larger particles are concentrated and leave the membrane separately in the retentate. Accordingly, TFF systems are either used to separate larger particles, such as colloids, proteins, or cells from smaller ones, or to exchange the suspension buffer. The separation task's driving force is the transmembrane pressure from the feed to permeate side, which regulates the share of fluid permeating the membrane [Bake2004]; [Raut2004]. Therefore, TFF systems separate suspensions based on mechanical forces without chemical interaction. Thus, TFF is attractive for fragile and delicate purification tasks in the fields of pharmacy [Musu2018] and protein chemistry [Saxe2009], as well as for large-scale purification in bioprocessing [Cars2012] or water treatment [Wint2005].

Microgels are soft polymeric colloids that gained major attention in research in the last decade with possible applications in drug delivery and surface functionalization [Plam2017]. In lab-scale, microgels from various polymers are synthesized by precipitation polymerization in a batch or plug flow reactor [Wolf2018]. Both methods are easily up scaleable and suitable for large scale production. However, the synthesis brew contains linear pre-polymers, surfactants, and other residuals that need to be removed in a purification step. In lab-scale, purification is performed either by dialysis using bath dialysis tubes or ultracentrifugation [Tadr2011]. Both purification methods take a long time, extensive manual work, and are not suitable for a larger production. Tangential flow ultrafiltration is expected to be the promising purification procedure for upscaling microgel fabrica-

tion [Plam2017]; [Thor2011]. Microgel filtration was already experimentally studied in terms of its fouling characteristics [Wies2018]; [Nir2016] and its filter-cake motions [Lüke2020], as well as modeled by the group of Nägele [Roa2015]; [Park2020]. However, purification of microgels using membrane based TFF-systems was not studied in terms of its functionality and productivity.

TFF unit operation systems consist of a sample beaker, a permeate beaker, a feed pump, a membrane module, and a back pressure valve. The feed pump transports the sample inside the membrane module and creates a transmembrane pressure. The membrane-permeating share of the fluid flows into the permeate beaker. The remaining retentate is pressure released by the back-pressure valve and circulates back into the sample beaker. Accordingly, the sample loses volume and concentrates. In diafiltration, this sample volume loss is substituted by the new buffer. Systems without automatic process control are commercially available from different manufacturers for 4000 - 8000 €. Automated systems monitor pressures and flowrates using pressure sensors and balances to control the transmembrane pressure and to exchange buffer for diafiltration automatically. Simple automated systems cost around 20000 - 30000 € and can also be expanded with various sensors to monitor the filtration process. Exemplary manufacturers for such lab scale systems are Merck Millipore, Pall Corporation, Repligen Corporation, or Sartorius AG.

The core part of the TFF process is the membrane module. The membrane defines the separation task by selectively retaining certain particles or molecules by size or charge exclusion. The retained matter concentrates on the feed side and accumulates on the surface and in the membrane's inner pore structure in a filter cake. After filtration, cleaning procedures are applied to remove the accumulated matter and increase performance. Nevertheless, a share of the matter generally remains inside the pore structure. Subsequently, if contamination is not acceptable, membranes can be reused for the same product but need to be exchanged for different ones. TFF membranes and modules are subject to plenty of patents about membrane materials, flow-management, and module design continuously being

filed until today [Tana1982]; [Diel2005]; [Mart2013]; [Leut2019]. Consequently, each manufacturer offers slightly different membranes and modules. The two widespread membrane materials are polyethersulfone (PES) and regenerated cellulose (RC). The membrane modules are either stacked flat-sheet membranes or bundles of hollow fibers. Both materials are available in all kind of pore sizes for ultrafiltration and microfiltration applications. Depending on the effective membrane area, ready to use lab scale membrane modules are commercially available for prices of 100-700 €. This price is reasonable if reused for a specific product but rarely affordable if used as a single-use product in lab-scale purification tasks as in research and development, such as for microgel purification.

A more prominent application for PES membranes is blood purification by hemodialysis. This membrane application uses hollow fiber PES membranes to purify human blood on kidney failure diseases [Ronc2003] with worldwide more than 2 million patients receiving the treatment several times a week [Cous2011]. Blood purification modules are single-use and commercially available as hollow fiber module with different effective membrane areas reaching from 0.2 m² to 2.5 m². Additionally, these modules are available with different molecular weight cut-offs in the range of 10-300 kDa [Bosc2013]. Due to efficient mass production, the costs for one module is 20 - 60 €. These low cost membrane modules were recently applied for single pass tangential flow filtration for antibody purification and proved to be well suited for ultrafiltration applications [Yehl2020].

This work engineers an automated tangential-flow ultrafiltration device customized for fast and cheap diafiltration-based microgel purification. It presents the components of the filtration device to enable simple and fast reverse engineering. Additionally, this work analyzes TFF as a unit operation for microgel purification in terms of its ability to remove contaminants of different sizes applying nuclear magnetic resonance (NMR), bubble pressure tensiometry, and conductivity measurements.

5.2 Hardware description

The design of the device combines a robust filtration unit with low-cost automation for diafiltration. The process (Figure 5.1) uses diaphragm pumps with solvent-resistant PVDF/ETFE pump head for the feed pump (KNF-NF1.100) and a PP/ETFE pump head for the water pump (KNF-NF1.60). These pumps have moderate shear stress, a low risk of leakage, and can generate high pressures up to 6 bar. Simultaneously, they cost significantly less than comparable peristaltic pumps, which are often used in commercial TFF systems. For smooth filtration and pressure readout, a pulsation damper is added to the feed stream (KNF-Pulsationsdämpfer FDP 1.10). The filtration unit also includes a stainless steel diaphragm based back-pressure valve (Swagelok) on the retentate side of the membrane, which enables a robust and precise regulation of the transmembrane pressure in the range of 0 - 1.7 bar.

The core part of the filtration device is the membrane module that is commercially used as a medical blood dialyzer. The here presented 200 ml - 500 ml batch microgel application uses membrane modules with an effective membrane area of 0.2 m² and 0.6 m² and high-flux membranes (Baxter) with a molecule weight cut off (MWCO) of 30 kDa [Ronc2003]. One module costs approx. 50 € which is approx. 10 % of a comparable commercial TFF membrane module. The membranes used for hemodialysis and TFF are fabricated with the same polymer in a similar process. The reason for the significant price difference is the mass production of the hemodialysis membranes and modules. Compared to traditional microgel purification using batch dialysis tubes, the price of the single-use tubes is similar to the cost of the membrane modules used in this process.

These mechanical fluid-contacting components are all connected using 4 mm outer diameter polyurethane tubing. These components results in a feed-retentate cycle hold-up volume excluding the membrane module of 43 ml, while the membrane module adds another 17 ml or 52 ml for the Polyflux 2H or 6H respectively. Estimating an average transmembrane pressure of 0.4 bar, the feed pump can operate flow rates in the range of

0 - 1100 ml/min. The exemplary filtration with a Polyflux 6H membrane module achieves permeate fluxes at 0.4 bar of 175 ml/min.

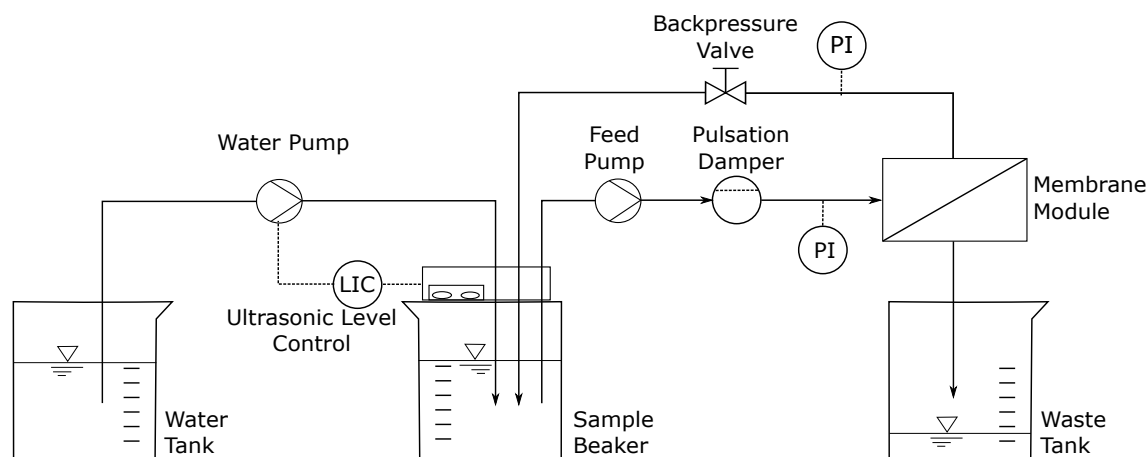


Figure 5.1: Piping and instrument drawing of the filtration process.

An Arduino microcontroller controls the electrical system (Figure 5.2). It communicates with the operator via two buttons and a display to initialize the operation mode and the settings. The microcontroller displays the feed pressure from the electric pressure sensor, the sample beaker volume, and the operation time during operation. The feed pump control and the di-filtration settings are set by the operator using the control buttons. The diafiltration is controlled using a low-cost contactless ultrasonic level indicator installed in the 3D-printed lid of the feed beaker. In running operation, the solvent permeates the membranes, so that the microgel concentration increases and the sample volume reduces. The ultrasonic level indicator measures this volume change in the sample beaker. It regulates it by controlling the water pump in iterative steps substituting the solvent with pure water from the water tank. Three safety measures are installed. The whole system is stopped automatically if one of the three cases occurs. In the first case, the float switch indicates that the waste tank is full. In the second, the electric pressure sensor exceeds a maximum pressure, and in the third, the water level in the sample beaker does not rise during water pump operation. This last case indicates a leakage somewhere in the system. The material costs for the automation are about 70 € for the microcontroller and circuit board and 5 € for the ultrasonic sensor. The electric pressure

sensor (327 €) and the float switch (3 €) in the waste tank are integrated as emergency sensors but are not essential for the system's operation.

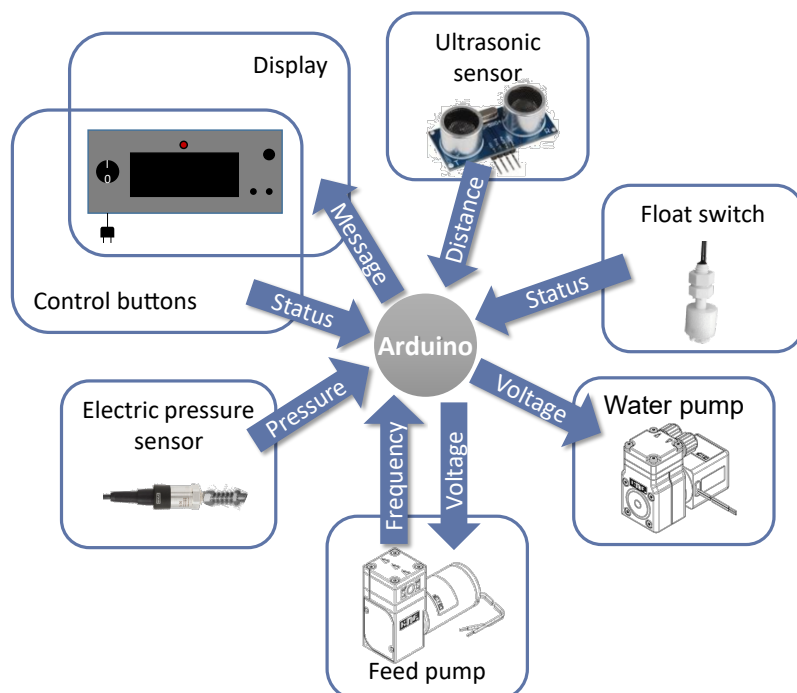


Figure 5.2: Electrical components communicating via the Arduino microcontroller.

With a total material price of 2400 €, the device is a low-cost alternative for cross-flow diafiltration applications and simplifies daily lab routine by automation. The reduced costs for investment and consumables allow technology usage, especially in academic research, with the necessity for high flexibility and limited budget. **Possible other applications** of interest are colloid and polymer purification, biochemical protein purification, or microbiological buffer exchange in biotechnological applications.

- *Colloid and polymer purification*: The device separates the product from synthesis residuals such as monomers, linear pre-polymers or low molecular weight side products in the same efficiency as traditional dialysis. It holds the advantage of being faster with less manual work.
- *Biochemical protein purification*: Membrane filtration is a mild mechanical purification step and is therefore well suitable for protein purification. Depending on the synthesis volume, the filtration device can

easily be adapted by changing the membrane module and the sample beaker.

- *Microbiological buffer exchange in biotechnology*: Such as in protein purification, buffer exchange for cells and bacteria also require mild conditions. Therefore, diafiltration with low transmembrane pressure is ideally suited for buffer exchange. The diaphragm feed pump installed in the device can be regulated to small flow rates to reduce shear stress.

5.3 Design files summary

5.3.1 Mechanical components

The filtration device is assembled on an aluminum profile cage (ITEM GmbH, profile5 20x20cm) where all devices and different customized component holder are attached (see Figure 5.3 or Filtration_device_assembly.stp). The 3D-printed *electric housing* consists of two parts containing the electrical components, including the circuit board with the Arduino microcontroller, the display, and the control buttons. The *valve holder* is a bent 2 mm steel sheet as holder for the *backpressure valve*. The valve must be assembled upright to ensure stable operation by eliminating bubble deposition inside the valve (see Figure 5.3). The *plate top* is a PVC sheet that is holding the analog pressure indicator. The *membrane module holder* is a 3D-printed tray for holding the membrane module in operation. The sample beaker is covered with a *beaker lid* that simultaneously holds the ultrasonic sensor and the three tube connections for feed, retentate, and water. The ultrasonic sensor is additionally covered with the *beaker lid cover* as splash protection. The beaker is fixated using three 3D-printed *beaker fixations* each consisting of a top and bottom part. A screw connects both parts, while the bottom part holds and fixates a screw nut, and the top is movable, enabling adjustments to the beaker diameter. The *ground* is a PVC plate where the *beaker fixations*, the pumps and the damper are positioned (see Figure 5.3). The bottom *tub* is made of 1 mm steel sheet and serves as a

Table 5.1: Design file table listing all self built design files including 3D-printed parts, technical drawings of metal parts, PCB files, PCB drawings and the Arduino software . All files are located in the online repository. 3D-printed components are named by their fabrication technology: fused filament fabrication (FFF) or polyjet 3D-printing (Polyjet)

Design file name	File type	Open source license
Filtration_device_assembly.stp	STP CAD file	CC BY-SA 4.0
FFF_Electric_housing.ipt	Autodesk Inventor CAD file	CC BY-SA 4.0
FFF_Electric_housing_cover.stl	STL	CC BY-SA 4.0
FFF_Electric_housing_holder.stl	STL	CC BY-SA 4.0
FFF_Beaker_lid_cover.ipt	Autodesk Inventor CAD file	CC BY-SA 4.0
FFF_Beaker_lid_cover.stl	STL	CC BY-SA 4.0
FFF_Beaker_lid.ipt	Autodesk Inventor CAD file	CC BY-SA 4.0
FFF_Beaker_lid.stl	STL	CC BY-SA 4.0
FFF_Beaker_fixation_top.ipt	Autodesk Inventor CAD file	CC BY-SA 4.0
FFF_Beaker_fixation_top.stl	STL	CC BY-SA 4.0
FFF_Beaker_fixation_bottom.ipt	Autodesk Inventor CAD file	CC BY-SA 4.0
FFF_Beaker_fixation_bottom.stl	STL	CC BY-SA 4.0
FFF_Membrane_module_holder.ipt	Autodesk Inventor CAD file	CC BY-SA 4.0
FFF_Membrane_module_holder.stl	STL	CC BY-SA 4.0
Polyjet_Membrane_connection.ipt	Autodesk Inventor CAD file	CC BY-SA 4.0
Polyjet_Membrane_connection.stl	STL	CC BY-SA 4.0
Workshop_Tub.ipt	Autodesk Inventor CAD file	CC BY-SA 4.0
Workshop_Tub.pdf	PDF technical drawing	CC BY-SA 4.0
Workshop_Valve_holder.ipt	Autodesk Inventor CAD file	CC BY-SA 4.0
Workshop_Valve_holder.pdf	PDF technical drawing	CC BY-SA 4.0
Workshop_Plate_top.ipt	Autodesk Inventor CAD file	CC BY-SA 4.0
Workshop_Plate_top.pdf	PDF technical drawing	CC BY-SA 4.0
Workshop_Pressuresensor_holder.ipt	Autodesk Inventor CAD file	CC BY-SA 4.0
Workshop_Pressuresensor_holder.pdf	PDF technical drawing	CC BY-SA 4.0
Workshop_Ground.ipt	Autodesk Inventor CAD file	CC BY-SA 4.0
Workshop_Ground.pdf	PDF technical drawing	CC BY-SA 4.0
PCB_code.brd	EAGLE Circuit Board File	CC BY-SA 4.0
PCB_code.sch	EAGLE Schematics File	CC BY-SA 4.0
PCB1.jpg	JPG	CC BY-SA 4.0
PCB2.png	PNG	CC BY-SA 4.0
FiltrationDevice.ino	INO arduino file	CC BY-SA 4.0

plate for the water- and waste tank and additionally as spill collection. The *tub* can be pulled out to the front to facilitate the tank exchange. The final mechanical component is the **membrane connection**. This component is not directly built in the device but used as a connector for directly linking the feed and retentate tube to replace the membrane module in the flushing step. See operation instructions (section 5.6) for a detailed description.

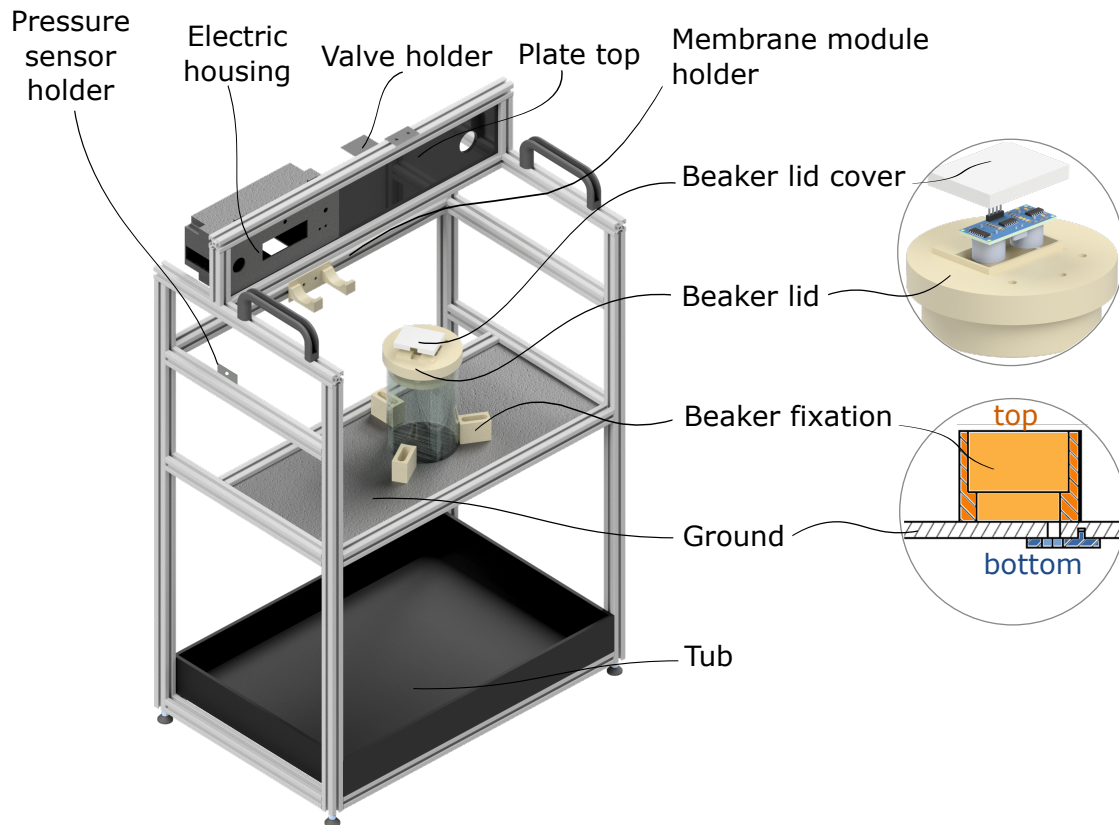


Figure 5.3: Rendering of the aluminum cage including all CAD design file items.

5.3.2 Electrical components

The electronic control system of the device is based on an Arduino Nano controller (Figure 5.4). It is operated with two buttons and one rotary push encoder and displays one 20x4 LCD display and one LED. The components connected to the controller are two pumps, one ultrasonic sensor, one electric pressure sensor, one float switch and one buzzer (see Figure 5.2). The electrical circuit (Figure 5.4) is supplied with a 24 Volt plug in power supply

preventing any high voltage in the system. A step-down converter supplies the Arduino and the operational amplifier.

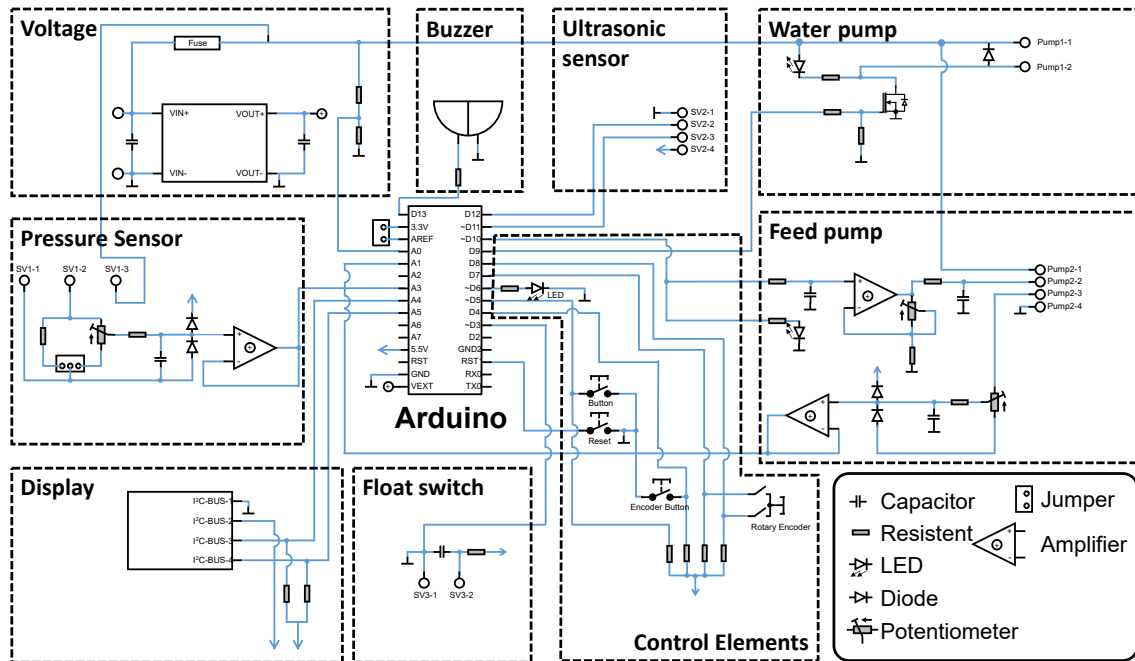


Figure 5.4: Electric circuit diagram

The signal of the **pressure sensor** is connected to the A3-pin of the Arduino (0 - 3.3 V) using a trimmer. The electric pressure sensor signal in the range of 4 - 20 mA is transferred to the 10-bit Arduino working range of 0 - 3.3 V, which results at a maximum pressure 2.5 bar in 930 steps with a minimum increment of 2.7 mbar. A 2-cable pressure sensor is connected, but the circuit board also allows using a 3-cable sensor with output signals of 0 - 10 V or 0 - 20 mA. A second equivalent optional sensor input is added to Pin A2, which is not shown in Figure 5.4, but can be found on the complete PCB in the online repository.

The **water pump** can be turned on and off by the D9 pin, and an onboard LED shows its operation. The **feed pump** is regulated by the Arduino D10 pin, so that its pump volume rate can be controlled. Therefore the signal is transferred in an impedance converter with adjustable gain to the pump control voltage of 5 V. Additionally, the rotation speed is back-transferred to the Arduino A1 pin but not used in our software. Similar to the water pump, an onboard LED shines when the pump is running.

The **ultrasonic sensor** gives the distance from the sensor to the liquid surface in the sample beaker. Using the maximum distance of an empty beaker from calibration, the sample volume is calculated. The **display** is connected via an I2C bus, the **float switch** and the **buzzer** are connected to the Arduino.

5.3.3 Arduino nano software

The software for running the device is available for an Arduino Nano microcontroller and has four cases that represent the main menu, the settings menu, the operation menu, and the error case. By choosing one of the menus the software is stepping into the respective control mode. Find a detailed description of the GUI and the software in section 5.6. The software code is available in the online repository.

5

5.4 Bill of materials

The Bill of materials in Table 5.2 only shows a reduced list, including the main components and collections of the smaller components. A complete bill can be found in the online repository. The primary device costs result from the pumps, the back-pressure valve, and the electric pressure sensor.

Table 5.2: Reduced *bill of materials* including the main components and collections of the smaller components. The detailed list of all single components is available in the entire bill of materials in the online repository.

Designator	Component	Number	Cost/EUR
KNF NF 1.100 IP30 24V Feed pump	Feed pump	1	577
KNF NF 1.60 KPDC water pump	water pump	1	215
KNF FPD 1.10 TTZ D1.6	Feed pulsation damper	1	183
Pressure transmitter WIKA S20 2.5bar	Electric pressure sensor	1	481
Manometer WIKA Typ 111.12 1.6bar	Analog pressure transmitter	1	10
Swagelok Valve KPR1DFC412A20000	Backpressure valve	1	440
Float Switch	Waste tank float switch	1	11
Ultrasonic sensor	Ultrasonic sensor for level indic.	1	5
Glas beaker 600ml d=90mm	Sample beaker	1	12
Vibration damper	Damper for pumps	16	1
PE Container 5l	Waste & water container	2	9
Membrane connection (polyjet)	Polyjet_Membrane_connection	1	10
3D-printed parts FFF	collection (see detailed table)	1	14
Polyflux dialyzer	Membrane module	1	50
Collections:			
ITEM aluminium profiles	Aluminum cage housing	1	172
Tubes, connectors	see detailed table	1	100
Electrical circuit components	Electric circuit and microcontroller	1	70
PVC Plates	Ground plate, Top plate	1	7
Steel Plates	Valve holder, Pressuresensor holder, Tub	1	< 1

5.5 Build instructions

5.5.1 Electrical control system

For building the electrical control system of the filtration device, you first need to order the circuit board and attach all electrical components to the board (see Figure 5.4 and the design files of the PCB - PCB_code.brd / PCB_code.sch / PCB1 / PCB2). The circuit board is screwed to the 3D-printed electric housing. The two buttons, the rotary push encoder, the LCD display, and the LED are directly connected to the electric housing's respective openings and later assembled to the aluminum cage in one piece.

5.5.2 Mechanical device fabrication

The mechanical part of the filtration device is assembled as a tabletop device with all components connected to an aluminum cage. The aluminum cage is fabricated by first cutting the 3m long aluminum profiles (Company: ITEM) to six different lengths (x, y, z, TopX, TopY, TopZ) and assembled

as shown in Figure 5.5. During assembly the *ground* plate and the *plate top* need to be inserted directly into the furrow of the aluminum profile as shown in Figure 5.3.

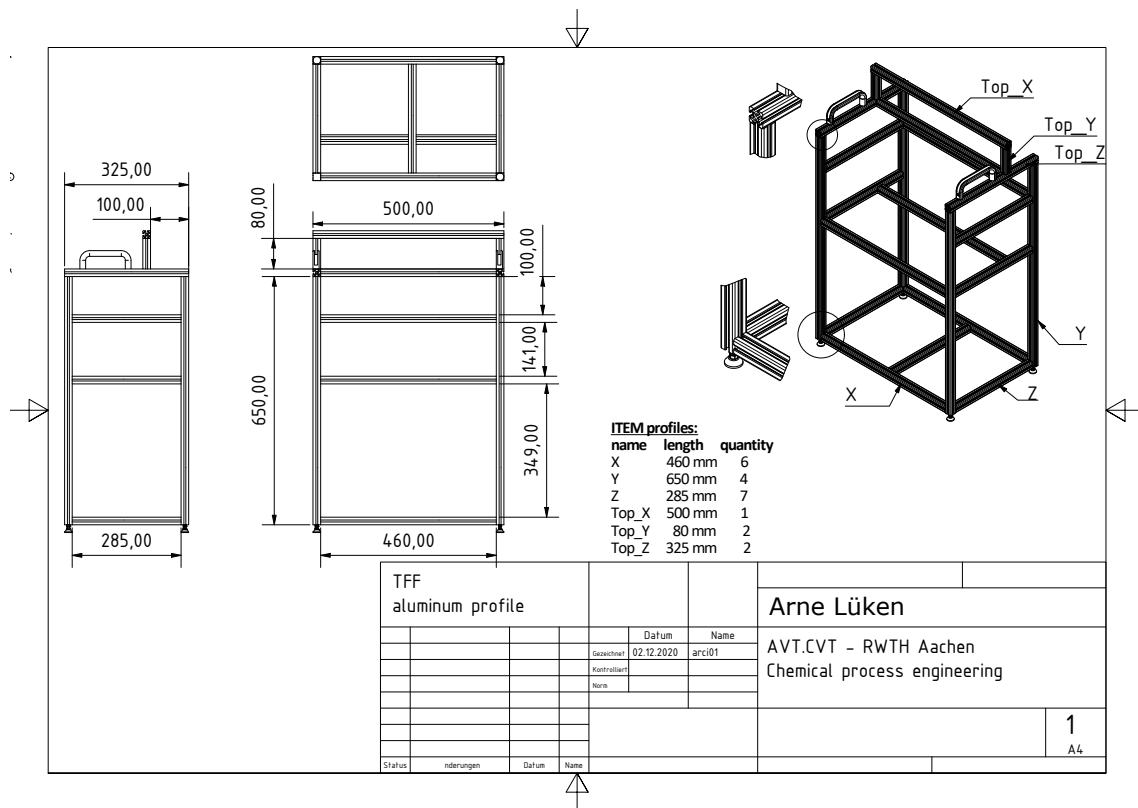


Figure 5.5: CAD-drawing of the aluminum cage assembly. Find the high quality image in the online repository

Afterward, all other mechanical components (pressure sensor holder, electric housing, valve holder, membrane module holder, and beaker fixation) are assembled as shown in Figure 5.3. Then, the electric pressure sensor (with *pipe clamp 25mm*), the back-pressure valve (with valve holder), the membrane module holder, and the assembled circuit board (inside the electric housing) are attached to the cage as shown in Figure 5.6 and Figure 5.7. The exact positions are not fixed and can be adapted to the purpose.

The water pump, the feed pump, the pulsation damper, and the beaker fixation are screwed onto the ground plate. Therefore, holes need to be drilled at the respective position. The pumps are additionally damped using rubbery dampers (Reichelt SMP 415 A15), one above and one underneath

the ground plate (compare with Figure 5.7 - pumps) to minimize pulsation transfer to the device. The beaker fixation is connected by one screw and can be adapted by approx. 1 cm to the beaker diameter. A close up of the assembly is shown in Figure 5.3 and in Figure 5.7 for the component beaker fixation bottom.

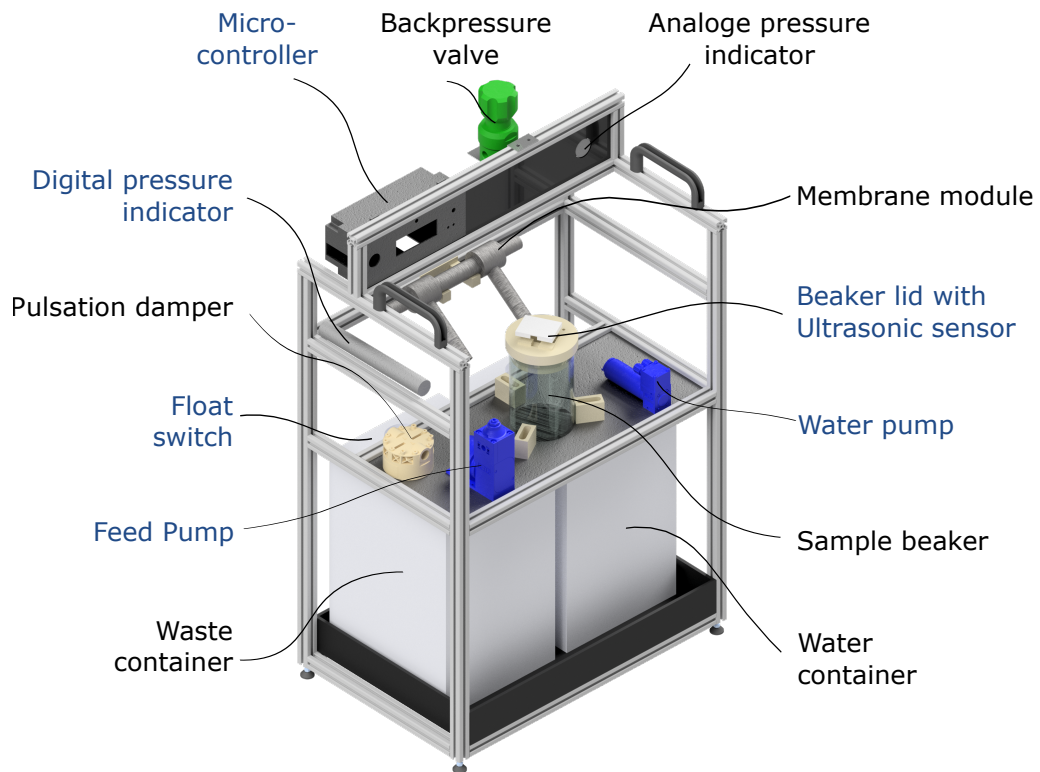


Figure 5.6: CAD-drawing of the filtration device assembly with all assembled components without tubing.

The ultrasonic sensor is put in the beaker lid and covered with the beaker lid cover. It holds in place without additional fixation. The float switch is included into the screw cap of the waste tanks by drilling a hole into the cap as seen in Figure 5.7 - float switch. The pumps and the other electric sensors (Pressure sensor, ultrasonic sensor, float switch) are afterward connected to the circuit board inside the electric housing.

The loose components, i.e., the tub, the water and waste tank, the sample beaker, and the beaker lid are put into position, and the 4mm tubing is connected to all components. Transparent, green, and blue tubing makes it possible to distinguish between high pressure tubing (feed), low pressure tubing (retentate), and the non-contaminated water cycle, respectively. The

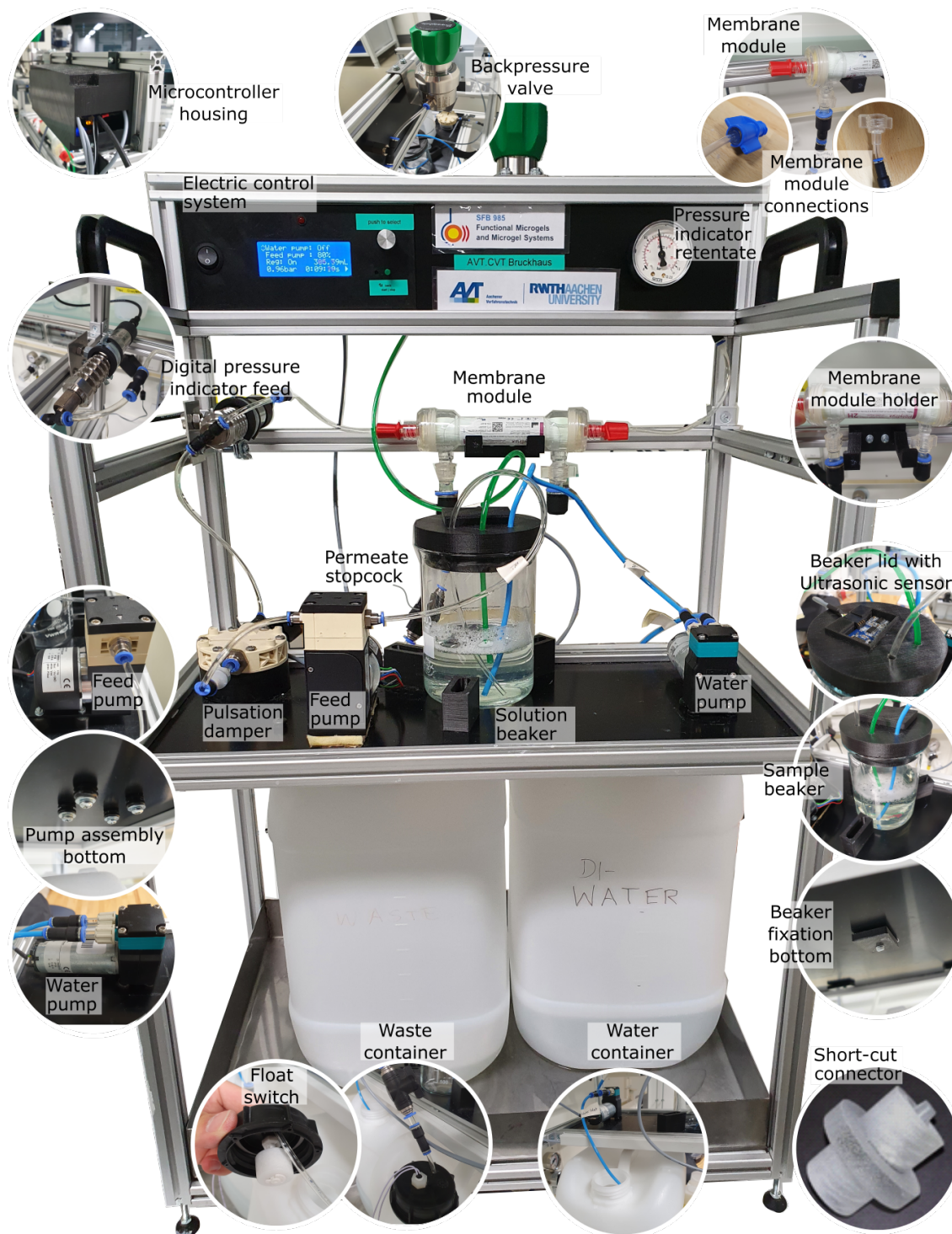


Figure 5.7: Image of the filtration device with assembly close-ups of all components.

tubing is connected to all components using Landefeld IQS connectors with the respective threads. The membrane module connection is glued to the tubing using a 2 component epoxy glue (UHU Schnellfest). The permeate

waste tubing is connected to one shell side of the membrane module, a stopcock is attached, and the tube is inserted into the waste tank by drilling a hole into the cap next to the float switch. The second permeate outlet of the membrane module is closed using a cap. Find images of the details in Figure 5.7.

5.6 Operation instructions

Table 5.3 shows a descriptive summary of the functions of the graphical user interface including descriptions of all settings. An exemplary operation instruction for microgel purification via diafiltration is shown in Table 5.4. The procedure includes the following steps:

- During device **preparation** the membrane module is installed, the microgel solution is filled in the sample beaker, the water tank is filled, and the waste tank is emptied (if necessary).
- **Dilution** needs to be performed if the sample volume is smaller than 100 ml. Operation volumes from 200-400 ml are suggested.
- During **diafiltration** the sample flows tangentially along the membrane, while the transmembrane pressure drives a share of the solvent and smaller molecules through the membrane. Additionally, it refills the sample beaker with pure water, so that the sample volume stays constant. This filtration step is performed until the solution is sufficiently purified. In our exemplary diafiltration using a 200 ml microgel solution (see section 5.7), this took approximately 2.6 l of permeate and 15 min of filtration using a Baxter Polyflux 6H hemodialysis membrane module. Adding a safety factor of 400 ml of filtrate results in a minimum of 3 liters of solvent exchange.
- After the filtration step, the solution is **concentrated** to the desired sample volume.
- The **flushing** step is essential to decrease colloidal microgel loss in the membrane module. Microgels accumulate on the membrane sur-

Table 5.3: GUI of the electric control system including a description of all settings.

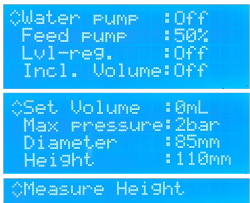
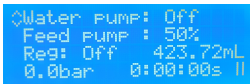
Settings 	Water pump	This value sets the initial state of the water pump when opening the operation mode. (ON/OFF)
	Feed pump	This value sets the initial state of the feed pump when opening the operation mode.(0-100%)
	Level regulation	Initial state of Level regulation when opening operation mode (ON/OFF). Level regulation performs diafiltration and keeps the liquid level constant over time by controls the water pump.
	Include volume	Considers the additional amount of water in the tubing during level regulation mode.
	Set volume	Sets the additional amount of water in the tubing.
	Max pressure	Sets the maximum pressure value.
	Diameter	Manual adjustment of beaker diameter.
	Height	Manual adjustment of the beaker height.
	Measure Height	Automatic beaker height measurement that is used for volume calculation. It measures height of empty beaker (empty beaker necessary)
Operation mode 	Water pump	State of the water pump (ON/OFF)
	Feed Pump	Power of the feed pump (0-100%)
	Level regulation	Level regulation = diafiltration (ON/OFF)
	xx.xx mL	Level indicator (liquid volume in solution beaker)
	x.x bar	Feed side pressure
	x:xx:xx s	Filtration time since start. Reset by going to main menu.
	>	Start/pause indicator of the process (push small button to start and pause)

Table 5.4: Exemplary operation instruction for microgel purification via diafiltration.

Preparation			Empty waste tank. Refill water tank to minimum of 4 L with DI-Water. Install membrane module between feed and retentate. Connect permeate connection /-stopcock to shell side. Connect the cap to the other shell side connection. Fill microgel solution in solution beaker and cover with lid. Submerge feed, retentate and water tubing in beaker.
Dilution Only necessary for small sample volumes	Water pump Feed Pump Level Regulation	ON 0% OFF	Start the device. Dilute sample by pumping water in the solution beaker. Run device until you reach a liquid level of 200-400 mL.
Diafiltration Purification of Sample	Water pump Feed Pump Level Regulation	ON/OFF 50% ON	Open the permeate stopcock. Adjust the back-pressure during operation to p=0.8-1 bar. Solvent is exchanged with fresh DI-water. Operate until min. 3 liters of DI-water is exchanged.
Concentration	Water pump Feed Pump Level Regulation	OFF 50% OFF	Remain permeate stopcock open. Operate device until required concentration is achieved.
Flushing End of purification	Water pump Feed Pump Level Regulation	OFF 100% OFF	Close permeate stopcock. Filter cake removal by cross-flow flushing. Flush tubing with air by taking feed tube out of solution.
Cleaning	Water pump Feed Pump Level Regulation	OFF 100% OFF	Exchange membrane module with short-cut connector. Exchange sample with 400ml of 10g/L Edisonide solution. Run device until solution tank is emptied. Repeat cleaning procedure with DI-water.

face as a filter cake. Higher permeation rates increase filter cake thickness. As the membrane area of the membrane modules is comparably large (0.2 m² for the 2H module or 0.6 m² for the 6H module), it can be a significant microgels loss in the filter cake, certainly for small sample volumes. This flushing step removes the filter cake from the membrane by suppressing permeation by closing the permeate stopcock and removing the cake by tangential cross-flow flushing. This method was proven in a previous study [Lücke2020]. Flushing times of 5 minutes with a maximum feed flow rate are recommended.

- Finally, the microgel solution is removed from the system by pulling the feed tubing out of the sample beaker, so that the pump empties the tubing by pumping air. The sample beaker is then exchanged with a beaker of cleaning agent (10 g/l Edisonite solution), which is subsequently flushed through all components to clean the internal surfaces. Therefore, the short-cut connector is replacing the membrane module so that the membrane might be reused for the same sample. This procedure is repeated with water to remove the cleaning agent. The system is finally stored in dry state.

An additional 7 minute long operation instruction video can be accessed via the online repository.

Mechanical hazards are distinguished between electrical and mechanical hazards. The system is operated with a commercial power supply with a maximum voltage of 24V, so that all voltages are lower than 24V and no electrical hazard occurs. Potential mechanical hazards result from the pressurized parts between the feed pump and the back-pressure valve, including the tubing, the IQS connections, and the membrane module. As pressurized volume is only liquid volume, an explosion is non-problematic, but splashing solutions might occur at leakages. Therefore, appropriate personal protective equipment, including goggles and lab coats, should be worn during operation. Device damages are secured by a software regulated maximum pressure error. This error automatically stops pumps and throws an alert if the feed pressure exceeds 2 bar. Finally, the risk of a fluid

spill is prevented by another software error: The system is automatically stopped when the water level in the sample beaker does not rise during the water pump operation. This behavior indicates either an empty water tank or a leakage somewhere in the system, where fluid might be spilled.

5.7 Purification of microgels using TFF

Microgels require an extensive purification step after synthesis to remove undesired side products and residuals. These contaminants are leftovers of monomers, surfactants that are desired for the reaction but undesired for the application, and linear pre-polymers that occur as side products. All of these molecules are significantly smaller than the desired microgels and can be removed using ultrafiltration.

This study evaluates the performance of the TFF-purification system by detecting leftovers of monomers and surfactant after purification. The microgel solution is analyzed using NMR and the purity of the permeate is analyzed by conductivity measurements at different time steps of the filtration. Additionally, the process-ability to remove linear polymer side products, that are not integrated in microgels, are evaluated using bubble pressure tensiometry. Finally, the diafiltration process is compared with an ultracentrifugation process. These results give a rough estimate on how long the diafiltration needs to be performed and additionally display the strengths and the limitations of microgel purification using diafiltration.

5.7.1 Experimentals

p-VCL microgels were synthesized using a continuous tube-reactor as described by Wolff et al. [Wolf2018]. In short, 14.76 g distilled and recrystallization VCL (98 % Sigma Aldrich) was mixed in 1 L aqueous solution with 0.402 g Cross-linker N,N'-methylenebis(acrylamide) (BIS) (99 %, Sigma-Aldrich) and 0.222 g surfactant hexadecyltrimethylammonium bromide (CTAB) (≥ 97 %, Merck). 0.883 g Initiator 2,2-azobis-(2-methyl propionamide)- dihydrochloride (AMPA) (97 %, Sigma-Aldrich) was dis-

solved in an second 50 ml aqueous solution. The two solutions were fed continuously into the tubular reactor using a syringe pump (Harvard PHD ULTRA) for the 50 ml solution and a gear pump (Ismatec MCP-Z) for the 1000 ml solution. The two solutions were mixed in a static mixer before entering the reactor. The reactor was heated to 70 °C, and the reaction time is set to 300 seconds by controlling the pumps' flowrates. The synthesis brew is directly used for the filtration process without previous purification.

Filtration of p-VCL microgels is performed using 200 ml of the synthesis brew as sample volume. The filtration device is equipped with a Baxter Polyflux 6H dialyzer membrane module with a membrane area of 0.6 m² and operated with a feed pump rate of 100 % at a feed pressure of 0.4 bar resulting in an average permeate flow rate of 175 mL/min. The filtration process was performed for 1 h, resulting in a total permeate volume of 10.5 L. During the filtration process, eight samples were taken from the sample beaker at different times to get a temporal resolution of the concentration of linear pre-polymers in the sample.

The p-VCL samples were analyzed using NMR. All samples were measured on a Bruker Avance III 400 spectrometer operating at 1H frequency of 400.17 MHz. One ml of each sample taken during the filtration is mixed with 20 vol % of deuterim oxide (D₂O) (99.9 %, Sigma-Aldrich).

p-NIPAM microgels were synthesized using a batch synthesis described by Senff et al. [Senff1999]. NIPAM monomer (205 mM, 9.27 g) and the surfactant Sodium dodecyl sulfate (SDS) (1.56 mM, 0.175 g) was mixed in 380 ml aqueous solution. This solution was heated to 70 °C and kept in inert gas-environment by bubbeling with nitrogen for 30 min. The initiator Potassium persulfate (KPS) (0.65mM, 70.3 mg) was dissolved in 20 ml and bubbled with nitrogen for 30 min as well. Then the reaction was initiated by adding the KPS-solution to the reactor and was kept running at 70 °C for 6 h. After cooling down the synthesis brew to room temperature, half of it (200 ml) were directly purified using ultracentrifugation and the remaining 200 ml were purified by dia-filtration with the filtration system described here.

Filtration of p-NIPAM microgels was performed using a Polyflux 2H dialyzer membrane module with a membrane area of 0.2 m². Due to the smaller membrane area, the permeate flow rate was significantly lower than for the p-VCL purification at approximately 50 ml/min. The filtration process was performed for 90 min and permeate samples were taken for conductivity and bubble pressure tensiometry measurements every 15 min.

The p-NIPAM permeate were analyzed measuring the permeate conductivity and bubble pressure tensiometry.

5.7.2 Results and discussion

NMR Analysis

The two microgels samples, p-VCL and p-NIPAM were analyzed using two different methods, that need to be considered complementary. The p-VCL sample was analyzed measuring the ¹H NMR of the microgel sample at different filtration times, which shows the overall analysis of the sample composition (Figure 5.8a). The microgels in the sample show broad peaks due to the slow molecular motion that leads to dipolar broadening. The narrow peaks can be assigned to small molecules (linear chains, other organic residues) that should be removed during filtration. After 15 minutes of filtration and an exchanged permeate volume of 2.6 liters, the narrow peaks disappeared, confirming that a purification occurred. The permeate volume linearly depends on the membrane area in the respective module, so that the Baxter 2H membrane module with 0.2 m² of membrane area will take triple time for the same outcome.

Conductivity and bubble pressure tensiometry

The NMR analysis of the p-VCL microgels proves the process functionality, but lacks in an analysis of different contaminants' removal efficiencies. Therefore, this study performed another analysis using p-NIPAM microgels measuring the conductivity of the permeate during filtration to prove separation efficiency of remaining reactants. Additionally, bubble pressure ten-

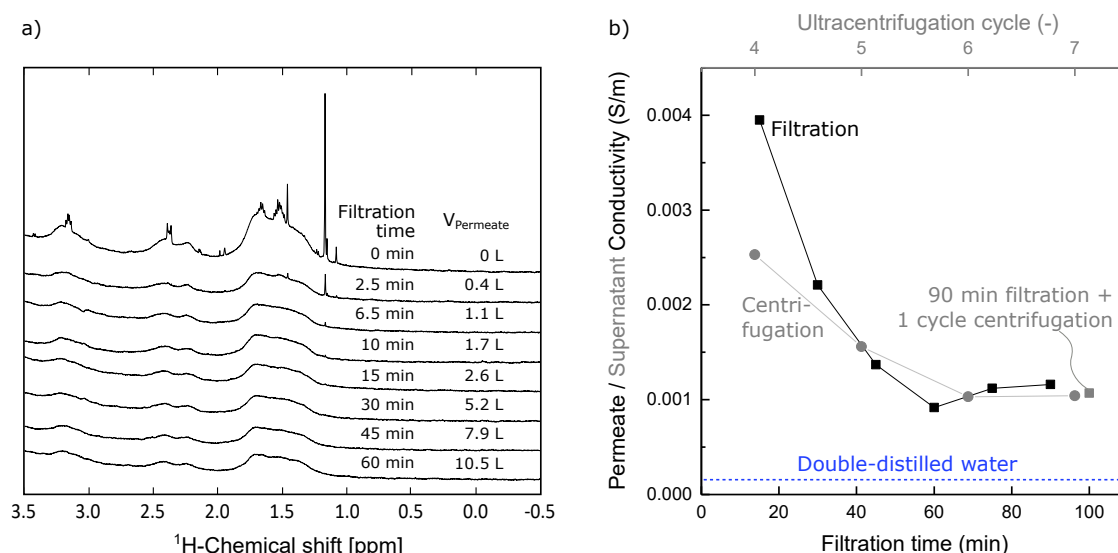


Figure 5.8: Verification of the microgel purification using NMR of the p-VCL microgel sample at different filtration times using a 6H membrane module with a membrane area of 0.6 m^2 (a). Conductivity measurements of the permeate and supernatant of the p-NIPAM sample purified by filtration using a 2H membrane module with a membrane area of 0.2 m^2 (black) and ultracentrifugation (grey), respectively. Additionally, the most right data-point shows the permeate sample after 90 min of filtration with an additional centrifugation cycle.

siometry is performed for analyzing the removal efficiency of surface active substances. In bubble pressure tensiometry, the surface tension γ (mN/m) of a bubble is measured at different surface ages τ (ms). τ represents the reaction time of the surface active molecule and decreased γ than pure water reveals the existence of the surface active substances. Linear polymers show a high affinity for contacting the gas-liquid interface of a bubble and influence the bubble pressure significantly. Accordingly, bubble pressure tensiometry can be used as a tool for analyzing the existence of high-molecular polymers, such as linear pre-polymers, in the permeate or the supernatant. Both data is compared with the supernatant of a ultra-centrifugation after 4-7 cycles.

The conductivity measurements (Figure 5.8b) reveal that the conductivity remains in a steady state after 45-60 min of filtration. The ultra-centrifugation reaches the same results within 6 cycles. One additional centrifugation cycle of the 90 min filtrated microgel sample (grey square) proves, that the filtration process equals the ultra-centrifugation process in

terms of conductivity of the sample. It can be concluded that 60 min of filtration using a 0.2 m² membrane module shows comparable results related to remaining reactants in the microgel sample.

The bubble pressure tensiometry serves as a tool for analyzing the removal efficiency of linear pre-polymers. The measurements of the ultra-centrifugation process reveal that each cycle of centrifugation removes some shares of polymer up to the 7th cycle (Figure 5.9b). The permeate of the filtration process (Figure 5.9a) shows a similar behavior for the 15 min to 45 min sample, revealing that a share of linear pre-polymer is being removed. However, the subsequent centrifugation shows an additional removal of surface active substances in the supernatant, which can be associated to a insufficient removal of larger polymers in the filtration process. The applied membrane has a MWCO of 30 kDa, so that large-molecular polymers (> 30 kDa) will be retained by the membrane. For removing larger pre-polymers, a membrane with larger MWCO must be chosen. Accordingly, removal of contaminants by filtration shows the same boundary conditions as a purification performed by dialysis.

Microgel loss

During the process, microgels accumulate inside the module on the membrane surface as monolayer and filter cake. The post purification cross-flow flushing step removes a share of these microgels. However, polymer adhering in the inner pore structure and as monolayer on the membrane surface will hardly be affected by the proposed cross flow cleaning method. Removal would require a much stronger cleaning method, such as back-flushing and chemical cleaning, which is not suggested in this setup due to complexity of the required instrumentation. Accordingly, a membrane surface-area dependent microgel loss is obtained inside the membrane module during the diafiltration-process. This microgel-loss is evaluated by performing another experiment filtrating a purified 200 ml pVCL solution with a concentration of 2.7 g/L. After 20 min of diafiltration using a Baxter 6H module, a concentration of 1.6 g/L was measured. Thus, the process

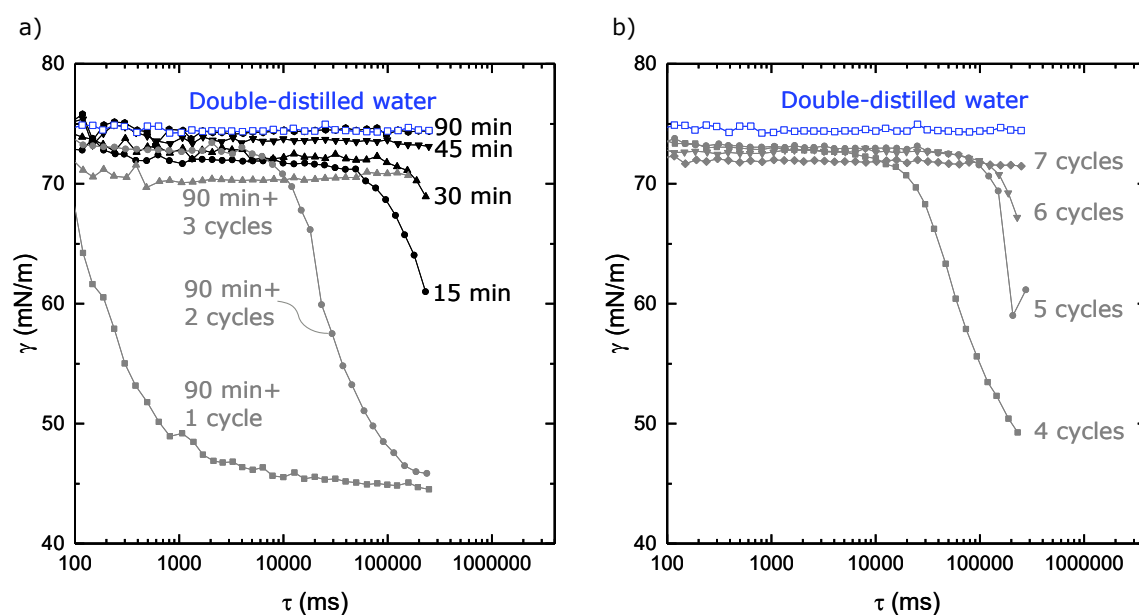


Figure 5.9: Bubble pressure tensiometry of the permeate and supernatant of a p-NIPAM microgel purification performed by filtration and ultracentrifugation, respectively. (a) shows the permeate at different filtration times (black) and additionally the supernatant of the centrifugated sample after 90 min of filtration (grey). (b) shows bubble pressure tensiometry measurements using ultra-centrifugation as purification method after 4-7 cycles.

lost approximately a total mass of 0.22 g microgels on a membrane area of 0.6 m². This loss mainly affects small sample volumes with small concentrations because it correlates to the membrane area and not to the sample concentration and sample volume. The membrane module should be selected appropriately for the filtration task.

5.8 Summary

The ultrafiltration device presented here opens the technology of tangential-flow diafiltration to polymer science research labs by reducing investment and operational costs. The technology outstands the existing state of the art purification technologies like dialysis or ultracentrifugation in terms of costs, time, and manual effort.

Purification of microgels by TFF shows promising results related to the removal of reactants and small molecular polymers. Depending on the

membrane module 15-60 min of filtration suffice for purifying a 200 ml batch of microgels. Our example using a 30 kDa MWCO membrane revealed an insufficient removal of large molecular p-NIPAM polymers. For a removal of components larger than 30 kDa a membrane with larger MWCO should be chosen. The upper limit pore size is defined by the microgel retention.

6 Conclusion and Perspectives

This thesis analyzes the filtration of colloidal microgels and soft micro-particles, focusing on particle scale phenomena occurring during filter cake formation in MF and UF processes. Such filtration processes have been analyzed on a micro-scale using microfluidic devices and on a lab-scale applying flat sheet and hollow fiber membrane modules.

Cake compaction A microfluidic dead-end model system to analyze the formation and compaction of soft particle filter cakes was developed and applied for visualizing single particle movements in a filter cake and their influence on the overall cake morphology. During a constant pressure cake built up, the cake compacts by particles filling up voids towards the membrane surface. After a certain number of rearrangements, this process calms down for the layers close to the membrane, indicating a complete void filling. Compression of the filter cake enables additional fill-up events by deforming and squeezing particles into existing smaller voids. The packing density strongly depends on the previous permeation and compression history, nicely mimicking biofilm compressibility in UF applications [Jafa2019].

Particle shape affecting hydraulic resistance The follow-up study increases complexity towards approximating filtration processes by introducing a microfluidic any-shape particle fabrication process. The vertical flow lithography suits as a high throughput method for fabricating microscopic particles in any 3D shape. Evolving from there, in-channel particle fabrication into a confined microfluidic chamber with a resting fluid enables the precise fabrication of a defined number of particles. The particle's shape

and stiffness strongly influence the filter cake's hydraulic resistance and morphology by modifying the contact points between the particles and their ability to deform and fill up voids in the cake. The study represents an unprecedented description of microscopic in-flow particle assembly and the assembly's hydraulic resistance highlighting the importance of considering the particle's shape during filtration.

In-flow assembled bio-hybrid tissues Looking at filter cakes from a different point of view, they also represent densely packed and permeated assemblies of particles and colloids. The creation and permeation of such assemblies are important in chromatography columns, packed beds in chemical and biochemical reactors, and scaffolds for tissue engineering. This thesis presents the in-flow assembly process of rigid and soft micro-particles. The morphology of the final assembly depends strongly on its formation process, which results from solvent depending particle-particle interactions. Particles' interactions and their tendency to assemble were extensively studied for nano-particle within the last 30 years [Nied2017]. All the progress in nano-particle assembly ranging from molecular synthesis to controlled 1D, 2D and 3D arrangement, emerges in assemblies with tremendous precision by considering all material properties, including composition, crystal structure, surface chemistry and morphology. However, nano-particle self-assemblies are restricted to a few tens of micrometers. [Nied2017]; [Anto2008] Accomplishing technical applications requires larger micron-scale building blocks by transferring molecular synthesis routes and nano-particle properties to 3D micro-particle fabrication and functionalization. The micro-particle shape determines the particle-contact points and thereby activates the interaction of particles depending on their properties, including charge, softness, and solvent wettability [Zhan2012]; [Wang2018].

The microfluidic methods for particle fabrication and filtration presented in this thesis potentially enable layer-by-layer in-flow particle self-assembly, creating a 3D structure similar to the various applications in layer-by-layer assemblies of nano-particles and macromolecules [Rich2016]. The roadmap

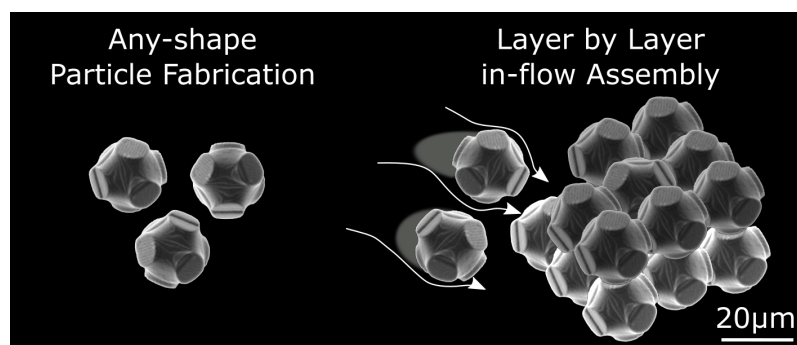


Figure 6.1: Visionary layer-by-layer in-flow 3D assembly of microscopic any-shape particles

towards a controlled macroscopic 3D-assembly using, e.g., the any-shape particles from Chapter 3, includes precise tuning and analysis of the particles' shape, their solvent contact angle, their softness, the particle-particle adhesion, and the forces applied during the in-flow assembly process. Finally, a controlled porous scaffold might serve as self-assembled bio-hybrid tissue with adjustable porosity (Figure 6.1).

Colloidal cake layer morphology This thesis combines optical visualization methods for describing dynamic movements of the particles and the filter cake with traditional measurements of the flux and the trans-membrane pressure. Thereby, it narrows the gap between microscopic particle interaction and filter cake properties. However, it is still challenging to translate single particle events to macroscopic, process scale filtration models.

The presented unique combination of CLSM in a flat sheet membrane cell allows the in-situ 3D visualization of filter cakes during a filtration process. Visualizing the cake mobility and its dynamic movements during cross-flow filtration unravels longitudinal patterns on the cake bulk boundary resulting from instabilities at the boundary layer with viscosity gradients. These instabilities accelerate the colloid transport to the bulk and reduce cake removal times. This reproducible phenomenon is expected to occur on any viscous boundary layer impacting filter cakes, where particles are not fixed in the gel layer structure but can flow on the surface of the cake. Future studies could investigate the influence on industrial applica-

tions, e.g., in tangential-flow dairy and protein filtration.

Additionally, the CLSM cake visualization method allows a particle scale analysis of the cake density during a filtration process. In future work, the acquisition of depth density gradients on real filter cakes using this method would translate the morphology to a more mechanistic description of filter cakes. The system raises the question of how the fluid is transported through a packed bed of soft particles and colloids. Soft particle deformation [Bouh2017]; [Link2019], gel layer permeation [Jafa2019], as well as the transport phenomena in gels, such as in soft chromatography columns [Plue1999] needs to be considered. This translation will substantially result in a rather mechanistic description of the cake layer permeation compared to Karman Cozeny based models with experimental filtrate specific cake resistance values [Fole2006].

Purification of microgels using UF Microgels are microscopic water-swollen crosslinked colloidal networks that can be engineered to respond to external stimuli, such as temperature or pH [Karg2019]. Microgels show promising applications as drug carriers in clinical attempts [Kitt2021], though they are still primarily applied in academic research. The downstream process in lab-scale is either performed by batch dialysis or by ultracentrifugation. Both methods are hardly upscale-able and not suited for larger-scale fabrication. This thesis suggests a semi-continuous and easily upscalable tangential flow diafiltration process for purification. Commercial, low-cost hemodialysis hollow fiber membrane modules are applied to purify microgels. The technology allows a fast and reliable separation of low-molecular residuals. At the same time, large molecular polymer strains remain in the microgel solution due to the separation properties of the chosen membrane. Accordingly, the membrane module needs to be selected for the respective microgel and its precise purification target. Pushing the microgel-research towards future applications will increase the sizes of the synthesis batches and carve out the advantages of the diafiltration process. Therefore, at present, various projects in the Collaborative Research Center (SFB 985) and at the chair of chemical process engineering at RWTH Aachen

University started applying the here developed diafiltration technology for the purification of microgels. The microscopic cake layer phenomena studied in the prior chapters of this thesis, including the cake compaction and the 3D patterns on the cake surface, occur on a day's basis during the tangential-flow purification of microgels in these ongoing projects.

Bibliography

- [Ande2013] K. B. Anderson et al. "A 3D printed fluidic device that enables integrated features". *Analytical chemistry* 85.12 (2013). DOI: 10.1021/ac4009594 (cit. on p. 15).
- [Anse2015] A. C. Anselmo et al. "Elasticity of nanoparticles influences their blood circulation, phagocytosis, endocytosis, and targeting". *ACS nano* 9.3 (2015). DOI: 10.1021/acsnano.5b00147 (cit. on p. 33).
- [Anto2008] M. Antonietti, M. Niederberger, and B. Smarsly. "Self-assembly in inorganic and hybrid systems: beyond the molecular scale". *Dalton transactions (Cambridge, England : 2003)* 1 (2008). DOI: 10.1039/b711529f (cit. on p. 110).
- [Anto2012] P. G. Antolli and Z. Liu. *Bioreactors: Design, properties, and applications*. Biochemistry research trends. New York: NOVA/Nova Science Publishers, 2012 (cit. on p. 40).
- [Armb2018] S. Armbruster et al. "Fouling mitigation in tubular membranes by 3D-printed turbulence promoters". *Journal of Membrane Science* 554.1 (2018). DOI: 10.1016/j.memsci.2018.02.015 (cit. on p. 16).
- [Bacc2002] P. Bacchin et al. "A unifying model for concentration polarization, gel-layer formation and particle deposition in cross-flow membrane filtration of colloidal suspensions". *Chemical Engineering Science* 57.1 (2002). (Cit. on p. 23).
- [Bacc2011] P. Bacchin et al. "Colloidal surface interactions and membrane fouling: investigations at pore scale". *Advances in colloid and interface science* 164.1-2 (2011). DOI: 10.1016/j.cis.2010.10.005 (cit. on pp. 14, 24, 64, 65).
- [Bait2021] K. Baitalow et al. "A mini-module with embedded spacers for high-throughput ultrafiltration". *Journal of Membrane Science* 637 (2021). (Cit. on p. 15).

- [Bake2004] R. W. Baker. *Membrane technology and applications*. 2nd ed. Chichester and New York: J. Wiley, 2004 (cit. on pp. 4–7, 9, 22, 64, 65, 84).
- [Bann2016] S. Bannwarth et al. “On-line monitoring of cake layer structure during fouling on porous membranes by in situ electrical impedance analysis”. *Journal of Membrane Science* 503 (2016). DOI: 10.1016/j.memsci.2016.01.009 (cit. on p. 65).
- [Beau2011] S. Beaufort, S. Alfenore, and C. Lafforgue. “Use of fluorescent microorganisms to perform in vivo and in situ local characterization of microbial deposits”. *Journal of Membrane Science* 369.1-2 (2011). DOI: 10.1016/j.memsci.2010.11.023 (cit. on p. 12).
- [Belf2019] G. Belfort. “Membrane Filtration with Liquids: A Global Approach with Prior Successes, New Developments and Unresolved Challenges”. *Angewandte Chemie (International ed. in English)* 58.7 (2019). DOI: 10.1002/anie.201809548 (cit. on pp. 1, 2).
- [Bell2020] D. J. Bell et al. “Hydrogel membranes made from crosslinked microgel multilayers with tunable density”. *Journal of Membrane Science* (2020). DOI: 10.1016/j.memsci.2020.118912 (cit. on p. 22).
- [Ben 2014a] I. Ben Hassan et al. “in situ 3D characterization of bidisperse cakes using confocal laser scanning microscopy”. *Journal of Membrane Science* 466 (2014). DOI: 10.1016/j.memsci.2014.04.041 (cit. on p. 12).
- [Ben 2014b] I. Ben Hassan et al. “In situ 3D characterization of monodispersed spherical particle deposition on microsieves using confocal laser scanning microscopy”. *Journal of Membrane Science* 454 (2014). DOI: 10.1016/j.memsci.2013.12.003 (cit. on p. 12).
- [Bere2010] L. A. Bereschenko et al. “Biofilm formation on reverse osmosis membranes is initiated and dominated by *Sphingomonas* spp”. *Applied and environmental microbiology* 76.8 (2010). DOI: 10.1128/AEM.01998-09 (cit. on p. 12).
- [Berg2018a] M. J. Bergman et al. “A new look at effective interactions between microgel particles”. *Nature communications* 9.1 (2018). (Cit. on p. 36).

- [Berg2018b] M. J. Bergman et al. "A new look at effective interactions between microgel particles". *Nature communications* 9.1 (2018). DOI: 10 . 1038/s41467-018-07332-5 (cit. on p. 65).
- [Blei2018] C. Bleilevens et al. "Microfluidic cell sorting: Towards improved bio-compatibility of extracorporeal lung assist devices". *Scientific reports* 8.1 (2018). DOI: 10 . 1038 / s41598 - 018 - 25977 - 6 (cit. on p. 25).
- [Bosc2013] A. Boschetti-de-Fierro et al. "Extended characterization of a new class of membranes for blood purification: the high cut-off membranes". *The International journal of artificial organs* 36.7 (2013). DOI: 10.5301/ijao.5000220 (cit. on p. 86).
- [Bouc2014] A. Bouchoux et al. "A general approach for predicting the filtration of soft and permeable colloids: the milk example". *Langmuir* 30.1 (2014). (Cit. on p. 23).
- [Bouh2017] I. Bouhid de Aguiar et al. "Deswelling and deformation of microgels in concentrated packings". *Scientific reports* 7.1 (2017). DOI: 10 . 1038/s41598-017-10788-y (cit. on pp. 23, 42, 65, 112).
- [Bouh2018] I. Bouhid de Aguiar et al. "Compressive resistance of granular-scale microgels: From loose to dense packing". *Colloids and Surfaces A: Physicochemical and Engineering Aspects* 553 (2018). DOI: 10.1016/j.colsurfa.2018.05.064 (cit. on p. 22).
- [Bouh2019a] I. Bouhid de Aguiar et al. "Conformational changes influence clogging behavior of micrometer-sized microgels in idealized multiple constrictions". *Scientific reports* 9.1 (2019). DOI: 10.1038/s41598-019-45791-y (cit. on pp. 10, 14, 24).
- [Bouh2019b] I. Bouhid de Aguiar et al. "Microfluidic model systems used to emulate processes occurring during soft particle filtration". *Scientific reports* 9.1 (2019). DOI: 10 . 1038 / s41598 - 019 - 39820 - z (cit. on p. 24).
- [Bouh2020] I. Bouhid de Aguiar and K. Schroën. "Microfluidics Used as a Tool to Understand and Optimize Membrane Filtration Processes". *Membranes* 10.11 (2020). DOI: 10 . 3390 / membranes10110316 (cit. on pp. 14, 15, 24, 51).

- [Bran2007] G. Brans et al. "Transmission and fractionation of micro-sized particle suspensions". *Journal of Membrane Science* 290.1-2 (2007). DOI: 10.1016/j.memsci.2006.12.045 (cit. on p. 12).
- [Brun2015] K. M. Brunner et al. "Effects of Particle Size and Shape on the Performance of a Trickle Fixed-Bed Recycle Reactor for Fischer–Tropsch Synthesis". *Industrial & Engineering Chemistry Research* 54.11 (2015). DOI: 10.1021/ie503174v (cit. on p. 41).
- [Bugg2012] T. V. Bugge et al. "Modeling cake buildup under TMP-step filtration in a membrane bioreactor: Cake compressibility is significant". *Water research* 46.14 (2012). (Cit. on p. 23).
- [Cars2012] F. Carstensen, A. Apel, and M. Wessling. "In situ product recovery: Submerged membranes vs. external loop membranes". *Journal of Membrane Science* 394-395 (2012). DOI: 10.1016/j.memsci.2011.11.029 (cit. on p. 84).
- [Char2006] C. Charcosset. "Membrane processes in biotechnology: an overview". *Biotechnology advances* 24.5 (2006). DOI: 10.1016/j.biotechadv.2006.03.002 (cit. on p. 3).
- [Cous2011] W. G. Couser et al. "The contribution of chronic kidney disease to the global burden of major noncommunicable diseases". *Kidney international* 80.12 (2011). DOI: 10.1038/ki.2011.368 (cit. on p. 86).
- [Dend2006] D. Dendukuri et al. "Continuous-flow lithography for high-throughput microparticle synthesis". *Nature materials* 5.5 (2006). DOI: 10.1038/nmat1617 (cit. on p. 41).
- [Dend2007] D. Dendukuri et al. "Stop-flow lithography in a microfluidic device". *Lab on a chip* 7.7 (2007). DOI: 10.1039/b703457a (cit. on p. 41).
- [Desm2018] P. Desmond, E. Morgenroth, and N. Derlon. "Physical structure determines compression of membrane biofilms during Gravity Driven Membrane (GDM) ultrafiltration". *Water Research* 143 (2018). DOI: 10.1016/j.watres.2018.07.008 (cit. on p. 15).
- [Di L2013] F. Di Lorenzo and S. Seiffert. "Macro- and Microrheology of Heterogeneous Microgel Packings". *Macromolecules* 46.5 (2013). DOI: 10.1021/ma302255x (cit. on p. 23).

- [Di2017] H. Di, G. J. Martin, and D. E. Dunstan. "A microfluidic system for studying particle deposition during ultrafiltration". *Journal of Membrane Science* 532 (2017). DOI: 10.1016/j.memsci.2017.03.017 (cit. on pp. 12, 72).
- [Di2018] H. Di et al. "Detailed, real-time characterization of particle deposition during crossflow filtration as influenced by solution properties". *Journal of Membrane Science* 555 (2018). DOI: 10.1016/j.memsci.2018.03.021 (cit. on p. 12).
- [Dias2017] A. D. Dias, J. M. Elicson, and W. L. Murphy. "Microcarriers with Synthetic Hydrogel Surfaces for Stem Cell Expansion". *Advanced healthcare materials* 6.16 (2017). DOI: 10.1002/adhm.201700072 (cit. on p. 40).
- [Diel2005] B. Diel. "Device and assembly for crossflow filtration". *United States Patent* -.US 6,929,743 B2 (2005). (Cit. on p. 86).
- [Dohe2020] R. P. Doherty et al. "Catalytically propelled 3D printed colloidal microswimmers". *Soft matter* (2020). DOI: 10.1039/d0sm01320j (cit. on p. 41).
- [Dres2016] E. Dressaire and A. Sauret. "Clogging of microfluidic systems". *Soft matter* 13.1 (2016). DOI: 10.1039/c6sm01879c (cit. on p. 14).
- [Dull2006] R. P. A. Dullens et al. "Shape-induced frustration of hexagonal order in polyhedral colloids". *Physical review letters* 96.2 (2006). DOI: 10.1103/PhysRevLett.96.028304 (cit. on p. 23).
- [Eghb2016] H. Eghbali et al. "Hollow fiber bioreactor technology for tissue engineering applications". *The International journal of artificial organs* 39.1 (2016). DOI: 10.5301/ijao.5000466 (cit. on p. 40).
- [Eins1905] A. Einstein. "Über die von der molekularkinetischen Theorie der Wärme geforderte Bewegung von in ruhenden Flüssigkeiten suspendierten Teilchen". *Annalen der physik* 4 (1905). (Cit. on p. 5).
- [Epst2021] J. A. Epstein and G. Z. Ramon. "In-situ micro-rheology of a foulant layer at a membrane surface". *Journal of Membrane Science* 640.1–2 (2021). DOI: 10.1016/j.memsci.2021.119747 (cit. on p. 13).
- [Fiel1995] R. W. Field et al. "Critical flux concept for microfiltration fouling". *Journal of Membrane Science* 100.3 (1995). (Cit. on p. 8).

- [Flai2019] S. Flaischlen and G. D. Wehinger. “Synthetic Packed-Bed Generation for CFD Simulations: Blender vs. STAR-CCM+”. *ChemEngineering* 3.2 (2019). DOI: 10.3390/chemengineering3020052 (cit. on p. 41).
- [Fole2006] G. Foley. “A review of factors affecting filter cake properties in dead-end microfiltration of microbial suspensions”. *Journal of Membrane Science* 274.1-2 (2006). DOI: 10.1016/j.memsci.2005.12.008 (cit. on pp. 10, 22, 23, 40, 112).
- [Fröh2012] H. Fröhlich et al. “Membrane Technology in Bioprocess Science”. *Chemie Ingenieur Technik* 297.4 (2012). DOI: 10.1002/cite.201200025 (cit. on p. 3).
- [Geno2011] D. Genovese and J. Sprakel. “Crystallization and intermittent dynamics in constricted microfluidic flows of dense suspensions”. *Soft matter* 7.8 (2011). DOI: 10.1039/c0sm01338b (cit. on p. 72).
- [Geor2001] Georges Daufin et al. “Recent and emerging application of membrane processes in food and dairy industry”. *Food and Bioproducts Processing* 79.2 (2001). (Cit. on p. 4).
- [Gnan2019] N. Gnan and E. Zaccarelli. “The microscopic role of deformation in the dynamics of soft colloids”. *Nature Physics* 15.7 (2019). DOI: 10.1038/s41567-019-0480-1 (cit. on pp. 36, 65).
- [Go2014] D. Go et al. “Programmable co-assembly of oppositely charged microgels”. *Soft matter* 10.40 (2014). DOI: 10.1039/c4sm01570c (cit. on p. 67).
- [Goni2010] C. Goniva et al. *An open source CFD-DEM perspective*. Vol. 22-24. Proceedings of OpenFOAM Workshop, Goeteborg, 2010 (cit. on p. 27).
- [Gons1950] V. E. Gonsalves. “A critical investigation on the viscose filtration process”. *Recueil des Travaux Chimiques des Pays-Bas* 69.7 (1950). (Cit. on p. 8).
- [Grif2022] I. M. Griffiths and P. S. Stewart. “A hybrid discrete–continuum framework for modelling filtration”. *Journal of Membrane Science* (2022). DOI: 10.1016/j.memsci.2022.120258 (cit. on pp. 10, 14).

- [Haba2015] S. Habasaki et al. "Vertical Flow Lithography for Fabrication of 3D Anisotropic Particles". *Small (Weinheim an der Bergstrasse, Germany)* 11.48 (2015). DOI: 10.1002/smll.201502968 (cit. on p. 42).
- [Hash2009] S. M. Hashmi and E. R. Dufresne. "Mechanical properties of individual microgel particles through the deswelling transition". *Soft Matter* 5.19 (2009). (Cit. on p. 36).
- [Hend2010] G. R. Hendrickson and L. A. Lyon. "Microgel translocation through pores under confinement". *Angewandte Chemie (International ed. in English)* 49.12 (2010). DOI: 10.1002/anie.200906606 (cit. on p. 65).
- [Herm1936] P. H. Hermans. "Principles of the Mathematical Treatment of Constant-Pressure Filtration". *J. Soc. Chem. Ind.* 55 (1936). (Cit. on p. 8).
- [Herm1985] J. Hermia, ed. *Mathematical Models and Design Methods in Solid-Liquid Separation*. Vol. 88. NATO ASI Series, Series E. Dordrecht: Springer, 1985. DOI: 10.1007/978-94-009-5091-7 (cit. on pp. 8, 9).
- [Herr2013] W. G. Herrick et al. "PEG-phosphorylcholine hydrogels as tunable and versatile platforms for mechanobiology". *Biomacromolecules* 14.7 (2013). DOI: 10.1021/bm400418g (cit. on p. 33).
- [Hlav1993] M. Hlavacek and F. Bouchet. "Constant flowrate blocking laws and an example of their application to dead-end microfiltration of protein solutions". *Journal of Membrane Science* 82.3 (1993). DOI: 10.1016/0376-7388(93)85193-z (cit. on p. 8).
- [Ho2000] Ho and Zydney. "A Combined Pore Blockage and Cake Filtration Model for Protein Fouling during Microfiltration". *Journal of Colloid and Interface Science* 232.2 (2000). DOI: 10.1006/jcis.2000.7231 (cit. on p. 8).
- [Ho2016] J. S. Ho et al. "In-situ monitoring of biofouling on reverse osmosis membranes: Detection and mechanistic study using electrical impedance spectroscopy". *Journal of Membrane Science* 518 (2016). DOI: 10.1016/j.memsci.2016.06.043 (cit. on p. 65).

- [Hugh2006] D. Hughes et al. "In situ 3D characterization of membrane fouling by yeast suspensions using two-photon femtosecond near infrared non-linear optical imaging". *Journal of Membrane Science* 280.1-2 (2006). DOI: 10.1016/j.memsci.2006.01.017 (cit. on p. 65).
- [Hwan2001] K.-J. Hwang, Y.-H. Yu, and W.-M. Lub. "Cross-flow microfiltration of submicron microbial suspension". *Journal of Membrane Science* 194 (2001). DOI: 10.1016/S0376-7388(01)00547-6 (cit. on p. 64).
- [Hwan2003] K.-J. Hwang and C.-L. Hsueh. "Dynamic analysis of cake properties in microfiltration of soft colloids". *Journal of Membrane Science* 214.2 (2003). DOI: 10.1016/S0376-7388(02)00556-2 (cit. on pp. 22, 23).
- [Hwan2009] K.-J. Hwang et al. "Effects of porous gel particle compression properties on microfiltration characteristics". *Journal of Membrane Science* 341.1-2 (2009). DOI: 10.1016/j.memsci.2009.06.029 (cit. on p. 22).
- [Hwan2010] K.-J. Hwang et al. "Effect of gel particle softness on the performance of cross-flow microfiltration". *Journal of Membrane Science* 365.1-2 (2010). DOI: 10.1016/j.memsci.2010.08.043 (cit. on pp. 23, 64).
- [Jafa2019] M. Jafari et al. "Biofilm compressibility in ultrafiltration: A relation between biofilm morphology, mechanics and hydraulic resistance". *Water Research* 157 (2019). DOI: 10.1016/j.watres.2019.03.073 (cit. on pp. 15, 53, 109, 112).
- [Jans2017] A. Jans et al. "Glycan-Functionalized Microgels for Scavenging and Specific Binding of Lectins". *Biomacromolecules* 18.5 (2017). DOI: 10.1021/acs.biomac.6b01754 (cit. on p. 25).
- [Jean1996] Jean-Louis Lanoiselle et al. "Modeling of solid/liquid expression for cellular materials". *AIChE Journal* 42.7 (1996). (Cit. on p. 65).
- [Jiao2004] B. Jiao, A. Cassano, and E. Drioli. "Recent advances on membrane processes for the concentration of fruit juices: a review". *Journal of food engineering* 63.3 (2004). (Cit. on p. 3).
- [John2021] John Linkhorst et al. "Templating the morphology of soft microgel assemblies using a nanolithographic 3D-printed membrane". *Scientific Reports* 11 (2021). (Cit. on pp. 15, 16, 24).

- [Jong2006] J. de Jong, R. G. H. Lammertink, and M. Wessling. "Membranes and microfluidics: a review". *Lab on a chip* 6.9 (2006). DOI: 10.1039/b603275c (cit. on p. 13).
- [Jons1984] Jonsson, G. "Boundary layer phenomena during ultrafiltration of dextran and whey protein solutions". *Desalination* 51.1 (1984). (Cit. on pp. 65, 66, 74, 79).
- [Jons1986] Jonsson, G. "Transport phenomena in ultrafiltration: membrane selectivity and boundary layer phenomena". *Pure and Applied Chemistry* 59.12 (1986). (Cit. on pp. 66, 79).
- [Jørg2014] M. K. Jørgensen, K. Keiding, and M. L. Christensen. "On the reversibility of cake buildup and compression in a membrane bioreactor". *Journal of Membrane Science* 455 (2014). DOI: 10.1016/j.memsci.2013.12.052 (cit. on p. 22).
- [Jose1984] Joseph, D. D., Nguyen, K., and Beavers, G. S. "Non-uniqueness and stability of the configuration of flow of immiscible fluids with different viscosities". *Journal of Fluid Dynamics* 141 (1984). (Cit. on pp. 66, 80).
- [Karg2019] M. Karg et al. "Nanogels and Microgels: From Model Colloids to Applications, Recent Developments, and Future Trends". *Langmuir : the ACS journal of surfaces and colloids* (2019). DOI: 10.1021/acs.langmuir.8b04304 (cit. on p. 112).
- [Kerd2019] S. Kerdi et al. "An in-situ technique for the direct structural characterization of biofouling in membrane filtration". *Journal of Membrane Science* 583.3 (2019). DOI: 10.1016/j.memsci.2019.04.051 (cit. on p. 15).
- [Kirs2019] A. Y. Kirschner et al. "Fouling mechanisms in constant flux cross-flow ultrafiltration". *Journal of Membrane Science* 574 (2019). DOI: 10.1016/j.memsci.2018.12.001 (cit. on p. 8).
- [Kiss2018] B. Kiss, U. Gottschalk, and M. Pohlscheidt. *New Bioprocessing Strategies: Development and Manufacturing of Recombinant Antibodies and Proteins*. Springer, 2018 (cit. on p. 40).
- [Kitt2021] Y. Kittel, A. J. Kuehne, and L. De Laporte. "Translating therapeutic microgels into clinical applications". *Advanced Healthcare Materials* (2021). (Cit. on p. 112).

- [Klos2012] C. Kloss et al. "Models, algorithms and validation for opensource DEM and CFD-DEM". *Progress in Computational Fluid Dynamics, An International Journal* 12.2/3 (2012). DOI: 10.1504/PCFD.2012.047457 (cit. on p. 27).
- [Klum2014] M. Klumpp et al. "Periodic open cellular structures with ideal cubic cell geometry: Effect of porosity and cell orientation on pressure drop behavior". *Chemical Engineering Journal* 242 (2014). DOI: 10.1016/j.cej.2013.12.060 (cit. on p. 41).
- [Krom2006] J. Kromkamp et al. "Effects of particle size segregation on cross-flow microfiltration performance: Control mechanism for concentration polarisation and particle fractionation". *Journal of Membrane Science* 268.2 (2006). DOI: 10.1016/j.memsci.2005.06.012 (cit. on p. 12).
- [Krüg2018] A. J. D. Krüger et al. "A catalyst-free, temperature controlled gelation system for in mold fabrication of microgels". *Chemical communications* 54.50 (2018). (Cit. on p. 79).
- [Krüg2019] A. J. D. Krüger et al. "Compartmentalized Jet Polymerization as a High-Resolution Process to Continuously Produce Anisometric Microgel Rods with Adjustable Size and Stiffness". *Advanced materials (Deerfield Beach, Fla.)* 31.49 (2019). DOI: 10.1002/adma.201903668 (cit. on p. 41).
- [Ksia2020] A. N. Ksiazkiewicz et al. "Closing the 1–5 μm size gap: Temperature-programmed, fed-batch synthesis of μm -sized microgels". *Chemical Engineering Journal* 379 (2020). DOI: 10.1016/j.cej.2019.122293 (cit. on p. 64).
- [Kuma2013] P. Kumar et al. "Perspective of membrane technology in dairy industry: a review". *Asian-Australasian journal of animal sciences* 26.9 (2013). DOI: 10.5713/ajas.2013.13082 (cit. on p. 3).
- [Lämm2018] M. Lämmermann et al. "Periodic open cellular structures (POCS) for intensification of multiphase reactors: Liquid holdup and two-phase pressure drop". *Chemical Engineering and Processing - Process Intensification* 126 (2018). DOI: 10.1016/j.cep.2018.02.027 (cit. on p. 41).

- [Lars1991] P. S. Larsen. "A stability model for the striping phenomenon in ultrafiltration". *Journal of Membrane Science* 57.1 (1991). (Cit. on pp. 66, 74, 79, 80).
- [Lee2016] J.-Y. Lee et al. "The potential to enhance membrane module design with 3D printing technology". *Journal of Membrane Science* 499 (2016). DOI: 10.1016/j.memsci.2015.11.008 (cit. on p. 15).
- [Leut2019] M. Leuthold, U. Grummert, and P. Schmidt. "Crossflow filtration unit for continuous diafiltration". *United States Patent* -.US 2019 / 0030486 A1 (2019). (Cit. on p. 86).
- [Léva2018] S. Lévy et al. "Frustrated packing in a granular system under geometrical confinement". *Soft matter* 14.3 (2018). DOI: 10.1039/c7sm01900a (cit. on p. 23).
- [Li2014] J. Li et al. "Similarity of wet granular packing to gels". *Nature communications* 5 (2014). DOI: 10.1038/ncomms6014 (cit. on p. 23).
- [Liét2011] J. J. Liétor-Santos, B. Sierra-Martin, and A. Fernández-Nieves. "Bulk and shear moduli of compressed microgel suspensions". *Physical Review E* 84.6 (2011). (Cit. on p. 36).
- [Life2021] Lifestraw. *LifeStraw Water Filters: Europe*. <https://eu.lifestraw.com/>. 2021 (cit. on p. 2).
- [Link2016] J. Linkhorst et al. "Microfluidic colloid filtration". *Scientific reports* 6 (2016). DOI: 10.1038/srep22376 (cit. on pp. 14, 24, 42, 65).
- [Link2019] J. Linkhorst et al. "Direct Observation of Deformation in Microgel Filtration". *Scientific reports* 9.1 (2019). DOI: 10.1038/s41598-019-55516-w (cit. on pp. 11, 15, 22–24, 42, 72, 112).
- [Loha2018] J. Lohaus, Y. M. Perez, and M. Wessling. "What are the microscopic events of colloidal membrane fouling?" *Journal of Membrane Science* 553 (2018). DOI: 10.1016/j.memsci.2018.02.023 (cit. on pp. 14, 24).
- [Loha2020] J. Lohaus et al. "What are the microscopic events during membrane backwashing?" *Journal of Membrane Science* 602 (2020). DOI: 10.1016/j.memsci.2020.117886 (cit. on pp. 14, 24, 65).
- [Löls2017] J. Lölsberg et al. "3D-printed electrodes with improved mass transport properties". *ChemElectroChem* 4.12 (2017). (Cit. on p. 16).

- [Löls2018] J. Lölsberg et al. "3D nanofabrication inside rapid prototyped microfluidic channels showcased by wet-spinning of single micrometre fibres". *Lab on a chip* 18.9 (2018). DOI: 10.1039/c7lc01366c (cit. on pp. 16, 25, 42).
- [Löls2019] J. Lölsberg et al. "Two-Photon Vertical-Flow Lithography for Microtube Synthesis". *Small (Weinheim an der Bergstrasse, Germany)* (2019). DOI: 10.1002/smll.201901356 (cit. on pp. 42, 43, 47).
- [Lore2016] S. Lorenzen et al. "Direct observation of fouling phenomena during cross-flow filtration: Influence of particle surface charge". *Journal of Membrane Science* 510 (2016). DOI: 10.1016/j.memsci.2016.01.046 (cit. on p. 64).
- [Lu2001a] W.-M. Lu et al. "Compression of deformable gel particles". *Powder Technology* 116.1 (2001). (Cit. on pp. 23, 36).
- [Lu2001b] W.-M. Lu et al. "Constant pressure filtration of monodispersed deformable particle slurry". *Separation Science and Technology* 36.11 (2001). DOI: 10.1081/SS-100106098 (cit. on p. 23).
- [Lüke2020] A. Lüken et al. "Unravelling colloid filter cake motions in membrane cleaning procedures". *Scientific Reports* 10.1 (2020). DOI: 10.1038/s41598-020-76970-x (cit. on pp. 24, 85, 101).
- [Lüke2021] A. Lüken et al. "Particle movements provoke avalanche-like compaction in soft colloid filter cakes". *Scientific reports* 11.1 (2021). DOI: 10.1038/s41598-021-92119-w (cit. on pp. 53, 55).
- [Mart2013] Martin Morrissey and Dennis Wong. "Disposable tangential flow filtration liner with sensor mount". *United States Patent* -.US 8.454,822 B2 (2013). (Cit. on p. 86).
- [Mart2018] M. C. Martí-Calatayud, S. Schneider, and M. Wessling. "On the rejection and reversibility of fouling in ultrafiltration as assessed by hydraulic impedance spectroscopy". *Journal of Membrane Science* 564 (2018). DOI: 10.1016/j.memsci.2018.07.021 (cit. on p. 65).
- [Meir2004] M. Meireles et al. "The origin of high hydraulic resistance for filter cakes of deformable particles: cell-bed deformation or surface-layer effect?" *Chemical engineering science* 59.24 (2004). (Cit. on p. 23).

- [Meng2007] Z. Meng et al. "Crystallization behavior of soft, attractive microgels". *The journal of physical chemistry. B* 111.25 (2007). DOI: 10.1021/jp073122n (cit. on p. 79).
- [Menu2012] P. Menut et al. "Does size matter? Elasticity of compressed suspensions of colloidal- and granular-scale microgels". *Soft matter* 8.1 (2012). DOI: 10.1039/C1SM06355C (cit. on p. 23).
- [Meuw2007] F. Meuwly et al. "Packed-bed bioreactors for mammalian cell culture: bioprocess and biomedical applications". *Biotechnology advances* 25.1 (2007). DOI: 10.1016/j.biotechadv.2006.08.004 (cit. on p. 40).
- [Moha2012] A. W. Mohammad et al. "Ultrafiltration in Food Processing Industry: Review on Application, Membrane Fouling, and Fouling Control". *Food and Bioprocess Technology* 5.4 (2012). DOI: 10.1007/s11947-012-0806-9 (cit. on p. 22).
- [Moha2014] P. S. Mohanty et al. "Effective interactions between soft-repulsive colloids: experiments, theory, and simulations". *The Journal of Chemical Physics* 140.9 (2014). DOI: 10.1063/1.4866644 (cit. on p. 22).
- [Moha2017] P. S. Mohanty et al. "Interpenetration of polymeric microgels at ultrahigh densities". *Scientific reports* 7.1 (2017). DOI: 10.1038/s41598-017-01471-3 (cit. on pp. 22, 65, 74, 79).
- [Mulu2011] M. Muluneh et al. "Direct visualization of pH-dependent evolution of structure and dynamics in microgel suspensions". *Journal of physics. Condensed matter : an Institute of Physics journal* 23.50 (2011). DOI: 10.1088/0953-8984/23/50/505101 (cit. on p. 74).
- [Musu2018] T. Musumeci et al. "Tangential Flow Filtration Technique: An Overview on Nanomedicine Applications". *Pharmaceutical nanotechnology* 6.1 (2018). DOI: 10.2174/2211738506666180306160921 (cit. on p. 84).
- [Nels2005] B. K. Nelson and D. M. Barbano. "A Microfiltration Process to Maximize Removal of Serum Proteins from Skim Milk Before Cheese Making". *Journal of dairy science* 88.5 (2005). (Cit. on p. 3).
- [Ngen2010a] I. S. Ngene et al. "A microfluidic membrane chip for in situ fouling characterization". *Journal of Membrane Science* 346.1 (2010). DOI: 10.1016/j.memsci.2009.09.035 (cit. on p. 65).

- [Ngen2010b] I. S. Ngene. *Real time visual characterization of membrane fouling and cleaning*. [S.l.: s.n.], 2010 (cit. on p. 8).
- [Nied2017] M. Niederberger. "Multiscale Nanoparticle Assembly: From Particulate Precise Manufacturing to Colloidal Processing". *Advanced Functional Materials* 27.47 (2017). DOI: 10.1002/adfm.201703647 (cit. on p. 110).
- [Nir2016] O. Nir et al. "Microfiltration of deformable microgels". *Soft matter* 12.31 (2016). DOI: 10.1039/c6sm01345g (cit. on pp. 65, 85).
- [Noro2016] H. R. Norouzi et al. *Coupled CFD-DEM modeling: formulation, implementation and application to multiphase flows*. John Wiley & Sons, 2016 (cit. on p. 27).
- [Oert2015] H. Oertel, M. Böhle, and T. Reviol. *Strömungsmechanik: Für Ingenieure und Naturwissenschaftler*. 7., überarb. Aufl. Wiesbaden: Springer Vieweg, 2015 (cit. on p. 11).
- [Oğuz2012] E. C. Oğuz et al. "Crystalline multilayers of charged colloids in soft confinement: experiment versus theory". *Journal of physics. Condensed matter : an Institute of Physics journal* 24.46 (2012). DOI: 10.1088/0953-8984/24/46/464123 (cit. on p. 23).
- [Palo2013] D. Paloli et al. "Fluid–solid transitions in soft-repulsive colloids". *Soft matter* 9.11 (2013). DOI: 10.1039/c2sm27654b (cit. on p. 72).
- [Park2020] G. W. Park and G. Nägele. "Modeling cross-flow ultrafiltration of permeable particle dispersions". *The Journal of Chemical Physics* 153.20 (2020). DOI: 10.1063/5.0020986 (cit. on p. 85).
- [Pete1993] Peter Henriksen and Ole Hassager. "Simulation of transport phenomena in ultrafiltration". *Chemical Engineering Science* 49.17 (1993). (Cit. on pp. 66, 79, 80).
- [Peto2010] A. R. Petosa et al. "Aggregation and deposition of engineered nanomaterials in aquatic environments: role of physicochemical interactions". *Environmental science & technology* 44.17 (2010). DOI: 10.1021/es100598h (cit. on p. 14).
- [Peyt2006] S. R. Peyton et al. "The use of poly(ethylene glycol) hydrogels to investigate the impact of ECM chemistry and mechanics on smooth muscle cells". *Biomaterials* 27.28 (2006). DOI: 10.1016/j.biomaterials.2006.05.012 (cit. on p. 33).

- [Pire1990] J. M. Piret and C. L. Cooney. "Immobilized mammalian cell cultivation in hollow fiber bioreactors". *Biotechnology advances* 8.4 (1990). (Cit. on p. 40).
- [Plam2017] F. A. Plamper and W. Richtering. "Functional Microgels and Microgel Systems". *Accounts of chemical research* 50.2 (2017). DOI: 10.1021/acs.accounts.6b00544 (cit. on pp. 64, 84, 85).
- [Plue1999] A. Pluen et al. "Diffusion of Macromolecules in Agarose Gels: Comparison of Linear and Globular Configurations". *Biophysical Journal* 77 (1999). (Cit. on p. 112).
- [Raut2004] R. Rautenbach and T. Melin. *Membranverfahren*. Berlin, Germany and Berlin, Germany: Springer, 2004 (cit. on pp. 22, 53, 64, 84).
- [Rich2002] J. F. Richardson et al. *Coulson and Richardson's chemical engineering: Particle technology and separation processes; Vol. 2*. 5th ed / J.F. Richardson and J.H. Harker with J.R. Backhurst. Oxford and Boston: Butterworth-Heinemann, 2002 (cit. on p. 10).
- [Rich2016] J. J. Richardson et al. "Innovation in Layer-by-Layer Assembly". *Chemical reviews* 116.23 (2016). DOI: 10.1021/acs.chemrev.6b00627 (cit. on p. 110).
- [Roa2015] R. Roa, E. K. Zholkovskiy, and G. Nägele. "Ultrafiltration modeling of non-ionic microgels". *Soft matter* 11.20 (2015). DOI: 10.1039/c5sm00678c (cit. on pp. 7, 85).
- [Roa2016] R. Roa et al. "Ultrafiltration of charge-stabilized dispersions at low salinity". *Soft matter* 12.20 (2016). DOI: 10.1039/c6sm00660d (cit. on p. 7).
- [Robe2001] Robert van Reis and Andrew Zydney. "Membrane separations in biotechnology". *Current opinion in biotechnology* 12.2 (2001). (Cit. on p. 2).
- [Roll2005] J. P. Rolland et al. "Direct Fabrication and Harvesting of Monodisperse, Shape-Specific Nanobiomaterials". *Journal of the American Chemical Society* 127.28 (2005). DOI: 10.1021/ja051977c (cit. on p. 41).

- [Ronc2003] C. Ronco et al. "Evolution of synthetic membranes for blood purification: the case of the Polyflux family". *Nephrology, dialysis, transplantation : official publication of the European Dialysis and Transplant Association - European Renal Association* 18 Suppl 7 (2003). DOI: 10.1093/ndt/gfg1073 (cit. on pp. 86, 87).
- [Rose2017] J. C. Rose et al. "Nerve Cells Decide to Orient inside an Injectable Hydrogel with Minimal Structural Guidance". *Nano Letters* 17.6 (2017). DOI: 10.1021/acs.nanolett.7b01123 (cit. on p. 41).
- [Rudo2019] G. Rudolph et al. "A review of in situ real-time monitoring techniques for membrane fouling in the biotechnology, biorefinery and food sectors". *Journal of Membrane Science* 588.2 (2019). DOI: 10.1016/j.memsci.2019.117221 (cit. on p. 12).
- [Saur2014] A. Sauret et al. "Clogging by sieving in microchannels: Application to the detection of contaminants in colloidal suspensions". *Applied Physics Letters* 105.7 (2014). DOI: 10.1063/1.4893459 (cit. on p. 14).
- [Saxe2009] A. Saxena et al. "Membrane-based techniques for the separation and purification of proteins: an overview". *Advances in colloid and interface science* 145.1-2 (2009). DOI: 10.1016/j.cis.2008.07.004 (cit. on p. 84).
- [Send2016] Z. B. Sendekie and P. Bacchin. "Colloidal Jamming Dynamics in Microchannel Bottlenecks". *Langmuir : the ACS journal of surfaces and colloids* 32.6 (2016). DOI: 10.1021/acs.langmuir.5b04218 (cit. on pp. 14, 24, 64).
- [Senf1999] H. Senff and W. Richtering. "Temperature sensitive microgel suspensions: Colloidal phase behavior and rheology of soft spheres". *The Journal of Chemical Physics* 111.4 (1999). DOI: 10.1063/1.479430 (cit. on pp. 65, 80, 103).
- [Shaw2018] L. A. Shaw et al. "Scanning two-photon continuous flow lithography for synthesis of high-resolution 3D microparticles". *Optics express* 26.10 (2018). DOI: 10.1364/OE.26.013543 (cit. on p. 42).
- [Shol2016] D. S. Sholl and R. P. Lively. "Seven chemical separations to change the world". *Nature News* 532.7600 (2016). (Cit. on p. 1).

- [Shri2008] A. Shrivastava, S. Kumar, and E. L. Cussler. "Predicting the effect of membrane spacers on mass transfer". *Journal of Membrane Science* 323.2 (2008). DOI: 10.1016/j.memsci.2008.05.060 (cit. on p. 16).
- [Sier2011] B. Sierra-Martin et al. "Determination of the bulk modulus of microgel particles". *Colloid and Polymer Science* 289.5-6 (2011). DOI: 10.1007/s00396-010-2346-z (cit. on p. 36).
- [Tadr2011] T. F. Tadros. *Microgel Suspensions: Fundamentals and Applications*. Weinheim: Wiley-VCH, 2011 (cit. on p. 84).
- [Tana1982] Y. Tanaka, K. Ogawa, and M. Hioka. "Plate type fluid treatment apparatus." *United States Patent* -.4,310,416 (1982). (Cit. on p. 86).
- [Tanu2017] H. J. Tanudjaja et al. "Effect of cross-flow velocity, oil concentration and salinity on the critical flux of an oil-in-water emulsion in microfiltration". *Journal of Membrane Science* 530 (2017). DOI: 10.1016/j.memsci.2017.02.011 (cit. on pp. 66, 74, 79).
- [Tanu2018] H. J. Tanudjaja et al. "Striping phenomenon during cross-flow microfiltration of oil-in-water emulsions". *Separation and Purification Technology* 207 (2018). DOI: 10.1016/j.seppur.2018.07.007 (cit. on pp. 66, 79).
- [Teme2002] J. S. Temenoff et al. "Effect of poly (ethylene glycol) molecular weight on tensile and swelling properties of oligo (poly (ethylene glycol) fumarate) hydrogels for cartilage tissue engineering". *Journal of Biomedical Materials Research: An Official Journal of The Society for Biomaterials, The Japanese Society for Biomaterials, and The Australian Society for Biomaterials and the Korean Society for Biomaterials* 59.3 (2002). (Cit. on p. 33).
- [Tepp2022] M. Tepper et al. "Rotating microstructured spinnerets produce helical ridge membranes to overcome mass transfer limitations". *Journal of Membrane Science* 643.1–2 (2022). DOI: 10.1016/j.memsci.2021.119988 (cit. on p. 16).
- [Thor2011] J. B. Thorne, G. J. Vine, and M. J. Snowden. "Microgel applications and commercial considerations". *Colloid and Polymer Science* 289.5-6 (2011). DOI: 10.1007/s00396-010-2369-5 (cit. on p. 85).

- [van 2016] T. de van Laar et al. "Transition-state theory predicts clogging at the microscale". *Scientific reports* 6 (2016). DOI: 10.1038/srep28450 (cit. on p. 24).
- [van 2018] R. van Zwieten et al. "From cooperative to uncorrelated clogging in cross-flow microfluidic membranes". *Scientific reports* 8.1 (2018). DOI: 10.1038/s41598-018-24088-6 (cit. on pp. 64, 65).
- [Wang2018] D. Wang et al. "Interplay between spherical confinement and particle shape on the self-assembly of rounded cubes". *Nature communications* 9.1 (2018). DOI: 10.1038/s41467-018-04644-4 (cit. on p. 110).
- [Wei2011] H. Wei et al. "Particle sorting using a porous membrane in a microfluidic device". *Lab on a chip* 11.2 (2011). DOI: 10.1039/c0lc00121j (cit. on p. 64).
- [Well2015] S. Wellert et al. "Responsive Microgels at Surfaces and Interfaces". *Zeitschrift für Physikalische Chemie* 229.7-8 (2015). DOI: 10.1515/zpch-2014-0568 (cit. on p. 73).
- [Wies2018] M. Wiese et al. "Fouling minimization at membranes having a 3D surface topology with microgels as soft model colloids". *Journal of Membrane Science* (2018). (Cit. on pp. 2, 72, 85).
- [Wies2019] M. Wiese et al. "Charged microgels adsorbed on porous membranes - A study of their mobility and molecular retention". *Journal of Membrane Science* 588 (2019). DOI: 10.1016/j.memsci.2019.117190 (cit. on pp. 65, 67, 74).
- [Wint2005] T. Wintgens et al. "The role of membrane processes in municipal wastewater reclamation and reuse". *Desalination* 178.1-3 (2005). DOI: 10.1016/j.desal.2004.12.014 (cit. on p. 84).
- [Wolf2018] H. J. M. Wolff et al. "From Batch to Continuous Precipitation Polymerization of Thermoresponsive Microgels". *ACS applied materials & interfaces* 10.29 (2018). DOI: 10.1021/acsami.8b06920 (cit. on pp. 84, 102).
- [Wolf2020] H. J. M. Wolff et al. "Soft temperature-responsive microgels of complex shape in stop-flow lithography". *Lab on a chip* 20.2 (2020). DOI: 10.1039/c9lc00749k (cit. on p. 41).

- [Wyss2010] H. M. Wyss et al. "Capillary micromechanics: Measuring the elasticity of microscopic soft objects". *Soft matter* 6.18 (2010). DOI: 10.1039/c003344h (cit. on p. 36).
- [Xia2013] L.-W. Xia et al. "Nano-structured smart hydrogels with rapid response and high elasticity". *Nature communications* 4 (2013). DOI: 10.1038/ncomms3226 (cit. on p. 64).
- [Yehl2020] C. J. Yehl and A. L. Zydney. "Single-use, single-pass tangential flow filtration using low-cost hollow fiber modules". *Journal of Membrane Science* 595.3 (2020). DOI: 10.1016/j.memsci.2019.117517 (cit. on p. 86).
- [Zahe2019] M. R. Zaheer, A. Gupta, et al. "Current development and future perspectives of microbial enzymes in the dairy industry". In *Enzymes in food biotechnology*. Elsevier, 2019. Pp. 287–302. (Cit. on p. 3).
- [Zama2009] A. Zamani and B. Maini. "Flow of dispersed particles through porous media — Deep bed filtration". *Journal of Petroleum Science and Engineering* 69.1-2 (2009). DOI: 10.1016/j.petrol.2009.06.016 (cit. on p. 65).
- [Zama2016] F. Zamani et al. "Impact of the surface energy of particulate foulants on membrane fouling". *Journal of Membrane Science* 510 (2016). DOI: 10.1016/j.memsci.2016.02.064 (cit. on p. 58).
- [Zato2009] M. Zator et al. "Microfiltration of protein/dextran/polyphenol solutions: Characterization of fouling and chemical cleaning efficiency using confocal microscopy". *Journal of Membrane Science* 344.1-2 (2009). DOI: 10.1016/j.memsci.2009.07.038 (cit. on p. 65).
- [Zhan2012] K. Zhang, M. Jiang, and D. Chen. "Self-assembly of particles—The regulatory role of particle flexibility". *Progress in Polymer Science* 37.3 (2012). DOI: 10.1016/j.progpolymsci.2011.09.003 (cit. on p. 110).
- [Zhu2007] H. P. Zhu et al. "Discrete particle simulation of particulate systems: Theoretical developments". *Chemical Engineering Science* 62.13 (2007). DOI: 10.1016/j.ces.2006.12.089 (cit. on p. 27).

